Millimeter Wave Outdoor Cellular Networks: Stochastic Geometry Channel Modeling and Performance Analysis

NOR AISHAH MUHAMMAD

A thesis submitted in fulfillment
of requirements for the degree of
Doctor of Philosophy

School of Electrical & Information Engineering
The University of Sydney

January 2019

Abstract

The tremendous growth of wireless services on hand-held devices has led to an explosive demand for high data rate transmissions. Future cellular networks will make use of higher frequency bands, i.e., millimeter wave (MMW), for enabling extremely high data rates to support content-rich applications. Although the MMW bands potentially offer numerous significant performance improvements in wireless networks, they still face many technical challenges related to the unique propagation characteristics and hardware constraints.

MMW communications exhibit severe path loss, vulnerability to blockages, and sparse multipath environments. Furthermore, the small wavelengths at MMW frequencies allow the incorporation of massive number of antennas into the MMW transceivers. These antennas can provide narrow beams with high gains to compensate the severe path loss and boost the received signal power. The fundamental differences between MMW and conventional microwave frequencies require revisiting the prior channel modeling to properly assess the networks performance. For that, in this thesis, we focus on the channel modeling, system design, and performance evaluation by incorporating the distinguishing features of MMW communication in the analysis.

In the first contribution, we develop a geometry-based stochastic channel model to characterize the effect of multipath propagation, i.e., the first-order reflection path between the transmitter and receiver. By considering random locations, sizes and orientations of buildings, we derive a closed-form analytical

expression for the power delay profile (PDP) contributed by all the first-order reflection paths. We show that wireless networks can benefit from buildings in the surrounding area of MMW communications, as the external surfaces of buildings render reflection paths whose signal powers are comparable to that of the line-of-sight (LoS) path.

Two critical features of the MMW cellular networks will be dense base stations (BSs) deployment and highly directional transmissions at both BS and mobile. The dense deployment of the MMW BSs leads to a higher user data rate, but it also introduces more interference to the receiver. In the second contribution, we propose a BS coordination scheme via disjoint clustering to provide satisfactory user performance in the dense MMW cellular networks. Leveraging concepts from stochastic geometry, we derive expressions for the signal-to-interference and noise ratio (SINR) coverage probability and area spectral efficiency (ASE) in the downlink MMW cellular networks by incorporating the peculiarity characteristics of MMW communications. Our results show a significant improvement in performance in terms of SINR coverage probability and ASE. The results also demonstrate the performance superiority of BS coordination via disjoint clustering over the non-coordinated case.

As the third contribution, we investigate the uplink performance of the MMW cellular networks with clustered users. By modeling the locations of users as of a Poisson cluster process (PCP), we derive tractable expressions to evaluate the SINR coverage probability in the uplink MMW cellular networks. We study the performances of a reference BS for two association strategies. First, the closest-selection (CS), where the nearest LoS BS serves the user. Second, the strongest-selection (SS), where the user communicates with the BS that provides the most significant received signal among all BSs. We investigate the impact of system parameters, such as blockage, the density of BSs, cluster radius and fractional power control (FPC) factor on the SINR coverage. Our results show

that regarding SINR coverage probability, the SS strategy outperforms the CS strategy in the environment with dense blockages.

Dedicated to my beloved husband,

parents and family.

Acknowledgement

First and foremost, I thank God Almighty for His blessings and for giving me the strength and wisdom to achieve my dreams.

I would like to express my utmost gratitude to my supervisor, Prof. Yonghui Li for being a dedicated mentor in guiding and helping me towards the completion of the thesis. Special thanks to Dr. Peng Wang and Dr. He Chen for their helpful guidance, valuable suggestions and encouragement in improving the quality of my papers. I would also like to give my most sincere thanks to Prof. Branka and Dr. Wei Bao for their insightful comments on my research work.

I would like to thank my various sources of financial support. Firstly, I would like to acknowledge the postgraduate scholarships (SLAI) from the Malaysian Ministry of Education (KPM), Universiti Teknologi Malaysia (UTM), and the School of Electrical and Information Engineering. I am grateful to The University of Sydney for the Norman I Prize Supplementary Scholarship and the University of Sydney's PRSS scheme, which allowed me to attend various local and international conferences.

Many thanks to current and past members of the Telecommunication Lab at The University of Sydney for creating a friendly and pleasant working environment. Thanks to all my colleagues who offered helpful discussions: Kolyan, Rana, Yuehua, Loris, Matthew, David, Wenlong, and others. My warmest thanks are also extended to all my wonderful friends for making my life in Sydney the most memorable and enjoyable journey. To Ilyana, Aziah, Fatin, Safura, Shima,

Mashani, Ain, Maria, Rosheila, and not to forget the 'Power Puff Moms' group, thank you very much for giving me such a beautiful memory. Also, many thanks to all Zara's babysitters for helping me during my studies.

I must acknowledge with tremendous thanks to my beloved husband, Azmel Othman, my children Aleesya Zara and Aydeen Ziad. Through your unconditional love, patience, support, and believe in me, I have been able to complete my PhD journey. Thank you with all my heart and soul.

Finally, I take this opportunity to express my profound gratitude to my loving parents and family for understanding, support, and endless love during my study in Australia. I would like to devote all my research achievements to them.

Nor Aishah Muhammad

Sydney, NSW, Australia

Jan 2019

Declaration

I hereby declare that this submission is my own work and that, to the best of my knowledge and belief, it contains no material previously published or written by another person nor material which to a substantial extent has been accepted for the award of any other degree or diploma of the University or other institute of higher learning, except where due acknowledgment has been made in the text.

Nor Aishah Muhammad

School of Electrical and Information Engineering

The University of Sydney

January 2019

Related Publications

The following is a list of publications in refereed journals and conference proceedings produced during my Ph.D. candidature.

Journal Papers

[$\mathbf{J}_1$] N. A. Muhammad, N. I. A. Apandi, H. Chen, Y. Li, and B. Vucetic, "Uplink Performance Analysis for Millimeter Wave Cellular Networks with Clustered Users," submitted to *IEEE Transactions on Communications*, 2018.

[$\mathbf{J}_2$] N. A. Muhammad, P. Wang, Y. Li, and B. Vucetic, "Analytical model for outdoor millimeter wave channels using geometry-based stochastic approach," *IEEE Transactions on Vehicular Technology*, vol. 66, no. 2, pp. 912-926, Feb 2017.

Conference Papers

[$\mathbf{C}_1$] N. A. Muhammad, H. Chen, W. Bao, Y. Li, and B. Vucetic, "Multi-cell Coordination via Disjoint Clustering in Dense Millimeter Wave Cellular Networks," in Proc. of IEEE International Conference on Communications (ICC), May. 2017.

Table of Contents

List of Figures

List of Tables

List of Acronyms

ADC Analog-to-Digital converter

ASE Area Spectral Efficiency

BS Base Station

CS Closest-selection

FPC Fractional power control

LoS Line-of-sight

MCP Matern cluster process

MMW Millimeter Wave

PCP Poisson Cluster Process

PDF Probability Density Function

PDP Power Delay Profile

PPP Poisson Point Process

RF Radio frequency

SINR Signal-to-Interference and Noise Ratio

SS Strongest-selection

UE User Equipment

Chapter 1

Introduction

This chapter presents an introduction to the thesis. It provides an overview of the research background and motivation, before summarizing the principle research problems and the main contributions of this thesis.

1.1 Background and Motivation

1.1.1 The Scarcity of Wireless Bandwidth

Wireless services become increasingly important not only for communications, but also for education, entertainment, location tracking, and healthcare. Therefore, demands for reliable transmission with high data rates and low latency connections have escalated worldwide. The remarkable evolution of smart-phones along with new wireless applications such as uncompressed high definition video streaming, online gaming and cloud computing, has coincided with the explosive growth of mobile data traffic. Recently, Cisco reported that the global mobile data traffic grew approximately 60 percent in 2016 and will continue to increase at a compounded annual growth rate (CAGR) of 47 percent from 2016 to 2021, where 78 percent of the contents will be video by 2021 [5]. In addition to the exponential increase in the data traffic volume, the explosion of wireless devices

is expected, chiefly smart-phones that will increase to 43 percent by 2021 [5]. These significant demands have driven both industry and academia to develop the next generation wireless cellular networks, referred to as the fifth-generation (5G) networks, to increase the data rate drastically.

How to cope with the substantial mobile traffic volume and data rate demands while offering an excellent quality of experience to users, is a challenging question for the network operators. Theoretically, the Shannon formula represents the channel capacity as [6]

$$C = BW \log_2 \left(1 + \frac{S}{N}\right), \tag{1.1}$$

where C is the maximum channel capacity in bits/second, BW is the channel bandwidth, S is the received signal power, and N is the noise power. From (1.1), it demonstrates one possible way to increase the channel capacity is by enlarging the bandwidth of the channel, increasing the received signal or decreasing the noise power at the receiver.

The current fourth generation (4G) systems have already implemented advanced technologies such as orthogonal frequency division multiplexing (OFDM), channel coding, multiple inputs multiple outputs (MIMO), cell splitting and heterogeneous networks, to achieve link capacity close to the theoretical limit. However, with only incremental improvements to the cellular systems, expect them to be inadequate to fulfill the projected capacity required in the upcoming 5G networks. Thus, it is evident that the potential solution to improve the system capacity is by increasing the channel bandwidth. The existing microwave spectrum, however, has been fully utilized and becoming increasingly congested. For this reason, the millimeter wave (MMW) band has received significant attention in the past few years as a promising and attractive option for supporting extremely high data rate wireless communication [1, 3, 7, 8].

1.1.2 The Use of Millimeter Wave Bandwidth

MMW generally refers to the electromagnetic spectrum in the range from 30 GHz to 300 GHz, where the wavelengths are from 1 mm to 10 mm. Following the existing spectrum allocation in Fig. 1.1, the current microwave cellular networks had only utilized a tiny portion of the full electromagnetic spectrum and thus there are massively unused spectrum blocks, especially at MMW bands. A fraction of the MMW spectrum has been used for several services such as military applications, satellite communications [9] and local multipoint distribution services (LMDS) [10], leaving more available. More recently, many countries including the USA, Europe, Australia, Japan and Korea have designated frequencies from 57 GHz to 66 GHz for unlicensed wireless applications such as wireless personal area networks (WPAN) and wireless local area networks (WLAN). As a result from these applications, several industrial standards have been developed, such as IEEE 802.15c, which is a standard for wireless personal area networks (WPAN) [11], IEEE 802.11ad (WiGig) at 60 GHz for short range applications [12], WirelessHD consortium [13], and IEEE 802.11ay [14].

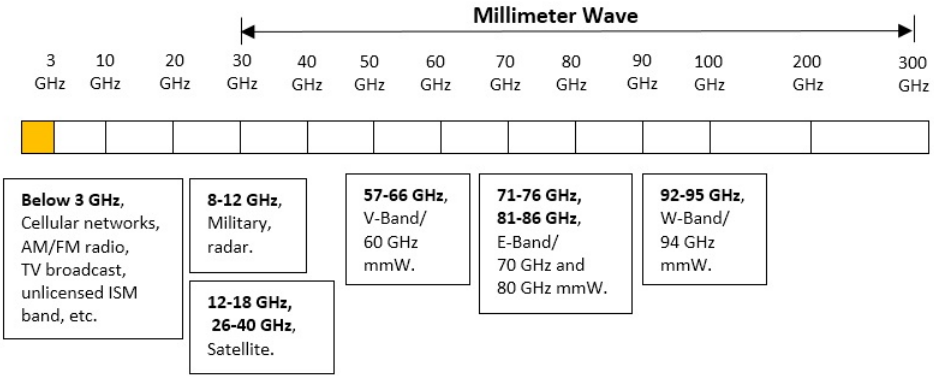

Figure 1.1. Operating range of existing wireless applications [1, 2].

Later the use of slightly higher frequencies in MMW spectrum has attracted growing attention among researchers as announced by the Federal Communications Commission (FCC) [15] and the European Conference of Postal and

Telecommunications Administrations (CEPT) [16] that 71-76 GHz, 81-86 GHz, and 92-95 GHz frequency bands had become available for point-to-point WLAN and cellular backhaul. Unlike 60 GHz frequency spectrum, these bands are on a lightly-licensed basis that will be used for cellular networks as the licensed spectrum better guarantees the quality of service. In particular, the higher frequencies in MMW spectrum became a critical topic of discussion concerning spectrum for 5G wireless cellular networks. Despite the potential capability to deliver extremely high data rates, wireless systems operating at MMW frequencies have several unique characteristics compared to their microwave counterparts, which introduce new challenges in the system design, modeling and analysis.

1.1.3 The Challenges in Millimeter Wave Cellular System Design

In this section, we describe several key disruptions in the MMW cellular system design related to unique propagation characteristics and hardware constraints.

Environmental factors such as oxygen molecules, water vapor, and rain effect MMW signals. Specifically, atmospheric absorption occurs when the electromagnetic waves are traveling through the atmosphere absorbed by oxygen, water vapor, and other gasses. Atmospheric absorption of electromagnetic waves varies significantly with frequency, as illustrated in Fig. 1.2. The severe atmospheric absorption at certain frequencies, e.g., 60 GHz and 180 GHz, which contribute about 17 dB/km and 7 dB/km, respectively, makes these particular frequencies mainly suitable for short-range application with a distance of a few meters. On top of the atmospheric absorption, raindrops render a further loss on the MMW signals where for the high intensity of rain, e.g., 100 mm/hr, the attenuation can contribute up to 30 dB/km, as depicted in Fig. 1.3, which may require a backup connection for countering the link failures in the heavy rain season.

Penetration losses due to blockages, e.g., building and tree, are much more

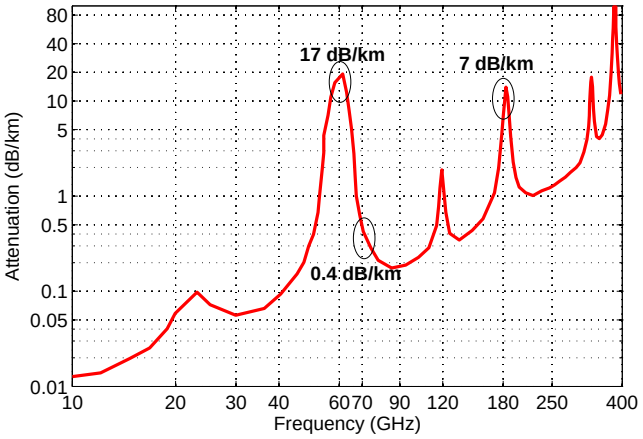

Figure 1.2. Atmospheric absorption of electromagnetic waves [3].

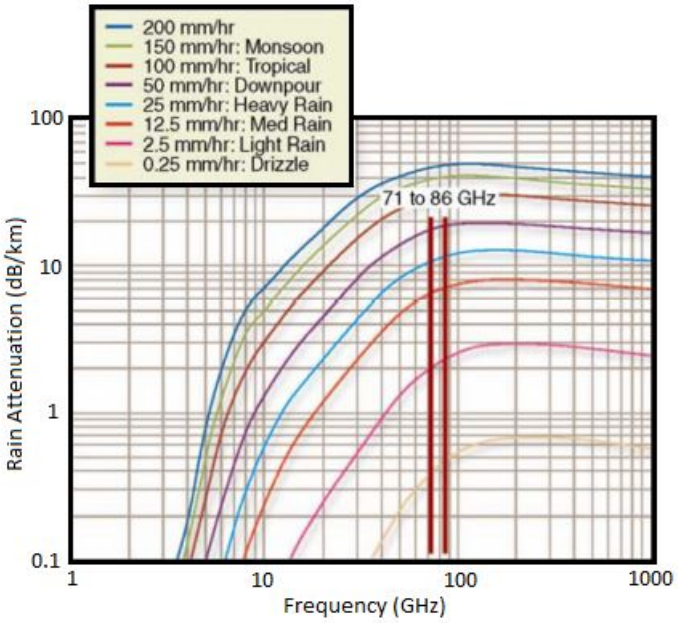

Figure 1.3. Rain attenuation across frequency at various rainfall intensities [3].

severe at MMW frequencies than lower frequency signals. These blockages result in entirely different path loss characteristics between line-of-sight (LoS) and non-LoS propagation [3, 17, 18]. Furthermore, sharp shadow zones occur due to the significantly larger sizes of blockages relative to the signal wavelength at MMW frequencies, which lead to insignificant diffraction mechanism [19]. Thus, MMW channels are expected to exhibit a sparse multipath nature, instead of the rich-scattering one demonstrated in conventional microwave channels. As a result,

it is not possible to directly use microwave propagation models for MMW systems. There are several works on the MMW channel model [20, 21, 22, 23], which have been mainly focusing on the shadowing effects due to blockages. However, as verified by the channel measurements in [19, 24], the reflection paths generated by buildings can also provide a non-negligible multipath propagation, which highlights the importance of considering the reflection paths in MMW channel modeling. So far, there has been only a few discussions regarding the multipath propagation in the MMW bands, including [25, 26, 27, 28]. The common limitation of these works is that the channel statistics are based on empirical or site-specific approaches, making these models not applicable to general environments. Therefore, an in-depth characterization of MMW channels with more general settings is of both theoretical and practical interest and still presents challenging open problems.

Another key feature of the MMW system is that the MMW signals encounter high near-field path loss as this loss increases with the carrier frequency. Large-scale antenna arrays that provide highly directional beamforms are envisioned to be one of the critical enablers for cellular communication at MMW bands in order to compensate the increased near-field path loss [29]. However, the use of a highly directional antenna poses challenges in the initial cell search where both base stations and mobiles may need to scan different angles to find the suitable propagation path, which could incur a significant delay in initial access and handovers [30, 31]. Furthermore, for a substantial number of antenna, equipping a single radio frequency (RF) chain per antenna may significantly increase cost, complexity and power consumption [32]. The MMW cellular system can employ analog or hybrid beamforming, which potentially reduces the number of RF chains [33]. MMW cellular networks may also apply low resolution analog-to-digital converters (ADCs) at receivers to reduce the power consumption [34, 35].

It is clear from the discussions mentioned above that designing cellular net-

works at higher frequency is not a direct extension from the prior system architectures for the conventional cellular system. Many technical challenges in the system design need to be addressed and resolved before the full deployment of MMW networks. For that, in this thesis, we focus on the channel modeling, system design, and performance evaluation by incorporating the distinguishing features of MMW communication in the analysis.

1.2 Research Problems and Contributions

In this thesis, the challenges in MMW system design are considered by analytically study important system design issues to enable the use of higher frequency bands for cellular networks. The focus of this thesis is on the channel modeling, system design and performance analysis of MMW cellular networks. The outcomes of this thesis will provide fundamental and important insights into the design and analysis of future MMW cellular networks. In the sequel of this section, we elaborate the thesis research problems and the corresponding contributions.

The *first* research problem we tackle in this thesis (Chapter 3) is to develop the MMW propagation channel model by considering the reflection components of the MMW signals in an urban area. Motivated by the discussed shortcomings in the MMW channel modeling, we consider the first-order reflection path in the analysis. In the MMW bands, the higher-order reflections suffer from more severe path losses and attenuation. Therefore, we ignore the expected power contributed by these reflections as they are insignificant. Hence it is reasonable to only consider the first-order reflection paths in the analysis as these paths provide the strongest received power among all the reflection components [36].

The main contributions regarding this research problem are summarized as follows:

- Leveraging concepts of random shape theory [37], we first model buildings

in an urban area by incorporating the randomness of locations, sizes, and orientations. By the proposed propagation environment model, we derive a closed-form expression for the power delay profile (PDP) contributed by all the first-order reflection paths, which gives the intensity of the energy at the receiver relative to the propagation delay.

- Based on the PDP, we analyze the average path loss and the number of first-order reflection paths under various channel parameter settings.

- Finally, we compare the average path loss of the first-order reflection to that of the LoS path in [20]. Numerical results are provided to validate the accuracy of the proposed model under various channel parameter settings. Our analytical results show that the richness of the first-order reflection paths relies on the propagation environments such as the sizes and density of buildings. The contribution of the first-order reflection paths is comparable to the LoS path, especially in dense building areas.

A straightforward solution to overcome heavy penetration losses due to the blockages is to deploy dense MMW base stations (BSs). As highlighted in [4, 20, 38, 39], the dense deployment of the MMW cellular networks is required to improve the coverage and rate experienced by a user. However, the dense cellular networks will certainly cause high interference and affect the system performance. As is evident in [20, 22] that the MMW networks may change from noise-limited to interference-limited regime depending on several system parameters such as the density of transmitters and blockages, operating beamwidth and transmission power. Extensive research work on interference mitigation techniques have been explored in the past, e.g., BS cooperation [40, 41], coordinated scheduling/beamforming [42, 43, 44] and interference cancellation [45, 46]. However, these works focus primarily on microwave cellular systems where the analysis does not incorporate the unique channel characteristics and antenna features for

the MMW networks. Hence, the *second* research problem we tackle in this thesis (Chapter 4) is to propose and evaluate an interference mitigation scheme for improving the coverage and rate experienced by a user in the dense MMW cellular networks.

The main contributions regarding this research problem are summarized as follows:

- We develop a new mathematical framework to quantify the performance of BS coordination via disjoint clustering in dense MMW cellular networks. We derive the coverage probability and area spectral efficiency (ASE) using tools from stochastic geometry and by incorporating the key features of the MMW systems, i.e., blockage and directional antennas.

- We propose cluster-based intercell scheduling to coordinate the inference within a cluster and evaluate the performance of such a BS coordination under various system parameter settings.

- Numerical results show that the proposed BS coordination scheme offers a linear signal-to-interference and noise ratio (SINR) coverage gain and there is an optimum cluster size to achieve the maximum ASE. This optimal value increases as the blockage factor, which is determined by the density and the average size of the buildings, decreases.

In the context of system-level performance analysis, the point process is employed to capture topological randomness in the network geometry. It is common practice to use the uniform Poisson point process (PPP) if the distance between the transmitter and receiver is invariant to geographic location. However, non-uniformly distributed user may exist in highly populated or hotspot regions. Considering an urban outdoor area, the cluster of users may appear at the outside subway stations, on the bench of cafe terrace or traveling along the sidewalks during peak hours. Therefore, modeling user locations by uniform PPP

is not entirely accurate in these conditions. Thus, in the following chapter of this thesis (Chapter 5), we turn our attention to the different spatial distribution of transmitters, namely Poisson cluster process (PCP) to model the locations of clustered users. The *third* research problem is to develop an analytical framework for characterizing the performance of uplink MMW cellular networks in the clustered user scenario.

The main contributions regarding this research problem are summarized as follows:

- We present a mathematical framework for evaluating the performance of the uplink MMW cellular networks. Unlike typical stochastic frameworks where the locations of users follow the uniform PPP, we leverage PCP to model the locations of clustered users. Derivation of the Laplace transform of interference in the clustered users scenario leads to a new and more involved analysis compared to uniform PPP based assumption.

- We consider two types of association strategies, i.e., the closest-selection (CS) and the strongest-selection (SS). For each association strategy, we characterize the Laplace transform of the interferences and the SINR coverage probability of a reference BS. The key steps for the analysis are the derivation of distance distribution from the receiver to its serving BS and the distance distribution from the receiver to intra-cluster and inter-cluster interfering nodes.

- Numerical results show the accuracy of the analytical model under a wide range of SINR thresholds and user intensities. We investigate the impact of system parameters, such as blockage, the density of BSs, cluster radius and fractional power control (FPC) factor on the coverage probability. Our results show that regarding the SINR coverage probability, the SS strategy outperforms the CS strategy in the environment with dense blockages.

The results also demonstrate that moderate FPC factor should be used at the low SINR thresholds, while full FPC is optimal for the high SINR thresholds.

1.3 Thesis Outline

The remainder of the thesis is organized as follows.

Chapter 2 starts with the theoretical background related to the MMW cellular systems and point processes for stochastic geometry analysis. Then, chapters 3-5 present the main contributions of this thesis. Each chapter provides notations at the beginning for the reader's convenience. Chapter 3 formulates the channel model for MMW propagation by incorporating the non-line of sight component, i.e., the first-order reflection. In Chapter 4, we develop an analytical model to quantify the performance of BS coordination via disjoint clustering in the dense MMW cellular networks. Chapter 5 presents the analytical model for evaluating the uplink performance of clustered users. Finally, Chapter 6 concludes the thesis by summarizing the main results and discussing potential future research directions.

Chapter 2

Theoretical Background

This chapter provides the necessary theoretical background for our research work. First, we present a general system model and overview the essential properties of MMW communications that are important for developing analytical models to predict the performance of MMW cellular systems. Then, we briefly review some preliminaries for stochastic geometry, which are employed in the analysis in Chapters 3-5.

2.1 Fundamentals of MMW cellular systems

In this section, we present a general system model that considers a downlink transmission for a MMW cellular network operating at frequency f_c and bandwidth BW. Due to the sparsity of MMW channel, clustered channel model with a limited number of propagation paths has been used to model the MMW channel between BS and user [47, 48, 49]. In this thesis, we consider a single path channel model [21, 50], where the channel matrix between BS at $\mathbf{x}$ and user at $\mathbf{y}$ is expressed as

$$\mathbf{H}_{\mathbf{x},\mathbf{y}} = \sqrt{\frac{N_{BS}N_{UE}}{L(\mathbf{x},\mathbf{y})}} h_{\mathbf{x},\mathbf{y}} \mathbf{a}_{UE}(\phi_{x,y}) \mathbf{a}^*_{BS}(\theta_{x,y}), \tag{2.1}$$

where N_{BS} and N_{UE} are the number of antennas for the BS and user. $L(\cdot)$ is the path loss, $h_{(\cdot)}$ is the small scale fading. The angle $\phi_{(\cdot)}$ and $\theta_{(\cdot)}$ denote the angles of arrival (AoA) and departure (AoD) at the user and BS, respectively. $(\cdot)^*$ denotes the conjugate transpose. Finally, $\mathbf{a}_{UE}(\phi_{(\cdot)})$ and $\mathbf{a}_{BS}(\theta_{(\cdot)})$ are the spatial array responses for the user and BS, respectively.

2.1.1 Large-Scale Path Loss

The path loss $L(\mathbf{x}, \mathbf{y})$ in (2.1) can be modeled as

$$L(d) = \delta(d_0) + 10\alpha \log_{10}\left(\frac{d}{d_0}\right) + S, \tag{2.2}$$

where $d = |\mathbf{x} - \mathbf{y}|$ is the distance from BS at $\mathbf{x}$ and user at $\mathbf{y}$, $\delta(d_0)$ is the close-in path loss model, α is the path loss exponent and S is a random variable that represents a log-normal shadowing coefficient. The close-in path loss model can be given by the Friis's equation as [51]

$$\delta(d_0) = 20 \log_{10}\left(\frac{2\pi d f_c}{c}\right), \tag{2.3}$$

where f_c represents the carrier frequency, c is the speed of light and d_0 is the close-in distance of 1 meter.

Following the measurements in [3, 17, 18, 24], the presence of blockage in the direct path results in very different path loss laws for the LoS and non-LoS links. Extensive measurements of MMW channel by using directional antennas in [3] found that the path loss of a LoS link is $\alpha_L = 2$. In the non-LoS transmission, the path loss exponent is larger than that in LoS and varies depending on the surrounding environments. From the measurements in the New York and Austin city [18], the non-LoS path loss exponent was found to be $\alpha_N = 4.5$, $\alpha_N = 3.3$ and $\alpha_N = 4.7$ at operating frequency 28 GHz, 38 GHz and 73 GHz, respectively.

Table 2.1. Penetration losses for different materials and frequencies [4].

Material	Thickness(cm)	Attenuation		
		< 3 GHz [52], [54]	40 GHz [51]	60 GHz [52]
Drywall	2.5	5.4	-	6.0
Office whiteboard	1.9	0.5	-	9.6
Clear glass	0.3/0.4	6.4	2.5	3.6
Mesh glass	0.3	7.7	-	10.2
Chipwood	1.6	-	.6	-
Wood	0.7	5.4	3.5	-
Plasterboard	1.5	-	2.9	-
Mortar	10	-	160	-
Brick wall	10	-	178	-
Concrete	10	17.7	175	-

2.1.2 Effects of blockage

Vulnerability of MMW signals towards blockage results in two consequences: penetration loss and multi-path. The penetration losses due to building materials were measured at 28 GHz [24], 40 GHz [24, 52] and 60 GHz [53, 54]. According to these measurements, the penetration loss depends on the materials of the building wall. Table. 2.1 illustrates the penetration losses for different materials [4, 55]. For example, the 10 cm-thick brick and concrete exhibit losses of 178 dB and 175 dB, respectively, which result in the isolation of MMW outdoor BSs from indoor users. For inner building materials, the penetration loss through a 2.5 cm dry wall at 2.5 GHz is similar to that at 60 GHz [53], which motivates the deployment of indoor MMW femtocells or Wi-Fi systems.

Besides buildings, MMW signals also cannot penetrate through trees and the human body. At MMW frequencies, the presence of trees between transmitter and receiver can result in an additional loss of about 20 dB [56, 57], which can be an important issue in the link budget. Penetration loss due to the human body is as much as 20-35 dB [58], which significantly decreases the coverage probability of the MMW networks. Because of the sensitivity of the MMW signals to blockage, proper positioning of the BS is much needed to avoid large-scale blocking by

obstacles.

Measurements performed in frequency bands centered at 28 GHz, 38 GHz, 60 GHz, and 73 GHz [18, 38] show that an MMW channel has fewer multi-path component than a microwave channel. For instance, the average number of multi-path components was found to be approximately five at 28 GHz and three at 73 GHz in the Manhattan area [18]. Note that the multi-path component depends on the scattering environment. Also, the results in [38] indicate that the signal energy arrives in the form of clusters, mainly generated by reflections from the building walls. We found similar evidence in the ray tracing simulations conducted for the 28 GHz [59] and 73 GHz [60] bands, which supports the theory that the signal propagation mechanism in outdoor MMW channels can be accurately modeled based on reflection paths.

2.1.3 Beamforming

From (2.3), it documents the close in path loss increases with the carrier frequency. With the small wavelengths inherent in the MMW frequency range, massive arrays of steerable antenna that provide narrow beams with high gains can be deployed to compensate the severe path losses at MMW bands.

In the single path beamforming, the BS and user use the antenna arrays to transmit and receive via one data stream. When the LoS path dominates the communication channel or when there is a sufficiently small number of scatterers, it is possible to direct the beamforming vector to a specific desired direction in order to maximize the beamforming gain. Consequently, we have a beam with its main lobe pointing to the desired direction. For analytical tractability, in this thesis, we consider a sectored antenna model as initially proposed in [61] to approximate the actual array beam patterns. A sectored antenna model as shown in Fig. 2.1 is characterized by M, m, θ and ψ, which refer to as the main lobe gain, back lobe gain, the beam width of the main lobe gain and the angle from

the boresight direction, respectively.

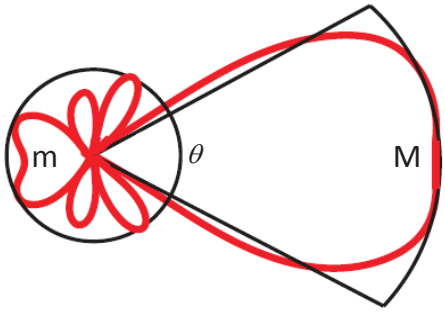

Figure 2.1. An example of the sectored antenna model.

2.2 Fundamentals of Stochastic Geometry

Stochastic geometry is a useful mathematical and statistical tool to characterize random spatial patterns of wireless networks [62, 63, 64, 65]. This tool has been widely used to analyze the system-level performance of cellular networks due to the tractability of the mathematical analysis. In stochastic geometry analysis, the network topology is modeled following a specific point process to capture the spatial randomness of the network. In this thesis, we employ the most popular point process namely the Poisson point process (PPP) [41, 62, 64] and Poisson cluster process (PCP) [65, 66, 67].

2.2.1 Poisson Point Process

Definition 2.1. (Poisson Point Process [62]):
A point process $\Phi = \{x_1, x_2, \cdots\} \subset \mathbb{R}^d$ is a PPP if and only if the number of points inside any compact set $\mathcal{B} \subset \mathbb{R}^d$ is a Poisson random variable, and the number of points in disjoint sets are independent.

Interference at a receiver is the sum of all interfering signals from random locations of undesired transmitters. The statistics of the interference can be

characterized using the stochastic geometry analysis.

Consider the following simple scenario: assume that the transmitters are randomly distributed in a two-dimensional Euclidean space $\mathbb{R}^2$ according to a homogeneous PPP Φ with intensity λ. From the view of a receiver at the location $\mathbf{x}$, all signals from the transmitters are regarded as interfering signals. In this case, because the locations of the transmitters follow a random point process, the overall interference, denoted by I, is a random variable. The distribution of I can be obtained by using the Laplace transform $\mathcal{L}(s) = \mathbb{E}[\exp(-sI)]$. Since I can be computed as the summation of the interfering signal from each transmitter, we have $I = \sum_{\mathbf{x}\in\Phi} L(\mathbf{x}, \mathbf{y})$, where its Laplace transform is given by

$$\mathcal{L}(s) = \mathbb{E}[\exp(-s \sum_{\mathbf{x}\in\Phi} L(\mathbf{x}, \mathbf{y}))] = \mathbb{E}\left[\prod_{\mathbf{x}\in\Phi} \exp(-sL(\mathbf{x}, \mathbf{y}))\right]. \tag{2.4}$$

The probability generating functional (PGFL) of PPP is defined as

$$\mathcal{G}(v) = \mathbb{E}\left[\prod_{\mathbf{x}\in\Phi} v(\mathbf{x})\right] = \exp\left(-\lambda \int_{\mathbb{R}^2} (1 - v(\mathbf{x}))\, d\mathbf{x}\right). \tag{2.5}$$

Thus, the Laplace transform in (2.4) is given by

$$\mathcal{L}(s) = \exp\left(-\lambda \int_{\mathbb{R}^2} (1 - \exp(-sL(\mathbf{x}, \mathbf{y}))\, d\mathbf{x}\right). \tag{2.6}$$

2.2.2 Poisson Cluster Process

Definition 2.2. (Poisson Cluster Process [65]):
A PCP results from applying homogeneous independent clustering to a stationary PPP. Specifically, the parent points form a stationary PPP Φ_p with intensity λ_p. The daughter point process, denoted by $\kappa^{\mathbf{x}}$, for a given parent $\mathbf{x}$ is a family of independent and identically distributed (i.i.d.) finite points with distribution

independent of the parent process. The complete PCP can be given as

$$\Phi_c = \bigcup_{\mathbf{x}\in\Phi_p} \kappa^{\mathbf{x}}. \tag{2.7}$$

Definition 2.3. If the number of points per cluster follows a Poisson distribution with intensity λ_d, such a PCP is referred to as a Neyman-Scott Process [65, Def. 3.4].

Denote by $G(v)$, $G_p(v)$ and $G_c(v)$ the generating functionals of Φ_c, Φ_p and $\kappa^{\mathbf{0}}$ processes, respectively. The generating functional is given by

$$\begin{aligned} G(v) &\overset{(a)}{=} G_p(G_{(\cdot)}(v)) \overset{(b)}{=} G_p(G_{(\mathbf{y})}(v)) \\ &\overset{(c)}{=} G_p(G_c(v(\mathbf{y}+\cdot))) \overset{(d)}{=} \mathbb{E}\left[\prod_{\mathbf{y}\in\Phi_p} G_c(v(\mathbf{y}+\cdot)\right] \\ &\overset{(e)}{=} \exp\left(-\int_{\mathbb{R}^2} \left(1 - G_c(v(\mathbf{y}+\cdot))\right) \Lambda(d\mathbf{y})\right), \end{aligned} \tag{2.8}$$

where (a)-(d) are from [62] and (e) is due to the generating functional of PPP. The generating functional of the representative cluster in (2.8) is given by

$$G_c(v(\mathbf{y}+\cdot)) = \mathbb{E}\left[\prod_{\mathbf{x}\in\kappa^{\mathbf{0}}} v(\mathbf{y}+\mathbf{x})\right]. \tag{2.9}$$

where $\kappa^{\mathbf{0}}$ is the daughter process of the representative cluster.

Chapter 3

Analytical Model for Outdoor Millimeter Wave Channels Using Geometry-Based Stochastic Approach

In this chapter, we develop a geometry-based stochastic channel model to statistically characterize the effect of all the first-order reflection paths between the transmitter and receiver. These first-order reflections are generated by the single-bounce of signals reflected from the walls of randomly distributed buildings. Based on this geometric model, a closed-form expression for the PDP contributed by all the first-order reflection paths is obtained and then used to evaluate their impact on the MMW outdoor propagation characteristics. Numerical results are provided to validate the accuracy of the proposed model under various channel parameter settings. The findings in this chapter provide a promising step towards more complex and practical MMW propagation channel modeling.

3.1 Chapter Introduction

Over the past decades, there has been a considerable amount of research on modeling the MMW propagation channel [68, 28, 3, 19, 38, 69, 70, 25]. Extensive propagation measurements have been conducted in [28, 3, 19], which revealed the unique characteristics of wireless propagation at MMW bands. Motivated by these characteristics, several attempts have been done on modeling the MMW channels, including deterministic and stochastic models. Deterministic models are typically based on ray tracing simulations [25, 71], which aim to produce accurate results via a detailed description of propagation environments. So they are costly and time-consuming especially when a large investigation area is considered. In addition, such results would be valid only for the particular propagation setting under investigation and may not be applicable to general propagation environments.

On the other hand, the stochastic approach that characterizes the channel behaviour using the probability distribution functions of the channel parameters is becoming a popular way to develop general yet sufficiently accurate channel models. Stochastic channel models can be further classified into two approaches, which are non-geometrical[28] and geometry-based [38, 69]. In [28], the authors proposed a non-geometrical channel model to statistically characterize the channel parameters, such as the number of scatterers, delay spread, path loss and shadowing, without any geometric assumptions. In contrast, the geometry-based channel models in [38, 69] were developed based on the predefined distributions of the channel parameters and distribution of effective scatterers with their geometric information such as angles of departure and arrival, and delay. All the parameters in [28, 38, 69] were obtained from an extensive set of channel measurements. However, parameterizations of these models are currently lacking because of the limited MMW channel measurement data.

The geometry-based stochastic approach has also been adopted in analytical

channel models. Examples are in [72, 73, 20]. Specifically, the authors in [72] modeled all the buildings in an urban area as random lattices with a constant occupancy probability. A closed-form expression for the propagation depth, i.e., the probability that a ray undergoes the successive reflection steps at a certain level of lattices, has been proposed based on the assumption that the ray enters the lattice area at a prescribed incident angle. In [73], the lattice environment in [72] was extended by removing the restriction of the incident angle. Such refinement was achieved by modeling the propagation depth for the source of ray that was placed inside the lattice. With such a system model, the authors considered the possibility of the successive reflections at all propagation angles. However, the existing models in [72, 73] have been mostly designed for the rich scattering environment, which will not be valid for the sparse MMW channels. Motivated by the previously discussed limitations, in this chapter we develop a stochastic MMW channel model by considering all the first-order reflection components of MMW signals in an urban area.

3.2 System Model

Consider an MMW communication link with a separation distance D between the transmitter Tx and receiver Rx, both of which are equipped with omnidirectional antennas with unit gains[1]. As illustrated in Fig. 3.1, the transmitter and receiver are located at $(-D/2, 0)$ and $(D/2, 0)$, respectively, and the communication link is surrounded by buildings that are randomly distributed in the communication area. For simplicity, we ignore the heights of all buildings and so a two-dimensional coordinate system as used in Fig. 3.1 is sufficient to describe

[1]Although directional antenna arrays are typically equipped in practical MMW cellular systems, we only consider an omnidirectional antenna system here to provide an antenna-independent channel model, which is desirable for the purpose of system analysis. A similar treatment has also been adopted in [20, 27, 38]. One would obtain the PDP with directional antenna by computing the convolution of the PDP with omni-directional antenna and the antenna geometries.

Table 3.1. Notation Summary

Notation	Description
λ	Point process of building centers
D	Distance between the transmitter and receiver
C	Center of building
l	Length of building
w	Length of building
θ	Orientation of building
L_r	The propagation distance of a first order reflection
τ	Propagation delay
c	The speed of light
f	The carrier frequency
λ_f	The signal wavelength of frequency f
$\rho(\tau)$	The path loss of a reflection path with propagation delay τ
Φ	The covered ratio
σ	The mean value of the reflection loss

the system. In addition, the following assumptions are made for all the buildings throughout this chapter.

1. Each building is of a rectangular shape specified by its center location C, length l, width w and orientation θ, where θ is defined as the anti-clockwise angle between the x-axis and the l-side of the building as shown in Fig. 3.1.

2. All the building centers $\{C\}$ form a homogeneous PPP with density λ.

3. The lengths and widths of all buildings follow, respectively, independent and identical distributions $f_L(l)$ and $f_W(w)$.

4. In each channel realization, the orientations of all buildings are the same, following a uniform distribution[2] over $(0, \pi]$.

5. The surfaces of all buildings are sufficiently smooth such that all the non-LoS paths follow the specular reflection law and the diffraction paths are

[2]This assumption is reasonable for modern cities where the buildings are normally aligned at the same angle, but may not be accurate in old cities. A further investigation for the area with different building orientations is left as a future work.

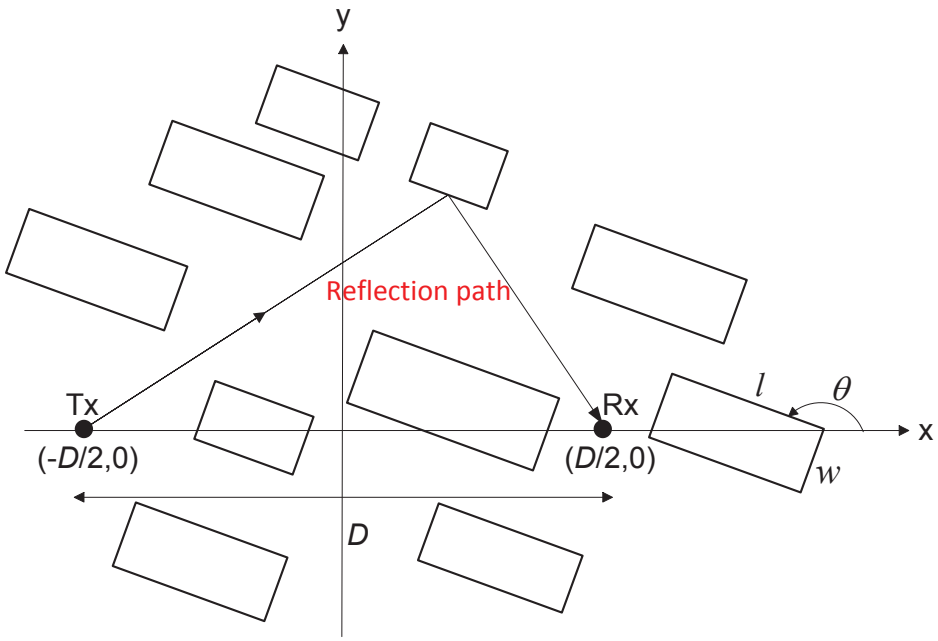

Figure 3.1. System model for outdoor communications.

negligible as this propagation mechanism contributes to insignificant signal strength at MMW bands [19, 70].

Table 3.1 contains the summary of notations used in this chapter. In this chapter, our main focus is on the characterization of the channel PDP contributed by all the first-order reflection paths.

3.3 Power Delay Profile Characterization

3.3.1 Derivation of PDP

In the above-considered system, the signal emitted from the transmitter may arrive at the receiver via multiple propagation paths. Besides a direct LoS path, any building in the communication area may potentially generate a reflection path, depending on its location and orientation. Meanwhile, each potential reflection path may also be blocked by some other buildings. Denote by L_r the propagation distance of a first-order reflection path, which corresponds to a propagation delay

of $\tau = L_r/c$ with c being the speed of light. The path loss along a reflection path with propagation delay τ is obtained by the Friss free space equation as [74]

$$\rho(\tau) = \left(\frac{\lambda_f}{4\pi L_r}\right)^2 \cdot \frac{1}{\sigma} = \frac{1}{(4\pi f\tau)^2 \sigma} \tag{3.1}$$

where $\lambda_f = c/f$ is the signal wavelength corresponding to the operating frequency f, and σ denotes the mean value of the reflection loss. The reflection loss needs to be considered here because in reality, when a signal is reflected, there must be some power loss due to the absorption by the medium. Note that in principle the value of the reflection loss depends on the incident angle, the properties of the building material, (i.e., the dielectric constant and the conductivity), the polarization of the incident wave, and the carrier frequency. However, taking all these effects into consideration will significantly complicate the analysis. For simplicity, in this chapter we use a constant mean value of the reflection loss σ and leave the detailed treatment of the reflection loss for future work. The mean value of σ is determined by exploiting the empirical model as in [75, 76]. A similar treatment has also been adopted in [77, 78, 26].

Denote by $\mathbb{E}(N_{RF}|\tau_1 \leq \tau \leq \tau_2)$ the average number of the first-order reflection paths with delays that are between τ_1 and τ_2. The density of the first-order reflection paths with time delay τ can be obtained by

$$f_{SR}(\tau) = \lim_{|\tau_2 - \tau_1| \to 0} \frac{\mathbb{E}(N_{RF}|\tau_1 \leq \tau \leq \tau_2)}{|\tau_2 - \tau_1|}. \tag{3.2}$$

Then the average path loss of all the first-order reflection paths with a specific common propagation delay τ can be modeled as

$$P(\tau) = \rho(\tau) \cdot f_{SR}(\tau). \tag{3.3}$$

In this chapter, we will derive an analytical expression for $f_{SR}(\tau)$ by considering

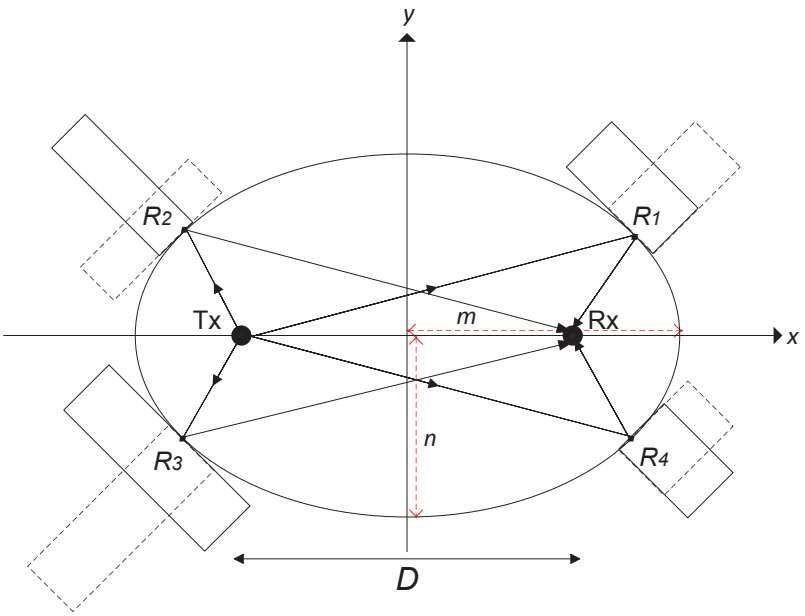

Figure 3.2. Examples of the reflection points on an ellipse with path length $c\tau$. All buildings in dashed and solid lines are, respectively, at the orientation of buildings $\theta \in (0, \pi/2]$ and $\theta \in (\pi/2, \pi]$.

the random locations, sizes, and orientations of buildings, as detailed below.

In real communication environments, a first-order reflection path with delay τ may be generated by a building with an arbitrary orientation θ. Thus, we can express the function $f_{SR}(\tau)$ as

$$f_{SR}(\tau) = \int_0^{\pi} f_{SR}(\tau|\theta) \cdot f_{\theta}(\theta)\, d\theta \tag{3.4}$$

where $f_{SR}(\tau|\theta)$ is the density of the first-order reflection paths with time delay τ when the building orientation is θ, and $f_{\theta}(\theta)$ is the probability density function (PDF) of orientation θ. From assumption 4, we have $f_{\theta}(\theta) = 1/\pi$.

Given the positions of the transmitter and receiver, a first-order reflection path can be completely determined by its reflection point. Since all the first-order reflection components with the same delay τ have the same path length L_r, their reflection points can be elegantly characterized by using an ellipse model as depicted in Fig. 3.2. The foci of this ellipse are chosen to be, respectively,

the transmitter Tx and receiver Rx located at $(-D/2, 0)$ and $(D/2, 0)$. Then the reflection points corresponding to the first-order reflection paths with the same delay τ all lie on this ellipse with proper major radius m and minor radius n, as illustrated in Fig. 3.2. Based on this ellipse model, we can readily conclude that, for a given value of building orientation θ, there are four possible locations of reflection points on the ellipse, which are denoted by R_1, R_2, R_3 and R_4 in Fig. 3.2, respectively. Consequently, we have four exclusive events of the first-order reflection paths with given τ and θ. Thus the function $f_{SR}(\tau|\theta)$ in (3.4) can be rewritten as

$$f_{SR}(\tau|\theta) = \sum_{i=1}^{4} f_{SR_i}(\tau|\theta) \tag{3.5}$$

where $f_{SR_i}(\tau|\theta)$ is the counterpart of $f_{SR}(\tau|\theta)$ contributed by the event when the reflection point is located at R_i. Note that since the derivations of these four terms in (3.5) are very similar to each other, our subsequent discussion will be mainly focused on the first term, $f_{SR_1}(\tau|\theta)$. In addition, we assume $\theta \in (\pi/2, \pi]$ in what follows, as the related derivations, though the same as those for the case of $\theta \in (0, \pi/2]$, involve slightly different notations.

Intuitively, a first-order reflection path that contributes to $f_{SR_1}(\tau|\theta)$ can be guaranteed if and only if the following two independent sub-events hold simultaneously: (a) there is a building with a proper location to generate such a first-order reflection path with its reflection point located at R_1, and (b) this reflection path is not blocked by any other buildings. Mathematically, we can further decompose the function $f_{SR1}(\tau|\theta)$ as

$$f_{SR_1}(\tau|\theta) = f_{RF_1}(\tau|\theta) \cdot f_{NB_1}(\tau|\theta) \tag{3.6}$$

where $f_{RF_1}(\tau|\theta)$ is the density of sub-event (a) and $f_{NB_1}(\tau|\theta)$ refers to the probability of sub-event (b). The detailed derivations of them are presented in, re-

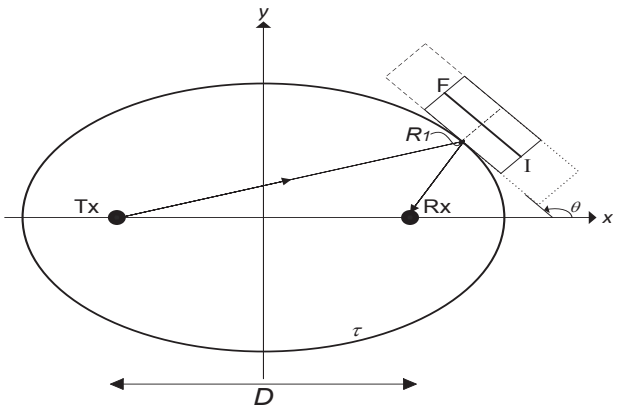

(a)

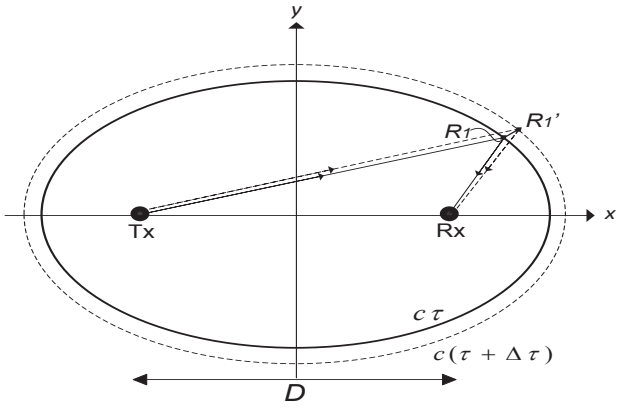

(b)

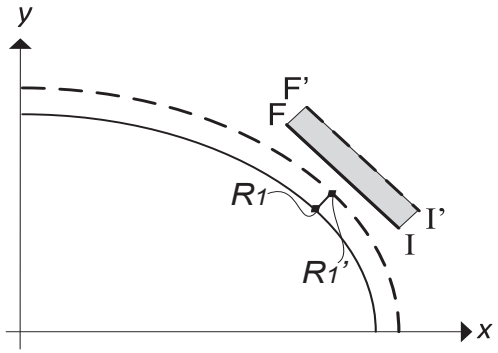

(c)

Figure 3.3. Ellipse model. (a) The possible locations of buildings that potentially generate a reflection path with R_1 being its reflection point. (b) Reflection paths with path lengths $c\tau$ and $c(\tau + \Delta\tau)$.(c) Geometry of the parallelogram $FF'I'I$.

spectively, subsections 3.3.2 and 3.3.3 below.

3.3.2 Derivation of $f_{RF_1}(\tau|\theta)$

To facilitate the derivation of $f_{RF_1}(\tau|\theta)$ in (3.6), we exploit the ellipse model as in Fig. 3.3(a) to describe the coordinates of the reflection point R_1, denoted by (x, y). Mathematically we have

$$\frac{x^2}{m^2} + \frac{y^2}{n^2} = 1 \tag{3.7}$$

where m and n are, respectively, the major radius and minor radius of the considered ellipse. Given the coordinates of the two foci, i.e., $(-D/2, 0)$ and $(D/2, 0)$, and the fact that the sum of the distances between any point on the ellipse and its two foci is the same and equals to $L_r = c\tau$, we have

$$m = \frac{c\tau}{2}, \tag{3.8}$$

and

$$n = \frac{1}{2}\sqrt{c^2\tau^2 - D^2}. \tag{3.9}$$

Recalling the assumption that $\theta \in (\pi/2, \pi]$, we can see that the tangent line of the ellipse across point R_1 is coincident with the l-side wall of the building that generates this first-order reflection path. Denote by φ the angle between the x-axis and this tangent line and recall that θ represents the orientation of all buildings. From Fig. 3.3 (a), we can express the slope of this tangent line by implicitly differentiating (3.7) with respect to x as

$$\tan\varphi = \tan\theta = \frac{dy}{dx} = \frac{-n^2 x}{m^2 y}, \tag{3.10}$$

or equivalently

$$y = \frac{-n^2 x}{m^2 \tan\theta}. \tag{3.11}$$

Combining (3.7), (3.8), (3.9) and (3.11), we can write the coordinates of point R_1 as

$$x = \frac{-c^2\tau^2 \tan\theta}{2\sqrt{c^2\tau^2 \sec^2\theta - D^2}}, \tag{3.12}$$

$$y = \frac{c^2\tau^2 - D^2}{2\sqrt{c^2\tau^2 \sec^2\theta - D^2}}. \tag{3.13}$$

Now, let us assume that the above-considered reflection path is generated by a building specified by the quadruple (C, l, w, θ). As illustrated in Fig. 3.3 (a), the reflection point R_1 may be at any point on the l-side wall of this building. As a consequence, the center of the building C may also have numerous possible locations, and all these locations form a line segment FI, where the two end points F and I correspond to the critical cases when R_1 falls on the two corners of the building.

In practice, the probability of the sub-event that there is a building capable of generating a first-order reflection path with its reflection point located at a specific point, e.g., R_1, is always zero. Therefore, in (3.6), we have defined $f_{RF_1}(\tau|\theta)$ as the density, instead of the probability, of such a sub-event. To derive the expression of $f_{RF_1}(\tau|\theta)$, we need to introduce a neighbourhood of R_1, which is denoted by $\mathcal{N}_{R_1}$. Consider the following event E_1: conditioned on that all buildings have orientation θ, there is at least one[3] properly located building that is capable of generating a first-order reflection path. Denote by $\mathbb{P}(E_1|\mathcal{N}_{R_1})$ the probability of

[3]In practice, buildings should not be overlapped, which is not guaranteed in the homogeneous PPP model in assumption 2. However, as the measure of the neighborhood $\mathcal{N}_{R_1}$ vanishes to zero, the overlapping probability will also converge to zero and thus the ignorance of overlapping will not cause any error in our model. A similar treatment has also been adopted in [20].

such a reflection path with its reflection point falling within the neighbourhood of R_1, $\mathcal{N}_{R_1}$. Then we can express $f_{RF_1}(\tau|\theta)$ as

$$f_{RF_1}(\tau|\theta) = \lim_{|\mathcal{N}_{R_1}|\to 0} \frac{\mathbb{P}(E_1|\mathcal{N}_{R_1})}{|\mathcal{N}_{R_1}|} \tag{3.14}$$

where $|\mathcal{N}_{R_1}|$ is the measure of $\mathcal{N}_{R_1}$.

In this chapter, we choose $\mathcal{N}_{R_1}$ to be the trajectory of R_1 when the path length varies from $c\tau$ to $c(\tau + \Delta\tau)$. Therefore, we have

$$|\mathcal{N}_{R_1}| = c(\tau + \Delta\tau) - c\tau = c\Delta\tau. \tag{3.15}$$

It can be expected that, as the path length increases from $c\tau$ to $c(\tau + \Delta\tau)$, the reflection point R_1 will gradually move outwards to another position denoted by R_1' in Fig. 3.3 (b). Consequently, the line segment FI will also gradually move outwards to another line segment denoted by $F'I'$ in Fig. 3.3 (c). In other words, $\mathbb{P}(E_1|\mathcal{N}_{R_1})$ in (3.14) is equal to the probability of the event that the center of the building falls in the region swept by the line segment FI during the movement. Note that this area may not be of a regular parallelogram shape, as the trajectory of the reflection point from R_1 to R_1' may not be a straightforward line segment. However, when $\Delta\tau \to 0$, we can asymptotically regard the trajectory of R_1R_1' as a line segment, and in turn regard the region $FF'I'I$ as a parallelogram, whose area is calculated in the following lemma.

Lemma 3.1. *When $\Delta\tau$ is sufficiently small, the area of the parallelogram $FF'I'I$ illustrated in Fig. 3.3 (c), which is denoted by $S_{FF'I'I}$, is given by*

$$S_{FF'I'I} = \frac{lc^2\tau\Delta\tau}{2\sqrt{c^2\tau^2 - D^2\cos^2\theta}}. \tag{3.16}$$

The detailed derivation of (3.16) can be found in Appendix A.1.

Next, let $\Phi(l, w)$ be a point process for the centers of buildings with the same

length l and width w. Since $\Phi(l,w)$ is a subset of the point process of the centers of all buildings $\{C\}$, it is thus a PPP with density $\lambda_{l,w} = \lambda f_L(l)dl f_W(w)dw$ [20]. Denote by $K_{RF_1}(l,w)$ the number of buildings falling in $S_{FF'I'I}$ with their centers belonging to $\Phi(l,w)$. Consequently, $K_{RF_1}(l,w)$ is a Poisson variable with expectation

$$\begin{aligned}\mathbb{E}[K_{RF_1}(l,w)] &= \lambda_{l,w} \cdot S_{FF'I'I} \\ &= \lambda_{l,w} \frac{lc^2\tau\Delta\tau}{2\sqrt{c^2\tau^2 - D^2\cos^2\theta}}.\end{aligned} \tag{3.17}$$

Note that $K_{RF_1}(l,w)$ is an independent Poisson random variable for different values of l and w. Thus, by the superposition property of Poisson random variables [62], the total number of buildings falling within $S_{FF'I'I}$ is $K_{RF1} = \sum_{l,w} K_{RF_1}(l,w)$. The expectation of K_{RF_1} is given by

$$\begin{aligned}\mathbb{E}[K_{RF_1}] &= \int_L \int_W \frac{\lambda l c^2\tau\Delta\tau}{2\sqrt{c^2\tau^2 - D^2\cos^2\theta}} f_W(w)\, f_L(l)\, dwdl \\ &= \lambda \frac{\mathbb{E}[l]c^2\tau\Delta\tau}{2\sqrt{c^2\tau^2 - D^2\cos^2\theta}}.\end{aligned} \tag{3.18}$$

Finally, on the basis of (3.18) and by recalling the definition of $f_{RF_1}(\tau|\theta)$ in (3.14), we have the following theorem.

Theorem 3.1. *The density of the sub-event that there is a building with orientation θ to generate a first-order reflection path with delay τ and its reflection point located at R_1, is given by*

$$f_{RF_1}(\tau|\theta) = \lambda \frac{\mathbb{E}[l]c\tau}{2\sqrt{c^2\tau^2 - D^2\cos^2\theta}}. \tag{3.19}$$

The proof of Theorem 3.1 can be found in Appendix A.2.

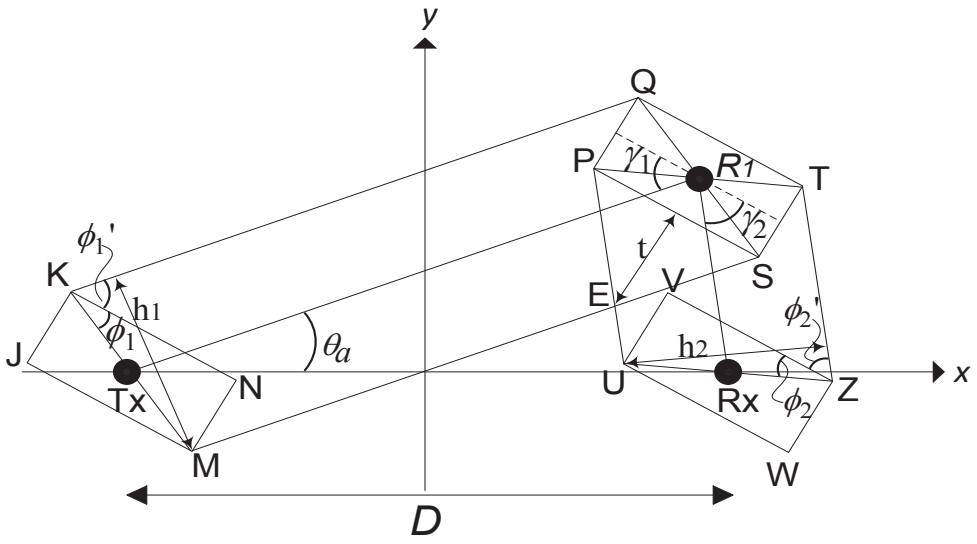

Figure 3.4. Geometry of the blockage region.

3.3.3 Derivation of $f_{NB_1}(\tau|\theta)$

Next, let us move our focus to the derivation of $f_{NB_1}(\tau|\theta)$ in (3.6). Suppose that there is a properly located building that can potentially generate a first-order reflection path with its reflection point being at R_1. As illustrated in Fig. 3.4, this potential reflection path consists of two line segments, i.e., TxR_1 and R_1Rx. It is therefore easy to see that this reflection path can practically exist only if neither of the two line segments, TxR_1 and R_1Rx, is blocked by other buildings. Following a similar argument as the blockage analysis of a LoS link in [20], we can conclude that, the probability that the line segment TxR_1 is not blocked by buildings with length l and width w is equal to the probability that there is no such buildings whose centers lie within the region $JKQTSM$ as illustrated in Fig. 3.4. Similarly, the blockage region for the line segment R_1Rx is the region $UPQTZW$. In summary, the probability $f_{NB_1}(\tau|\theta)$ contributed by buildings with length l and width w is equal to the probability that there are no such buildings whose centers lie within the blockage region $JKQTZWUEM$. This blockage

region is of a non-convex and irregular shape, whose area is given in the following lemma.

Lemma 3.2. *A simple yet accurate approximation for the area of the blockage region $JKQTZWUEM$, as illustrated in Fig. 3.4, is given by*

$$S_{JKQTZWUEM} \approx l\sqrt{c^2\tau^2 - D^2\cos^2\theta} + wD\,|cos\theta| + lw - \frac{l(c\tau - D)}{4} - \frac{l^2\sqrt{c^2\tau^2 - D^2}}{8D}. \tag{3.20}$$

The detailed derivation of (3.20) can be found in Appendix A.3.

Denote by $K_{NB_1}(l, w)$ the number of buildings with length l and width w whose centers fall in the blockage region $JKQTZWUEM$. Again, we can see that $K_{NB_1}(l, w)$ is a Poisson random variable with expectation

$$\begin{aligned}&\mathbb{E}[K_{NB_1}(l,w)] \approx \lambda_{l,w} \cdot S_{JKQTZWUEM} \\ &= \lambda_{l,w}\left(l\sqrt{c^2\tau^2 - D^2\cos^2\theta} + wD\,|cos\theta| + lw - \frac{l(c\tau - D)}{4} - \frac{l^2\sqrt{c^2\tau^2 - D^2}}{8D}\right).\end{aligned} \tag{3.21}$$

With $K_{NB_1}(l, w)$ being an independent Poisson random variable for a specific value of l and w, the total number of buildings falling within the blockage region $S_{JKQTZWUEM}$ is $K_{NB_1} = \sum_{l,w} K_{NB_1}(l, w)$, whose mean value can be calculated as

$$\begin{aligned}&\mathbb{E}[K_{NB_1}] \approx \int_L \int_W \mathbb{E}[K_{NB_1}(l,w)] f_W(w)\, f_L(l)\, dwdl \\ &= \lambda\left(\mathbb{E}[l]\sqrt{c^2\tau^2 - D^2\cos^2\theta} + \mathbb{E}[w]D\,|cos\theta| + \mathbb{E}[l]\mathbb{E}[w] - \frac{\mathbb{E}[l](c\tau - D)}{4}\right. \\ &\quad \left. - \frac{\mathbb{E}[l]^2\sqrt{c^2\tau^2 - D^2}}{8D}\right).\end{aligned} \tag{3.22}$$

Consequently, on the basis of (3.22), we have the following theorem.

Theorem 3.2. *Conditioned on that all buildings have orientation θ, the probability that a first-order reflection path with propagation delay τ and reflection point located at R_1, is not blocked by other buildings is given by*

$$f_{NB_1}(\tau|\theta) \approx \exp\Bigg(-\lambda\Bigg(\mathbb{E}[l]\sqrt{c^2\tau^2 - D^2\cos^2\theta} + \mathbb{E}[w]D\,|cos\theta| + \mathbb{E}[l]\mathbb{E}[w] - \frac{\mathbb{E}[l](c\tau - D)}{4} - \frac{\mathbb{E}[l]^2\sqrt{c^2\tau^2 - D^2}}{8D}\Bigg)\Bigg). \tag{3.23}$$

The proof of Theorem 3.2 is given in Appendix A.4.

3.3.4 Derivation of $f_{SR}(\tau)$

Combining the results derived in the previous two subsections, we are now ready to present the closed-form expression for $f_{SR}(\tau)$. Recalling the definition of a first-order reflection path in (3.6), we can rewrite the function $f_{SR_1}(\tau|\theta)$ by substituting (3.19) and (3.23) into (3.6) as

$$f_{SR_1}(\tau|\theta) \approx \frac{\lambda\mathbb{E}[l]c\tau}{2\sqrt{c^2\tau^2 - D^2\cos^2\theta}} \cdot \exp\Bigg(-\lambda\Bigg(\mathbb{E}[l]\sqrt{c^2\tau^2 - D^2\cos^2\theta} + \mathbb{E}[w]D\,|cos\theta| + \mathbb{E}[l]\mathbb{E}[w] - \frac{\mathbb{E}[l](c\tau - D)}{4} - \frac{\mathbb{E}[l]^2\sqrt{c^2\tau^2 - D^2}}{8D}\Bigg)\Bigg). \tag{3.24}$$

After similar derivations as those for (3.24), we can obtain

$$f_{SR_2}(\tau|\theta) \approx \frac{\lambda\mathbb{E}[w]c\tau}{2\sqrt{c^2\tau^2 - D^2\cos^2\theta}} \cdot \exp\Bigg(-\lambda\Bigg(\mathbb{E}[w]\sqrt{c^2\tau^2 - D^2\cos^2\theta} + \mathbb{E}[l]D\,|cos\theta| + \mathbb{E}[w]\mathbb{E}[l] - \frac{\mathbb{E}[w](c\tau - D)}{4} - \frac{\mathbb{E}[w]^2\sqrt{c^2\tau^2 - D^2}}{8D}\Bigg)\Bigg), \tag{3.25}$$

$$f_{SR_3}(\tau|\theta) = f_{SR_1}(\tau|\theta), \tag{3.26}$$

and

$$f_{SR_4}(\tau|\theta) = f_{SR_2}(\tau|\theta). \tag{3.27}$$

Therefore, we have

$$\begin{aligned} f_{SR}(\tau|\theta) &= \sum_{i=1}^{4} f_{SR_i}(\tau|\theta) \\ &\approx \frac{\lambda\mathbb{E}[l]c\tau}{\sqrt{c^2\tau^2 - D^2\cos^2\theta}} \cdot \exp\Bigg(-\lambda\Bigg(\mathbb{E}[l]\sqrt{c^2\tau^2 - D^2\cos^2\theta} + \mathbb{E}[w]D\,|cos\theta| \\ &\quad + \mathbb{E}[l]\mathbb{E}[w] - \frac{\mathbb{E}[l](c\tau - D)}{4} - \frac{\mathbb{E}[l]^2\sqrt{c^2\tau^2 - D^2}}{8D}\Bigg)\Bigg) \\ &\quad + \frac{\lambda\mathbb{E}[w]c\tau}{\sqrt{c^2\tau^2 - D^2\cos^2\theta}} \cdot \exp\Bigg(-\lambda\Bigg(\mathbb{E}[w]\sqrt{c^2\tau^2 - D^2\cos^2\theta} + \mathbb{E}[l]D\,|cos\theta| \\ &\quad + \mathbb{E}[w]\mathbb{E}[l] - \frac{\mathbb{E}[w](c\tau - D)}{4} - \frac{\mathbb{E}[w]^2\sqrt{c^2\tau^2 - D^2}}{8D}\Bigg)\Bigg). \end{aligned} \tag{3.28}$$

Note that the expression (3.28) is derived based on the assumption of $\theta \in (\pi/2, \pi]$ defined in Section 3.3.1. For the case when $\theta \in (0, \pi/2]$, as illustrated in Fig. 3.2, we can see that the angle between the x-axis and the tangent line of the ellipse across point R_1 is $\varphi = \theta + \frac{\pi}{2}$. Hence following a similar derivation as (3.10), the slope of the tangent line across point R_1 in this case is given by

$$\tan\varphi = \tan\left(\theta + \frac{\pi}{2}\right) = \frac{dy}{dx} = \frac{-n^2x}{m^2y}. \tag{3.29}$$

Next, to obtain the function $f_{SR}(\tau|\theta)$ for the case when $\theta \in (0, \pi/2]$, we can follow the similar derivations as those from (3.5) to (3.28), except that we replace the expression for the slope of the tangent line in (3.10) with (3.29) and exchange the

building parameter l and w. Thus, we have

$$
\begin{aligned}
f_{SR}(\tau|\theta) &= \sum_{i=1}^{4} f_{SR_i}(\tau|\theta) \\
&\approx \frac{\lambda \mathbb{E}[w] c\tau}{\sqrt{c^2\tau^2 - D^2\cos^2\varphi}} \cdot \exp\Bigg(-\lambda\Bigg(\mathbb{E}[w]\sqrt{c^2\tau^2 - D^2\cos^2\varphi} + \mathbb{E}[l]D\,|cos\varphi| \\
&\quad + \mathbb{E}[w]\mathbb{E}[l] - \frac{\mathbb{E}[w](c\tau - D)}{4} - \frac{\mathbb{E}[w]^2\sqrt{c^2\tau^2 - D^2}}{8D}\Bigg)\Bigg) \\
&\quad + \frac{\lambda \mathbb{E}[l] c\tau}{\sqrt{c^2\tau^2 - D^2\cos^2\varphi}} \cdot \exp\Bigg(-\lambda\Bigg(\mathbb{E}[l]\sqrt{c^2\tau^2 - D^2\cos^2\varphi} + \mathbb{E}[w]D\,|cos\varphi| \\
&\quad + \mathbb{E}[l]\mathbb{E}[w] - \frac{\mathbb{E}[l](c\tau - D)}{4} - \frac{\mathbb{E}[l]^2\sqrt{c^2\tau^2 - D^2}}{8D}\Bigg)\Bigg)
\end{aligned} \tag{3.30}
$$

where $\varphi = \theta + \frac{\pi}{2}$.

Finally, by substituting (3.28) and (3.30) into (3.4), we can obtain the closed-form expression for $f_{SR}(\tau)$ as

$$
\begin{aligned}
f_{SR}(\tau) \approx\ & \zeta_1\left(\frac{8\eta}{\pi}(1+\eta\beta_1)tanh^{-1}\left(\frac{\pi}{8\eta^2}\right) - \beta_1\right) \\
& + \zeta_2\left(\frac{8\eta}{\pi}(1+\eta\beta_2)tanh^{-1}\left(\frac{\pi}{8\eta^2}\right) - \beta_2\right)
\end{aligned} \tag{3.31}
$$

where

$$\zeta_1 = \lambda\mathbb{E}[l]a\exp\left(\lambda\mathbb{E}[l]\left(\frac{D(a-1)}{4} - D\eta - \mathbb{E}[w]\right) + \frac{\lambda\mathbb{E}[l]^2\sqrt{a^2-1}}{8}\right)$$
$$\times \exp\left(\frac{\lambda\mathbb{E}[w]D(a-\eta)}{\sqrt{a^2-1}-a}\right)$$
$$\zeta_2 = \lambda\mathbb{E}[w]a\exp\left(\lambda\mathbb{E}[w]\left(\frac{D(a-1)}{4} - D\eta - \mathbb{E}[l]\right) + \frac{\lambda\mathbb{E}[w]^2\sqrt{a^2-1}}{8}\right)$$
$$\times \exp\left(+\frac{\lambda\mathbb{E}[l]D(a-\eta)}{\sqrt{a^2-1}-a}\right)$$
$$\beta_1 = \lambda D\left(\mathbb{E}[l] + \frac{\mathbb{E}[w]}{\sqrt{a^2-1}-a}\right)$$
$$\beta_2 = \lambda D\left(\mathbb{E}[w] + \frac{\mathbb{E}[l]}{\sqrt{a^2-1}-a}\right)$$
$$\eta = \sqrt{a^2-(1/2)}$$
$$a = \frac{L_r}{D} = \frac{c\tau}{D}.$$

The detailed derivation of (3.31) can be found in Appendix A.5.

3.3.5 PDP and Average Number of the First-Order Reflection Paths

We now return to the PDP contributed by all the first-order reflection paths as defined in (3.3). Substituting (3.31) into (3.3), we have

$$P(\tau) \approx \rho(\tau)\cdot\left(\zeta_1\left(\frac{8\eta}{\pi}(1+\eta\beta_1)tanh^{-1}\left(\frac{\pi}{8\eta^2}\right)-\beta_1\right)\right.$$
$$\left.+\zeta_2\left(\frac{8\eta}{\pi}(1+\eta\beta_2)tanh^{-1}\left(\frac{\pi}{8\eta^2}\right)-\beta_2\right)\right). \tag{3.32}$$

In brief, the values of $\zeta_1, \zeta_2, \beta_1$ and β_2 in (3.32) all depend on the average dimensions of the buildings $\mathbb{E}[l]$ and $\mathbb{E}[w]$, and the density of the buildings λ. Thus we can conclude that the behavior of PDP contributed by all the first order reflection paths varies with these environment parameters. We will further discuss the

effect of these parameters in the next section.

Note that, although the resultant expression (3.32) is a bit complicated, it is much more efficient to be used for analyzing the PDP compared to numerical simulations. Therefore, the derived expression can effectively facilitate the system modeling and greatly reduce the time for numerical simulations, which is the key contribution of our work.

On top of (3.32), we can obtain the total path loss of a link by combining the average path loss of an LoS component and the average path loss of the first-order reflection paths, which are denoted by $\mathbb{E}[P_{LoS}]$ and $\mathbb{E}[P_{Ref}]$, respectively. The total path loss of a link is given by

$$\mathbb{E}[P_t] = \mathbb{E}[P_{LoS}] + \mathbb{E}[P_{Ref}]. \tag{3.33}$$

In (3.33), the average path loss of the LoS component is given by [20]

$$\begin{aligned}\mathbb{E}[P_{LoS}] =& \frac{1}{(4\pi f \tau_0)^2} \cdot \\ & \exp\left(-\frac{2\lambda(\mathbb{E}[L]+\mathbb{E}[W])D}{\pi} - \lambda\mathbb{E}[L]\mathbb{E}[W]\right)\end{aligned} \tag{3.34}$$

and the average path loss of the first-order reflection paths can be obtained by

$$\mathbb{E}[P_{Ref}] = \int_{\tau_0}^{\tau_{max}} P(\tau)\, d\tau. \tag{3.35}$$

In (3.35), τ_0 is the minimum propagation delay of all the first-order reflection paths, which is lower bounded by the propagation delay of the LoS path, i.e., we can set $\tau_0 = D/c$. Similarly, τ_{max} is the maximum propagation delay of all first-order reflection paths, which should be set as $\tau_{max} = +\infty$ theoretically.

As a by-product, the average number of the first-order reflection paths, which

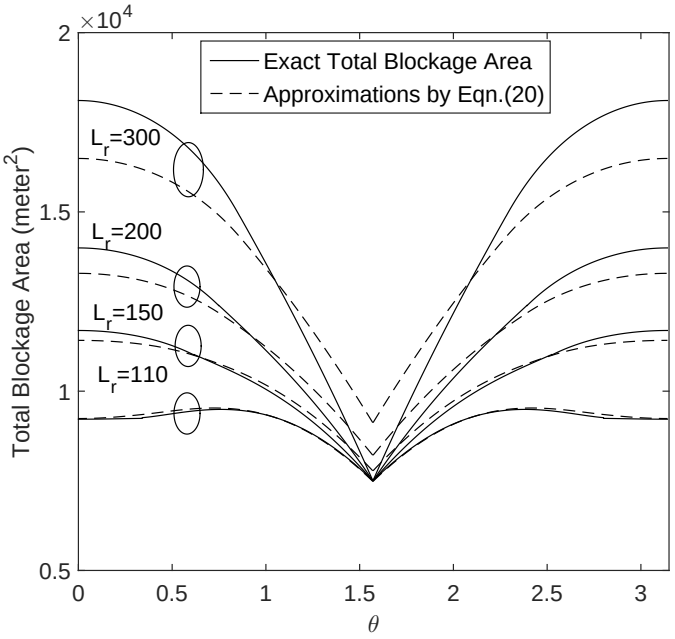

Figure 3.5. Comparison between the exact and approximated total blockage area for the orientation of buildings $\theta \in (0, \pi)$.

is denoted by $\mathbb{E}[f_{SR}]$, can be derived from (3.31) as

$$\mathbb{E}[f_{SR}] = \int_{\tau_0}^{\tau_{max}} f_{SR}(\tau)\, d\tau. \tag{3.36}$$

3.4 Numerical Results and Discussions

In this section, we will present some numerical examples to validate the accuracy of the proposed analytical model and discuss the impact of environment features, e.g., building dimensions and density, on the PDP and the average number of the first-order reflection paths.

3.4.1 Validation of the Blockage Area Approximation (3.20)

First, let us verify the accuracy of the blockage area approximation in (3.20). In Fig. 3.5, both the exact total blockage area and the approximation (3.20) are plotted as functions of the building orientation θ when $D = 100$ m, $l = 55$ m and $w = 50$ m. After comparison, we observe that the approximation involved

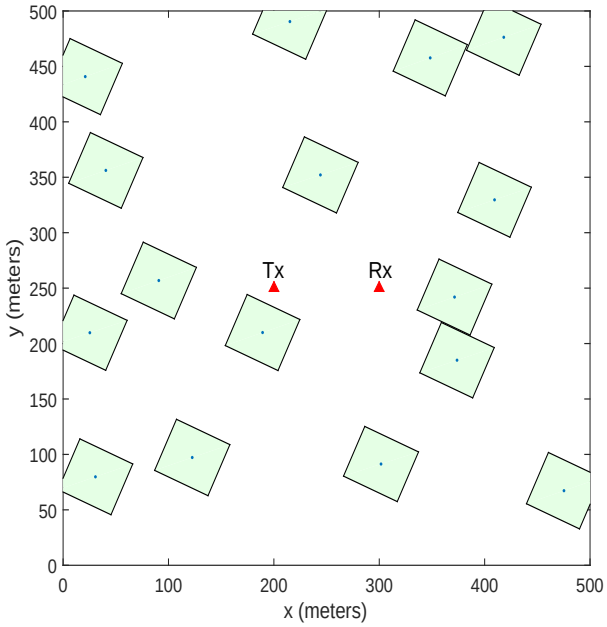

Figure 3.6. An example of a point-to-point link with distance $D = 100$ m. This link is surrounded by randomly located buildings with $l \in [54, 56]$ and $w \in [49, 51]$.

in (3.20) is very accurate for small values of the path length L_r in the whole interval $\theta \in (0, \pi]$. Though the gap between the exact and approximation curves becomes visible as the value of L_r increases, we observe that by using (3.20), we will underestimate the blockage area when the value of θ is close to 0 or π, and overestimate the blockage area when the value of θ is close to $\pi/2$. Recall from (3.4) that the function $f_{SR}(\tau)$ involves the integration with respect to θ from 0 to π. Intuitively, after performing the integration, we can expect that the overestimated and underestimated areas will cancel each other to a certain extent and reduce the approximation error. We will further verify the accuracy of this approximation in the next subsection.

3.4.2 Effects of Environment Parameters on PDP

We now set about validating our analytical results and discussing the effect of environment features on the PDP contributed by all the first-order reflection paths. We consider a point-to-point link with distance $D = 100$ m and operating frequency $f = 73$ GHz. Both the transmitter and receiver are equipped with a single

omnidirectional antenna with unit gain. Such a link is surrounded by randomly distributed and identically orientated buildings. The lengths and widths of the buildings are uniformly distributed in certain intervals. The center locations of all the buildings in this area form a homogeneous PPP with density λ. For the ease of subsequent discussions, we denote Φ as the fraction of land covered by buildings in the investigated area, i.e., $\Phi = 1 - \exp(-\lambda \mathbb{E}[l]\mathbb{E}[w])$[20], which we refer to as the covered ratio.

Given the detailed parameter setting in the above system, the PDP contributed by all the first-order reflection paths can be analytically obtained by (3.32). Besides, we also provide the simulation results of the PDP contributed by all the first-order reflection paths in the following way. We consider a square area[4] of 500×500 m^2 as illustrated in Fig. 3.6, where the transmitter and receiver are located at $(200\text{m}, 250\text{m})$ and $(300\text{m}, 250\text{m})$, respectively. In each channel realization, we first randomly generate buildings within this square area based on the given building parameters. Then we follow the ray-tracing principle and the law of reflection to check if every single side wall of each building is able to generate a first-order reflection path between the transmitter and receiver. The blockage status of the potential first-order reflection paths is then further verified. We set the reflection loss $\sigma = 3$ dB. Each first-order reflection path is specified by its time delay, and the corresponding path loss can be calculated consequently. After simulating a sufficiently large number of channel realizations, we sort all the collected first-order reflection paths by their time delays and classify them into pre-partitioned time delay intervals. Finally, the sum path loss of all the first-order reflection paths in each interval is divided by the product of the interval width and the total number of channel realizations. The resultant ratios

[4]An infinite area should be considered here theoretically, but this is impossible in simulations. However, we argue that only considering such a finite square area is sufficient, as the PDP is mainly contributed by short reflection paths and the received power through those long reflection paths is very insignificant after much severer propagation loss. We have numerically verified this via varying the size of this square area.

are referred to as the simulated PDP contributed by all the first-order reflection paths.

Fig. 3.7 compares the analytical and simulated PDPs under various building environments. In each sub-figure of Fig. 3.7, three values of the covered ratio, i.e., $\Phi = 0.05, 0.2$ and 0.4, are considered, which represent sparse, medium and dense building environments, respectively. In addition, three different pairs of length and width distributions are considered in Figs. 3.7(a), 3.7(b) and 3.7(c) to observe the effect of the building dimensions on PDP. Specifically, we assume the uniform distributions of $l \in$ [9 m,11 m] and $w \in$ [9 m,11 m] in Fig. 3.7(a); those of $l \in$ [54 m,56 m] and $w \in$ [49 m,51 m] in Fig. 3.7(b), and those of $l \in$ [149 m,151 m] and $w \in$ [149 m,151 m] in Fig. 3.7(c), which represent small, medium and large sizes of buildings, respectively. From these figures[5], we can make the following observations.

- The analytical PDP derived in (3.32) is numerically very accurate in all scenarios, which indicates that the error incurred by the blockage area approximation in (3.20) is negligible. Note that the calculation of equation (3.32) only takes less than a second, whereas the time of obtaining those simulation curves in Fig. 3.7 is measured in days. Therefore, though the expression in equation (3.32) looks complex, it provides a very efficient way to analyze the PDP.

- Given the distributions of building dimensions, there exists the most preferable value of covered ratio between 0 to 1 that leads to the maximum PDP curve. This is straightforward as in one extreme of $\Phi = 0$, there is no building to generate reflections, whereas in another extreme of $\Phi = 1$, the land is all covered by buildings and so all potential reflection paths will be blocked. Therefore, the value of Φ that leads to the maximum PDP curve

[5]Note that the simulated PDP for the case of $\Phi = 0.4$ is not presented in Fig. 3.7(a), because the related simulation is measured in months and very time-consuming.

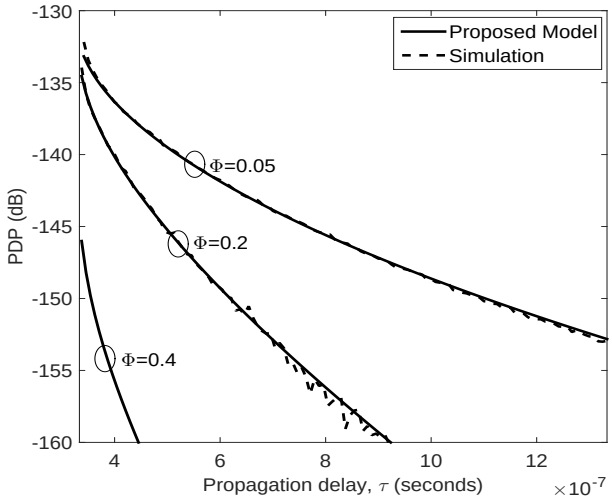

(a)

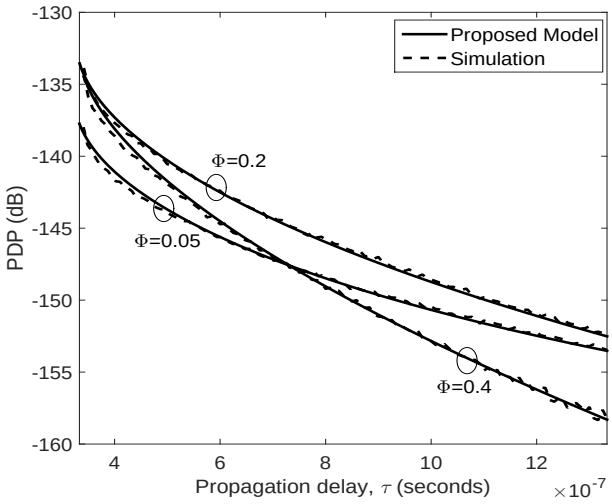

(b)

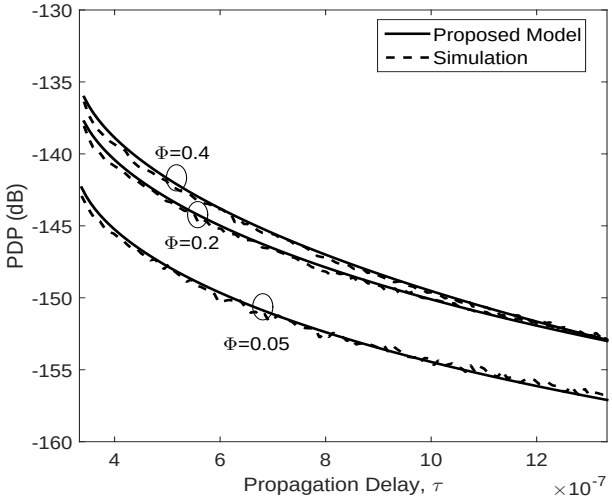

(c)

Figure 3.7. Comparison between analytical and simulated PDP. The dimensions of buildings are (a) $l \in$ [9 m,11 m] and $w \in$ [9 m,11 m], (b) $l \in$ [54 m,56 m] and $w \in$ [49 m,51 m], (c) $l \in$ [149 m,151 m] and $w \in$ [149 m,151 m].

must fall between 0 and 1.

- The most preferable value of Φ increases with the sizes of buildings, i.e., the length and width. For example, with small buildings in Fig. 3.7(a), the PDP curve for $\Phi = 0.05$ is the highest among the three PDP curves. As the building sizes increase, in Fig. 3.7(b) and Fig. 3.7(c), the highest ones are achieved when $\Phi = 0.2$ and 0.4, respectively. Thus we can have this observation qualitatively.

- The PDP curves decrease faster with the time delay τ when the building size is smaller or the covered ratio is larger. For example, by comparing the PDP curves for the case of $\Phi = 0.05$ in all subfigures, it is seen that the slope of the PDP curve in Fig. 3.7(a), i.e., for small buildings, is sharper than the other PDP curves. In addition, it is also seen from Fig. 3.7(a) that the PDP curve for $\Phi = 0.4$ has the sharpest slope among other PDP curves. This is because the existence of dense buildings in small dimensions will significantly increase the blockage probability of the first-order reflection paths.

Next, we compare the average path loss contributed by the first-order reflection paths in (3.35) with the average path loss contributed by the LoS path in (3.34). We use the same system setting and building parameters as in Fig. 3.7. Thus, we have the lower bound of the time delay in (3.35) $\tau_0 = D/c = 0.33\mu s$. To facilitate the numerical integration in (3.35), we set the upper bound in (3.35) to be a sufficiently large but finite value[6]. Fig. 3.8 plots the average path loss contributed by the first-order reflection paths and LoS path as functions of covered ratio Φ. From this figure, we can make the following observations.

[6]Theoretically, τ_{max} should be $+\infty$, but it is impossible in the numerical integration. However, the finite value of τ_{max} is a reasonable setting because in practice, the reflected waves with long delays contribute to insignificant received powers, which can be ignored. A similar treatment has also been adopted in [79, 80].

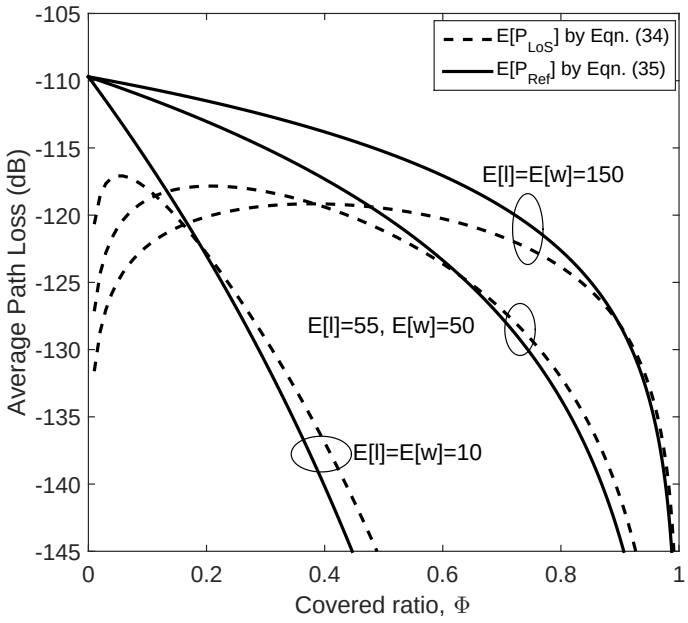

Figure 3.8. Effect of the covered ratio on the average path loss.

- Different from the monotonously decreasing LoS curves, the average path loss contributed by the first-order reflection paths exhibits as a concave function of the covered ratio. The optimal scenario that leads to the minimum absolute value of the average path loss occurs when Φ is between 0 and 1.

- In systems with Φ higher than this optimal scenario, the average path loss contributed by all the first-order reflection paths becomes comparable with that contributed by the LoS path, indicating that the reflection paths are not ignorable in these cases.

- The value of Φ corresponding to this optimal scenario increases as the size of buildings increases. For example, it is seen from Fig. 3.8 that the most preferable value of covered ratio for the small, medium and large buildings, are respectively around, $\Phi = 0.05$, $\Phi = 0.2$ and $\Phi = 0.4$.

Then, in Fig. 3.9, we plot the total path loss, the average path loss of the LoS and the average path loss of the first-order reflection paths, which are respectively

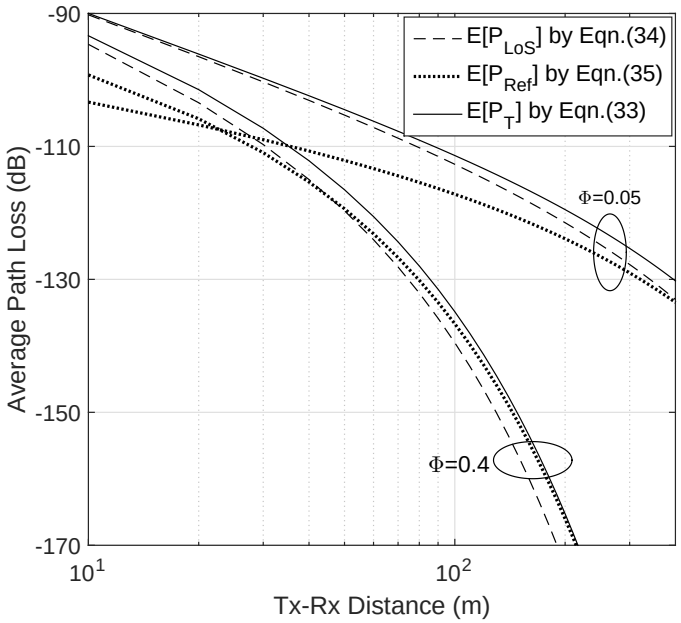

Figure 3.9. Effect of Tx-Rx distance on the average path loss.

obtained by (3.33), (3.34) and (3.35), as functions of Tx-Rx distance D. We use the average sizes of building $\mathbb{E}[L] = \mathbb{E}[W] = 10$ m, which represent small sizes of buildings. Two values of covered ratio Φ are considered, i.e., $\Phi = 0.05$ and 0.4. From this figure, we can make the following observations.

- In the system with a low value of Φ, the total path loss is dominated by the contribution of the LoS path, especially at the short Tx-Rx distance.
- Given the average sizes of buildings, there exist an optimum value of D at which both the LoS and the first-order reflection paths contribute to the same average path loss.
- The value of the optimal D decreases as the covered ratio Φ increases. From Fig. 3.9, it is seen that the value of the optimal D for the covered ratio $\Phi = 0.05$ and $\Phi = 0.4$, are respectively, 390 m and 30 m.

The same observations are found for the cases of medium and large sizes of buildings.

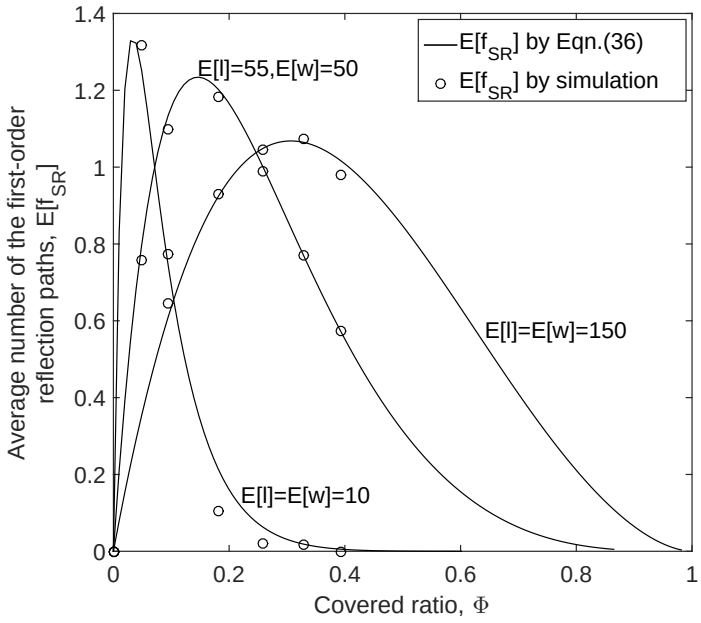

Figure 3.10. Effect of the covered ratio on the average number of the first-order reflection paths.

3.4.3 Average Number of the First-Order Reflection Paths

Finally, we discuss the effect of the environment features on the average number of the first-order reflection paths $\mathbb{E}[f_{SR}]$. Fig. 3.10 plots both the semi-analytical and simulated $\mathbb{E}[f_{SR}]$ as functions of covered ratio Φ, where the solid curves are calculated based on (3.36) and numerical integration, and the black circles are simulation results obtained by the same simulation process as in Section 3.4.2. The following observations are made from Fig. 3.10.

- The semi-analytical $\mathbb{E}[f_{SR}]$ in (3.36) is accurate in all scenarios. Although we are unable to derive the closed expression for $\mathbb{E}[f_{SR}]$, the semi-analytical expression in (3.36) provides an efficient way to analyze the contribution of the first-order reflection paths.

- All $\mathbb{E}[f_{SR}]$ curves exhibit a unimodal property in the range $\Phi \in [0, 1]$. These curves first increase monotonically as Φ increases from zero. After achieving their maximum points, these curves decrease with the increasing value of Φ.

- There exists a peak point for each $\mathbb{E}[f_{SR}]$ curve, which indicates the most preferable value of the covered ratio that leads to the maximum $\mathbb{E}[f_{SR}]$. The most preferable value of the covered ratio Φ increases with the size of buildings. This observation is consistent with the behavior of PDP in Section 3.4.2.

3.5 Chapter Summary

In this chapter, we proposed a novel geometry based channel model to evaluate the PDP contributed by all the first-order reflection paths. From the developed model, we investigated the effects of building density and sizes on the PDP and the average number of the first-order reflection components. The results show that the behavior of the PDP depends on the building sizes and density. Small building size and large covered ratio may lead to a significant decrease in PDP. Also, the results demonstrate that there exits an optimal communication distance that render the comparable power between the reflection paths and the LoS path. The findings in this chapter can provide useful insights to develop more complex channel models applicable to future MMW systems.

Chapter 4

Multi-cell Coordination via Disjoint Clustering in Dense Millimeter Wave Cellular Networks

This chapter investigates the performance of base station (BS) coordination via disjoint clustering in dense MMW cellular networks. Using tools from stochastic geometry, we derive the coverage probability and area spectral efficiency (ASE) by incorporating the key features of MMW systems, i.e., blockage and directional antennas. Simulation results are provided to validate the accuracy of the analytical results under various system parameters and demonstrate the performance superiority of BS coordination via disjoint clustering over the non-coordinated case. The results also suggest that the optimal cluster size to achieve the maximum ASE increases as the blockage factor, which is determined by the density and the average size of the buildings, decreases.

4.1 Chapter Introduction

The concept of BS cooperation for inter-cell interference mitigation has been extensively studied in the past decades, see, e.g., [40, 41, 42, 43, 44]. Specifically, numerical simulations with the assumption that the network follows a hexagonal grid model has been conducted in [40] to evaluate the performance of large-scale cellular networks. The simulation-based approach is often time-consuming and may require a massive set of data to provide insights into the effect of system parameters. Alternatively, stochastic geometry approach, which can provide accurate and tractable analytical results, has been widely used in recent years to analyze the coverage and rate of cellular networks. By using stochastic geometry, the works in [41, 42, 43, 44] assume that the locations of BSs are randomly distributed following a Poisson point process (PPP). An exact expression of the coverage probability for a typical user with pairwise BS cooperation has been derived in [41]. In [42] and [43], benefits of beam-forming coordination in multi-cell networks are analyzed. With the use of appropriate precoding, interference signals from base-stations within the same cluster can be canceled out. On the other hand, inter-cell scheduling among BSs within a cluster has been proposed in [44]. It was assumed that only one BS in a cluster transmits at each scheduling instance. Such a scheduling scheme has been proven to successfully eliminate the intercell interference and provides higher spectral efficiency than the full frequency reuse scheme. However, the works in [42, 43, 44] focus primarily on microwave cellular systems where the analysis does not incorporate the unique channel characteristics and antenna features for the MMW networks.

More recently, cooperative multipoint transmission at MMW frequencies has been analyzed based on the stochastic geometry approach in [81]. The effects of non-fading and fading environments on the SINR coverage were analyzed under the assumption that each user is served by a user-centric cluster of BSs. Although the user-centric clustering scheme has been shown to improve the user

performance especially for the cluster edge user, it still face many technical challenges including plenty of channel state information (CSI) acquisition overhead, high computational complexity and limited backhaul networks [82].

Different from the work in [81], we consider a disjoint clustering approach where a finite number of BSs is grouped to form multiple cooperation clusters. The disjoint clustering is considered as a practical clustering method because it only requires the CSI between all BSs and users to be shared among BSs in the same cluster. Thus, the amount of CSI overhead is much smaller than in the user-centric method [42]. We propose cluster-based intercell scheduling to mitigate the intra-cluster interference signals. Characterizing the system performance in such a multi-cell coordination strategy is a non-trivial problem, due to the location-dependent of the resulting active BSs in each cluster. In this chapter, we present analytical frameworks to analyze the coverage probability at the receiver and ASE of the MMW system. The findings in this chapter provide useful insights into the mitigation of inter-cell interference with BS clustering in the MMW cellular systems.

4.2 System Model

4.2.1 Network Model

As shown in Fig. 4.1, we consider a MMW cellular network with randomly distributed BSs in a two-dimensional Euclidean space $\mathbb{R}^2$ according to a homogeneous PPP Φ with intensity λ. All BSs are assumed to have a constant transmit power P_t. The entire network is divided into non-overlapping clusters, where each cluster consists of a finite number of collocated BSs. Following the conventional assumption on BS clusters [43, 83, 42], we generate the clusters by placing a uniform square lattice with sides of length W on $\mathbb{R}^2$.

The locations of users are modeled following another homogeneous PPP Φ_u

Table 4.1. Notation Summary

Notation	Description
Φ,λ	Point process and intensity of BSs.
Φ_u,λ_u	Point process and intensity of UEs.
p_L,p_N	Probability of LoS and non-LoS.
a_L,a_N	Path loss exponents for LoS and non-LoS.
β	Blockage factor.
δ	Path loss intercept.
BW	MMW bandwidth.
σ^2	Noise.
M_b, m_b, ω_b	Main lobe gain, back lobe gain and main lobe beamwidth of the BS.
M_u	Antenna gain of the user
$G(\theta)$	Antenna gain as a function of steering angle.
θ	The steering angle.
P_t	The transmit power.
W	The side of a square.

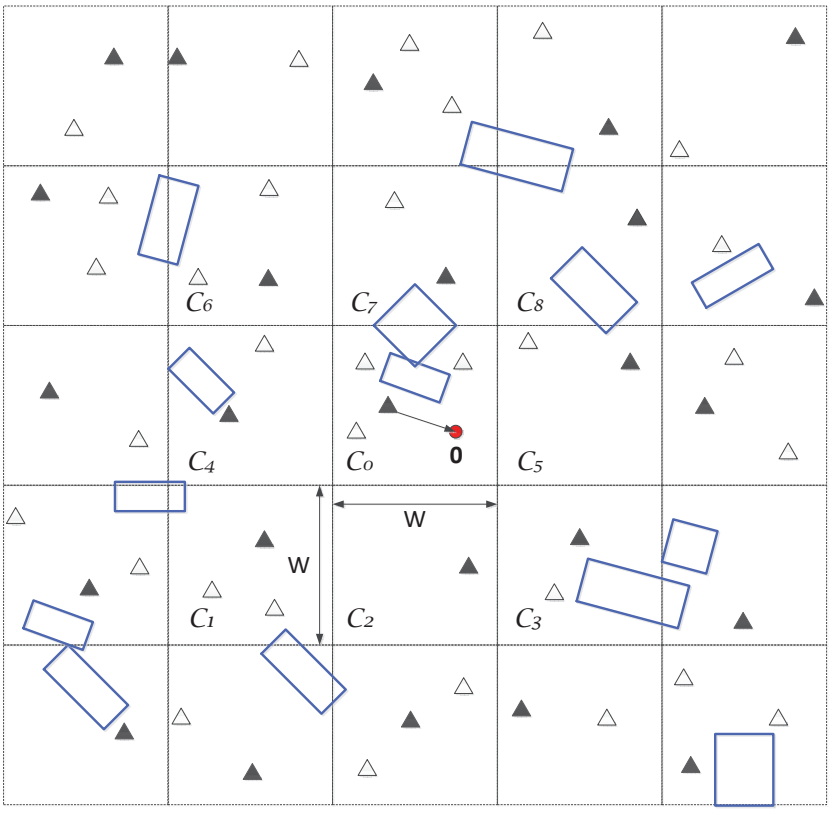

Figure 4.1. System model for MMW cellular networks with random buildings. The blue rectangles represents the random buildings. The red circle represents the typical user. The shaded triangles are the active nodes and the clear triangles are the inactive nodes.

with intensity λ_u. The communications between users and their associated BSs are surrounded by randomly distributed buildings in the communication area. Due to the presence of these buildings, the BS can be either line-of-sight (LoS) or non-LoS to its associated user. We adopt the blockage model in [20, 84] to characterize the blockage effects on the system performance. By incorporating such a model, the probabilities of LoS and non-LoS links, are respectively given by, $p_L(\mathbf{x},\mathbf{y}) = e^{-\beta|\mathbf{x}-\mathbf{y}|}$ and $p_N(\mathbf{x},\mathbf{y}) = 1 - e^{-\beta|\mathbf{x}-\mathbf{y}|}$, where $|\mathbf{x}-\mathbf{y}|$ represents the distance from $\mathbf{x}$ to $\mathbf{y}$ and β is the blockage factor, which is determined by the density and the average size of the buildings. Larger beta indicates higher building density so that the MMW signal is more likely to be blocked. Following [20], we assume that the blockage effects for different links are independent since the error of ignoring the correlation of blockage effects between links is marginal. The path loss exponent of a link, which is denoted by α, is modeled as a discrete random variable, where it takes on values $\alpha = \alpha_L$ with probability $p_L(\mathbf{x},\mathbf{y})$ for LoS, and $\alpha = \alpha_N$ with probability $p_N(\mathbf{x},\mathbf{y})$ for non-LoS, respectively.

We assume that each user is equipped with an omnidirectional antenna[1] with antenna gain M_u. All BSs are assumed to have steerable antennas. We use a sectored antenna model as in [61, 50, 21] to model the actual antenna pattern. The sectored antenna model is characterized by three parameters, i.e., main lobe gain M_b, back lobe gain m_b, and main lobe beamwidth ω_b. The BS antenna gain as a function of the steering angle θ_b is given by

$$G(\theta) = \begin{cases} M_b & |\theta_b| \leq \omega_b \\ m_b & \text{elsewhere.} \end{cases}$$

We assume a perfect beam aligment between the user and its serving BS, where the total directivity gain of the desired link is $M_b M_u$. The beams for all

[1]Directional antennas can also be used at the user terminals. The derived formula can be easily extended for the case when the users have directional antennas. A similar treatment has been adopted in [21, 81, 84].

the interfering BSs are assumed to be randomly oriented with respect to each other. Thus, the steering angle of all interfering BSs is modeled as a uniform random variable over $(0, 2\pi]$. Correspondingly, the total directivity gain from a BS at $\mathbf{x}$ to a user at $\mathbf{y}$, denoted by $D_{\mathbf{x},\mathbf{y}}$, can be modeled as a discrete random variable, where it takes on values $a_1 = M_b M_u$ with probability $b_1 = \frac{\omega_b}{2\pi}$, and $a_2 = m_b M_u$ with probability $b_2 = 1 - \frac{\omega_b}{2\pi}$.

Each user is assumed to be associated with the BS that has the smallest path loss among all BSs in the cooperating cluster. We also assume that the serving BS is located in the same cluster at which the user is located. Note that there is a possibility that the serving BS lies outside the cluster at which the user is located. However, such an event occurs with negligible probability, especially when the density of the BSs is high [83]. For the intercell interference coordination, we consider a cluster-based intercell scheduling, in which BSs in a cluster cooperatively schedule their transmissions and choose a user to be served based on the scheduling scheme. To provide fairness among all the users in the cluster, we assume that the user takes a turn to be served in a round-robin manner.

Table 4.1 contains the summary of notations used in this chapter.

4.2.2 SINR

Based on the stationarity of the PPP, we consider the average performance of a reference user (termed the typical user) located at the origin $\mathbf{0}$ inside a reference cluster (termed the typical cluster), which is denoted by $\mathcal{C}_0$, as shown in Fig. 4.1. Such an average performance is equivalent to the average user performance in the system [63]. Correspondingly, the location of the typical cluster center, which is denoted by $\mathbf{C}$, follows a uniform distribution over $[-\frac{W}{2}, \frac{W}{2}]$. Denote by $\mathcal{C}_0(\mathbf{c})$ the square region of the typical cluster $\mathcal{C}_0$ centered at $\mathbf{C} = \mathbf{c}$ with sides W. Note that we define $\mathbf{C} \triangleq (C_x, C_y)$ and $\mathbf{c} \triangleq (c_x, c_y)$ throughout this chapter. The typical

user is served by the BS in the typical cluster that has the smallest path loss and located at $\mathbf{x}_0$. Thus, the SINR received by the typical user can be written as

$$\text{SINR} = \frac{h_{\mathbf{x}_0,\mathbf{0}} M_b M_u L(\mathbf{x}_0)}{\frac{\sigma^2}{P_t} + \sum_{\mathbf{x}\in\Phi_b} h_{\mathbf{x},\mathbf{0}} D_{\mathbf{x},\mathbf{0}} L(\mathbf{x})}, \tag{4.1}$$

where, $h_{(\cdot)}$ is the small-scale fading term. Similar to those in [81], we assume independent Rayleigh fading for each link, where $h_{(\cdot)}$ is exponentially distributed with unit mean. $L(\mathbf{x}) = \delta|\mathbf{x}|^{-\alpha}$ is the propagation loss where α equals to α_L with probability $p_L(\mathbf{x})$ for LoS link, and α_N with probability $p_N(\mathbf{x})$ if the link is non-LoS. δ represents the near-field path loss[2], σ^2 is the noise power, and Φ_b denotes the subset of the point process Φ consisting of points in $\mathbb{R}^2 \setminus \mathcal{C}_0(\mathbf{c})$.

4.3 Stochastic Geometry Analysis

In this section, we analyze the coverage probability of the typical user and the ASE of the MMW cellular network.

4.3.1 SINR Coverage Probability

We define the SINR coverage probability as the probability that the instantaneous SINR of a user is greater than a threshold t, which can be written as

$$P_c(t) = \mathbb{P}\left(\text{SINR} > t\right). \tag{4.2}$$

In other words, expression (4.2) also implies the complementary cumulative distribution function (CCDF) of the SINR[21, 85, 84].

Conditioned on the typical user is located inside the typical cluster $\mathcal{C}_0(\mathbf{c})$ and this user is served by a BS that has the smallest path loss l, the coverage

[2]In the close-in path loss model[38, 3, 84], δ can be regarded as the path loss at distance of 1 meter, which is given by $\delta = 20\log_{10}\left(\frac{2\pi d}{\lambda_c}\right)$ with $d = 1$ meter and λ_c represents the wavelength of the carrier frequency.

probability of such a user can be computed as

$$\begin{aligned}
&\mathbb{P}\left(\frac{h_{\mathbf{x}_0,\mathbf{0}} M_b M_u \delta l^{-1}}{\sigma^2 + I} > t \middle| \mathbf{C} = \mathbf{c}, L = l\right) \\
&\overset{(a)}{=} \exp\left(\frac{t\sigma^2 l}{\delta M_b M_u}\right) \mathbb{E}\left[\exp\left(-\frac{tlI}{\delta M_b M_u}\right) \middle| \mathbf{C} = \mathbf{c}, L = l\right] \\
&= \exp\left(\frac{t\sigma^2 l}{\delta M_b M_u}\right) \mathcal{L}_{I|\mathbf{C}=\mathbf{c},L=l}\left(\frac{tl}{\delta M_b M_u}\right),
\end{aligned} \tag{4.3}$$

where $I = \sum_{\mathbf{x}\in\Phi_b} h_{\mathbf{x},\mathbf{0}} D_{\mathbf{x},\mathbf{0}} L(\mathbf{x})$, (a) is based on the assumption that $h_{\mathbf{x}_0,\mathbf{0}}$ is an exponential random variable with unit mean and $\mathcal{L}_{I|\mathbf{C}=\mathbf{c},L=l}(s)$ is the Laplace transform of the random variable I evaluated at $s = \frac{tl}{\delta M_b M_u}$, conditioned on the typical user is located inside the typical cluster $\mathcal{C}_0(\mathbf{c})$ and this user is served by a BS that has the smallest path loss l.

To evaluate the conditional coverage probability in (4.3), we first compute the conditional Laplace transform of I. In practice, the interfering signal is mainly contributed by nearby BSs and the received power through those at far distance from the typical user is marginal after much severer propagation loss. To maintain the analytical tractability and result accuracy, we separate the overall interference into two terms, i.e., the interference from adjacent clusters (denoted by I_i for $i = 1, 2, \cdots, 8$) and the interference from BSs located outside the adjacent clusters (denoted by I_{out}). Thus, the conditional Laplace transform in (4.3) can be written as

$$\mathcal{L}_{I|\mathbf{C}=\mathbf{c},L=l}(s) = \prod_{i=1}^{8} \mathbb{E}\left[\exp(-sI_i)|\mathbf{C} = \mathbf{c}, L = l\right] \mathbb{E}\left[\exp(-sI_{\text{out}})|\mathbf{C} = \mathbf{c}, L = l\right], \tag{4.4}$$

where each expectation is derived individually as follows.

When the cluster-based intercell scheduling is applied in the considered system, it follows that only one BS in each cluster can be activated at a time. We approximate the location of the active BSs in the eight adjacent clusters of the typi-

cal cluster, denoted by $\mathcal{C}_i$ with $i = \{1, 2, \cdots, 8\}$ in Fig. 4.1, as independently and uniformly distributed over a square of sides W. Denote by $\mathcal{C}_1(\mathbf{c}), \mathcal{C}_2(\mathbf{c}), \cdots, \mathcal{C}_8(\mathbf{c})$ the regions corresponding to the eight adjacent clusters of the typical cluster. Then, to facilitate the derivation of $\mathbb{E}\left[\exp(-sI_1)|\mathbf{C} = \mathbf{c}, L = l\right]$, we denote $\mathbf{X}_1$ as the location of the interfering BS from cluster $\mathcal{C}_1(\mathbf{c})$. We define $\mathbf{X}_1 \triangleq (X_1, Y_1)$ and $\mathbf{x}_1 \triangleq (x_1, y_1)$. Given that the interfering BS from cluster $\mathcal{C}_1(\mathbf{c})$ is located at $\mathbf{X}_1 = \mathbf{x}_1$, the conditional Laplace transform of I_1 can be computed as

$$\begin{aligned}
&\mathbb{E}\left[\exp(-sI_1)|\mathbf{C} = \mathbf{c}, L = l, \mathbf{X}_1 = \mathbf{x}_1\right] \\
&\overset{(a)}{=} \mathbb{E}[\exp(-sh_{\mathbf{x}_1,\mathbf{0}} D_{\mathbf{x}_1,\mathbf{0}} \delta |\mathbf{x}_1|^{-\alpha_L})] \exp\left(-\beta|\mathbf{x}_1|\right) \\
&\quad + \mathbb{E}[\exp(-sh_{\mathbf{x}_1,\mathbf{0}} D_{\mathbf{x}_1,\mathbf{0}} \delta |\mathbf{x}_1|^{-\alpha_N})] \left(1 - \exp\left(-\beta|\mathbf{x}_1|\right)\right) \\
&\overset{(b)}{=} \sum_{k=1}^{2} b_k \frac{\exp\left(-\beta|\mathbf{x}_1|\right)}{1 + sa_k\delta|\mathbf{x}_1|^{-\alpha_L}} + \sum_{k=1}^{2} b_k \frac{\left(1 - \exp\left(-\beta|\mathbf{x}_1|\right)\right)}{1 + sa_k\delta|\mathbf{x}_1|^{-\alpha_N}},
\end{aligned} \tag{4.5}$$

where (a) follows from the fact that $\alpha = \alpha_L$ and $\alpha = \alpha_N$ with probability $p_L(\mathbf{x}_1)$ and $p_N(\mathbf{x}_1)$, respectively. (b) uses the moment generating function of the exponential random variable $h_{\mathbf{x}_1,\mathbf{0}}$ and the assumption that $D_{\mathbf{x}_1,\mathbf{0}}$ is a discrete random variable where $a_1 = M_b M_u$ and $a_2 = m_b M_u$ with probability $b_1 = \frac{\theta}{2\pi}$ and $b_2 = 1 - \frac{\theta}{2\pi}$, respectively. Then, through unconditioning on $\mathbf{X}_1$, we have

$$\begin{aligned}
&\mathbb{E}\left[\exp(-sI_1)|\mathbf{C} = \mathbf{c}, L = l\right] = \\
&\sum_{k=1}^{2} \int_{c_y - \frac{3W}{2}}^{c_y - \frac{W}{2}} \int_{c_x - \frac{3W}{2}}^{c_x - \frac{W}{2}} \frac{b_k \exp\left(-\beta\sqrt{x_1^2 + y_1^2}\right)}{1 + sa_k\delta\sqrt{x_1^2 + y_1^2}^{-\alpha_L}} f_{X_1,Y_1}(x_1, y_1) dx_1 dy_1 \\
&+ \sum_{k=1}^{2} \int_{c_y - \frac{3W}{2}}^{c_y - \frac{W}{2}} \int_{c_x - \frac{3W}{2}}^{c_x - \frac{W}{2}} \frac{b_k \left(1 - \exp\left(-\beta\sqrt{x_1^2 + y_1^2}\right)\right)}{1 + sa_k\delta\sqrt{x_1^2 + y_1^2}^{-\alpha_N}} f_{X_1,Y_1}(x_1, y_1) dx_1 dy_1,
\end{aligned} \tag{4.6}$$

where $f_{X_1,Y_1}(x_1, y_1)$ is the joint probability density function (PDF) of X_1 and Y_1.

Since X_1 and Y_1 are uniformly distributed within a square of sides W, we have

$$f_{X_1,Y_1}(x_1,y_1) = \begin{cases} \frac{1}{W^2} & c_x - \frac{3W}{2} < x_1 < c_x - \frac{W}{2}, \\ & c_y - \frac{3W}{2} < y_1 < c_y - \frac{W}{2} \\ 0 & \text{elsewhere.} \end{cases} \tag{4.7}$$

By substituting (4.7) into (4.6), we attain an analytical expression for the conditional Laplace transform of I_1.

We can follow the similar procedures as in (4.5)-(4.6) to obtain the Laplace transform of other I_i for $i = 2, 3, \cdots, 8$, and replace the joint PDF in (4.7) for each interference term. Let $\mathbf{X}_i \triangleq (X_i, Y_i)$, for $i = 2, 3, \cdots, 8$. The joint PDFs for each $\mathbf{X}_i$ are given by

$$f_{X_2,Y_2}(x_2,y_2) = \begin{cases} \frac{1}{W^2} & c_x - \frac{W}{2} < x_2 < c_x + \frac{W}{2}, \\ & c_y - \frac{3W}{2} < y_2 < c_y - \frac{W}{2} \\ 0 & \text{elsewhere,} \end{cases}$$

$$f_{X_3,Y_3}(x_3,y_3) = \begin{cases} \frac{1}{W^2} & c_x + \frac{W}{2} < x_3 < c_x + \frac{3W}{2}, \\ & c_y - \frac{3W}{2} < y_3 < c_y - \frac{W}{2} \\ 0 & \text{elsewhere,} \end{cases}$$

$$f_{X_4,Y_4}(x_4,y_4) = \begin{cases} \frac{1}{W^2} & c_x - \frac{3W}{2} < x_4 < c_x - \frac{W}{2}, \\ & c_y - \frac{W}{2} < y_4 < c_y + \frac{W}{2} \\ 0 & \text{elsewhere,} \end{cases}$$

$$f_{X_5,Y_5}(x_5,y_5)=\begin{cases}\frac{1}{W^2} & c_x+\frac{W}{2}<x_5<c_x+\frac{3W}{2},\\ & c_y-\frac{W}{2}<y_5<c_y+\frac{W}{2}\\ 0 & \text{elsewhere,}\end{cases}$$

$$f_{X_6,Y_6}(x_6,y_6)=\begin{cases}\frac{1}{W^2} & c_x-\frac{3W}{2}<x_6<c_x-\frac{W}{2},\\ & c_y+\frac{W}{2}<y_6<c_y+\frac{3W}{2}\\ 0 & \text{elsewhere,}\end{cases}$$

$$f_{X_7,Y_7}(x_7,y_7)=\begin{cases}\frac{1}{W^2} & c_x-\frac{W}{2}<x_7<c_x+\frac{W}{2},\\ & c_y+\frac{W}{2}<y_7<c_y+\frac{3W}{2}\\ 0 & \text{elsewhere,}\end{cases}$$

$$f_{X_8,Y_8}(x_8,y_8)=\begin{cases}\frac{1}{W^2} & c_x+\frac{W}{2}<x_8<c_x+\frac{3W}{2},\\ & c_y+\frac{W}{2}<y_8<c_y+\frac{3W}{2}\\ 0 & \text{elsewhere.}\end{cases}$$

Now, we derive the Laplace transform of I_{out}. The set of active BSs outside the adjacent clusters is approximated by a PPP Φ_a with intensity $\lambda_a=\frac{1}{W^2}$. To facilitate the derivation, we define

$$\mathcal{C}_T(\mathbf{c})\triangleq\left\{\begin{array}{ll}(x,y)\in\mathbb{R}^2 & :\left(c_x-\frac{3W}{2}\right)\le x\le\left(c_x+\frac{3W}{2}\right),\\ & \left(c_y-\frac{3W}{2}\right)\le y\le\left(c_y+\frac{3W}{2}\right)\end{array}\right\},$$

which is the union of $\mathcal{C}_0(\mathbf{c}),\mathcal{C}_1(\mathbf{c}),\cdots,\mathcal{C}_8(\mathbf{c})$. The Laplace transform of I_{out} is

given by

$$\mathbb{E}\left[\exp(-sI_{\text{out}})|\mathbf{C}=\mathbf{c}, L=l\right] \overset{(a)}{=} \exp\left(-\lambda_a \sum_{k=1}^{2} \int_{\mathbb{R}^2\setminus\mathcal{C}_T(\mathbf{c})} \frac{b_k \exp(-\beta|\mathbf{x}|)}{1+sa_k\delta|\mathbf{x}|^{-a_L}} d\mathbf{x}\right) \times \exp\left(-\lambda_a \sum_{k=1}^{2} \int_{\mathbb{R}^2\setminus\mathcal{C}_T(\mathbf{c})} \frac{b_k(1-\exp(-\beta|\mathbf{x}|))}{1+sa_k\delta|\mathbf{x}|^{-a_N}} d\mathbf{x}\right), \tag{4.8}$$

where (a) follows the definition of the probability generating functional (PGFL) of PPP [63] and follows the same steps as (4.5).

Finally, from (4.3), we can obtain the unconditional coverage probability as

$$P_c(t) = \int_0^\infty \int_{-\frac{W}{2}}^{\frac{W}{2}} \int_{-\frac{W}{2}}^{\frac{W}{2}} \exp\left(-\frac{tl\sigma^2}{\delta M_b M_u}\right) \times \mathcal{L}_{I|\mathbf{C}=\mathbf{c},L=l}\left(\frac{tl}{\delta M_b M_u}\right) f_{C_x,C_y}(c_x,c_y) f_L(l) dl dc_x dc_y, \tag{4.9}$$

where $f_{C_x,C_y}(c_x,c_y)$ is the joint PDF of C_x and C_y, which is given by

$$f_{C_x,C_y}(c_x,c_y) = \begin{cases} \frac{1}{W^2} & -\frac{W}{2} < c_x, c_y < \frac{W}{2} \\ 0 & \text{elsewhere.} \end{cases} \tag{4.10}$$

$f_L(l)$ is the PDF of L, which is given by [86]

$$f_L(l) = \Lambda'(l)\exp(-\Lambda(l)) \tag{4.11}$$

with

$$\Lambda'(l) = \frac{2\pi\lambda}{\alpha_L} l^{\frac{2}{\alpha_L}-1} e^{-\beta l^{1/\alpha_L}} + \frac{2\pi\lambda}{\alpha_N} l^{\frac{2}{\alpha_N}-1}\left(1-e^{-\beta l^{1/\alpha_N}}\right),$$

and

$$\Lambda(l) = \frac{2\pi\lambda}{\beta^2}\left(1-e^{-\beta l^{1/\alpha_L}}\left(1+\beta l^{1/\alpha_L}\right)\right) + \pi\lambda l^{2/\alpha_N} - \frac{2\pi\lambda}{\beta^2}\left(1-e^{-\beta l^{1/\alpha_N}}\left(1+\beta l^{1/\alpha_N}\right)\right).$$

4.3.2 Area Spectral Efficiency

Another performance metric of interest is the area spectral efficiency (ASE), which is defined as the maximum data rate per unit area normalized by the bandwidth. The ASE in bps/Hz/km^2 is given by [85]

$$ASE = \lambda \int_0^{T_{max}} \log_2(1+t) f_T(t) dt \tag{4.12}$$

where T_{max} is the maximum working SINR and $f_T(t)$ is the PDF of the SINR received by the typical user. Since $P_c(t)$ is equal to the CCDF of the SINR, the cumulative distribution function (CDF) of the SINR can be written as

$$F_T(t) = 1 - P_c(t). \tag{4.13}$$

Then, the PDF of T can be expressed as the derivative of its CDF, which is written as

$$f_T(t) = \frac{\partial F_T(t)}{\partial t}. \tag{4.14}$$

By substituting (4.14) into (4.12), we can obtain the analytical expression for the ASE.

4.4 Numerical Results

In this section, we provide numerical simulations to validate our analytical results. We also demonstrate the effect of BS coordination on the coverage probability $P_c(t)$ and ASE. We consider an MMW cellular network operating at a frequency $f = 73$ GHz with bandwidth of 100 MHz allocated to each user. In order to study the effectiveness of the proposed interference mitigation, we consider the BS intensity $\lambda = 400/km^2$, which represents an interference-limited MMW cellular

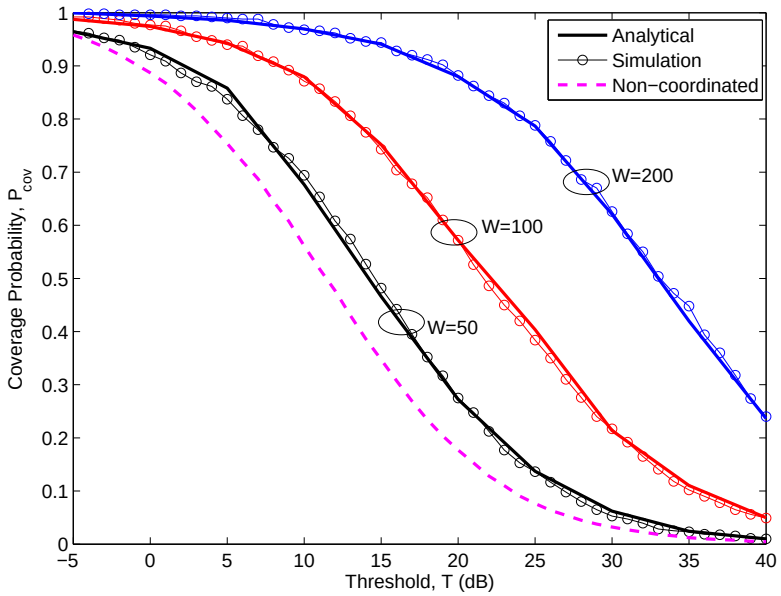

Figure 4.2. Comparison between the analytical and simulated coverage probability for $W = 50, 100, 200$.

network [87]. Besides, we set the intensity of user $\lambda_u = 1000/km^2$ to ensure that all BSs have at least one user to serve. The path LoS and non-LoS path loss exponents are set to $\alpha_L = 2.5$ and $\alpha_N = 4$, respectively. The parameters for the sectored antenna model at the BSs are set to M_b =18 dBi, m_b =-2 dBi, ω_b =10^o [88]. The noise power is given by σ^2(dBm)= -174 dBm/Hz+$10\log_{10}(BW) + 10$ dB.

With the given system parameters, the system coverage probability can be analytically obtained by using (4.9). Besides, we also provide the simulation results that are obtained from Monte Carlo simulations with 2000 random channel realizations in the following ways. We consider a square area of 3000x3000 m^2. In each channel realization, we first randomly generate BSs according to a PPP with intensity λ. Then, the entire area is divided into non-overlapping squares with sides W. Users are randomly generated following another PPP with intensity λ_u. In each cluster, an active user is randomly chosen and this user is served by a BS that provide the strongest received power.

Fig. 4.2 compares the analytical and simulated coverage probabilities of the typical user for various value of W. Here, we assume that the blockage factor

$\beta = 0.005$ to represent a dense building environment. In this figure, three values of W are considered, i.e., $W = 50$, $W = 100$ and $W = 200$. In addition, we also plot the coverage probability for the non-coordinated case, where all the BSs in the network are assumed to transmit at the same time. From this figure, we can make the following observations.

- The analytical expression derived in (4.9) is numerically accurate in all scenarios, which validates our theoretical analysis for the coverage probability.
- The coverage probability increases with the size of the clusters. For example, for the same threshold $T = 15$ dB, the coverage probability for the cluster size $W = 50$ is 0.48, while for $W = 200$ is 0.94. Intuitively, the number of coordinating BS increases with the cluster size. With a larger cluster size, the distance from the typical user to the interfering BS increases and thus the interfering signal can be reduced.
- The coverage probability of the proposed model is higher than that of the non-coordinated case. This can be explained by the fact that, as the number of transmitting BSs increases, the interfering signals enlarge, which potentially deteriorates the received signal at the typical user. By using the cluster-based intercell scheduling, the number of simultaneously active BSs in the network can be reduced, which consequently decreases the overall interfering signals.

Next, in Fig. 4.3, we plot the analytical ASE, which is obtained by (4.12). We use the same system setting as in Fig. 4.2 and $T_{max} = 20$ dB. Three values of building parameter β are considered, i.e., $\beta = 0.005, 0.001, 0.0005$, which represent dense, medium and sparse building environment, respectively. From this figure, we can make the following observations.

- All ASE curves exhibit a unimodal property in the range $W \in [20, 200]$. More specifically, these curves first increase monotonically as W increases.

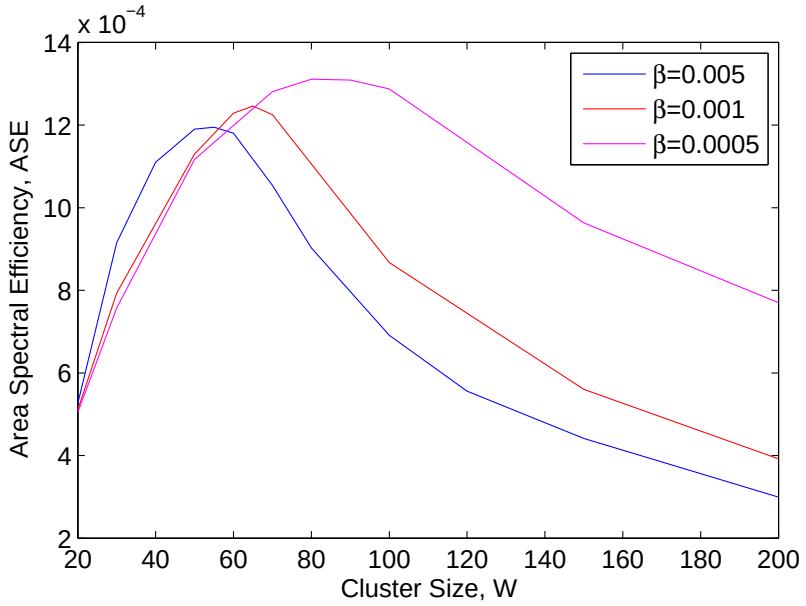

Figure 4.3. ASE of MMW cellular networks as a function of cluster size W.

After achieving their maximum points, these curves decrease with the further increasing value of W. By allowing the formation of larger clusters, the number of simultaneously active BSs reduces. On one hand, more interference signals can be removed and thus the coverage probability can be improved. On the other hand, such a large cluster will significantly decrease the ASE of the system.

- There exits a peak point for each ASE curve, which indicates that for a given network setup, there is an optimum W that leads to the maximum ASE. The value of the optimal W increases as the blockage factor β decreases. The intuitive reason is that in the sparse blockage environment, the non-LoS interference paths are converted to LoS interference paths and so the interfering signals at the receiver becomes stronger. As the size of the cooperating cluster increases, the distance between the user and the interfering BSs also increases, which consequently reduces the interfering signal. Thus, the sufficiently large size of cooperating cluster leads to the higher ASE.

4.5 Chapter Summary

In this chapter, we proposed an inter-cell interference coordination strategy for the dense MMW cellular networks. We modeled the locations of BS and user following independent and homogeneous PPPs. By using the concepts from stochastic geometry and incorporating the distinguishing features of MMW communications, we derived numerically tractable expressions for the coverage probability and ASE for the downlink MMW cellular networks. The results showed that the proposed BS coordination strategy outperformed the non-coordinated case in terms of coverage probability. Also, the results demonstrated that there exists an optimum cluster size that leads to the maximum ASE depending on the value of the blockage parameter.

Chapter 5

Uplink Performance Analysis for Millimeter Wave Cellular Networks with Clustered Users

This chapter investigates the uplink performance of the MMW cellular networks with clustered users. By modeling the locations of users as of a PCP, we derive tractable expressions to evaluate the SINR coverage probability for two user association strategies. First, the closest selection (CS), where the nearest LoS BS serves the user. Second, the strongest-selection (SS), where the user communicates with the BS that provides the strongest received signal among all BSs. Numerical results are provided to validate the accuracy of the analytical model under various system parameters. The results show that regarding SINR coverage probability, the SS strategy outperforms the CS strategy in the environment with dense blockages. The results also demonstrate that moderate FPC factors should be used at the low SINR thresholds, while full FPC is optimal for the high SINR thresholds.

5.1 Chapter Introduction

Recently, PCPs are actively studied for modeling and analyzing heterogeneous networks [66, 67, 89, 90, 91] and the device-to-device (D2D) [92] in microwave-based communications. Specifically, the works in[66, 89] used the point process formalism, which consists of multiple integrations leading to a complex analytical model and would increase the numerical computation time. An alternative way for any PCP based analysis is to incorporate the distance statistics as in [92, 67, 90, 91]. However, as a result of the blockage effect and the unique propagation characteristics, the results obtained for microwave networks are not applicable to MMW networks. So far, there are limited discussions regarding the PCP for MMW based communication except those in [93, 94]. While downlink performance of ad hoc networks has been investigated in [93] using the Matern cluster process (MCP) [65, Def. 3.6], the work in [94] presents the analysis for evaluating the uplink performance of clustered D2D using Thomas cluster process (TCP) [65, Def. 3.5]. However, the works in [93, 94] do not consider the power control at the user equipment (UE), which is a critical system design feature in the uplink transmission.

In this chapter, we analyze the performance of the uplink MMW cellular networks in the clustered users scenario by incorporating the peculiarity characteristics of MMW communications, power control, and user association strategies.

5.2 System Model

In this section, we introduce our system model for evaluating the performance of uplink MMW cellular networks. We begin with the spatial distribution of the transmitters and receivers. Then, we describe the channel model, the antenna model, the user association strategies, and the FPC. Table 5.1 contains the summary of notations used in this chapter.

Table 5.1. Notation Summary

Notation	Description
Φ_b,λ_b	Point process and intensity of BSs
Φ_u,λ_u	Point process and intensity of UEs before association
Φ'_u,λ'_u	Point process and intensity of UEs after association
Φ_p,λ_p	Parent process of cluster centers and intensity of clusters
Φ_p^L, Φ_p^N	Parent process of LoS and non-LoS clusters
$\kappa^{\mathbf{y}}$,λ_d	Daughter process of a cluster centered at $\mathbf{y}$ and intensity of UEs in the cluster
κ^0	The typical cluster centered at the origin
n	The average number of simultaneously active UEs in a cluster
D_c	Radius of cluster
a_L,a_N	LoS and non-LoS path loss exponents
c	link status with $c \in (L, N)$ for LoS and non-LoS
β	Blockage factor
δ	Path loss intercept
BW	MMW bandwidth
σ^2	Noise power
M_b, m_b, ω_b	Main lobe gain, back lobe gain and main lobe beamwidth of the BS
M_u, m_u, ω_u	Main lobe gain, back lobe gain and main lobe beamwidth of the UE
$G_b(\theta_b)$, $G_u(\theta_u)$	Antenna gain as a function of steering angle of the BS and the UE, respectively
$G_{\mathbf{x},\mathbf{z}}$	The total directivity gain between $\mathbf{x}$ and $\mathbf{z}$
a_k, b_k	PMF parameter of the random variable $G_{\mathbf{x},\mathbf{z}}$, b_k is the probability that $G_{\mathbf{x},\mathbf{z}} = a_k$ for $k \in \{1, 2, 3, 4\}$
R_s	Distance of the typical BS and its serving UE
R_x^a	Distance of the typical BS and the intra-cluster interfering UE located at $\mathbf{x}$
R_x^e	Distance of the typical BS and the inter-cluster interfering UE located at $\mathbf{x}$
R_y	Distance of the typical BS and the cluster center located at $\mathbf{y}$
R_t	Distance of an interfering UE to its serving BS

5.2.1 Spatial Cellular Network Model

We consider the uplink of an outdoor MMW cellular network and focus on the performance of outdoor users served by outdoor BSs, as depicted in Fig. 5.1. The outdoor BSs are randomly distributed in a two-dimensional Euclidean space $\mathbb{R}^2$

according to a homogeneous PPP Φ_b with intensity λ_b. The locations of UEs are modeled following the PCP Φ_u with intensity λ_u. We consider a special case of the Neyman-Scott PCP, i.e., MCP [65, Def. 3.6], where the parent points (cluster centers) are modeled by an independent PPP Φ_p with intensity λ_p. The locations of UEs for each cluster center are represented by a finite point process $\kappa^{\mathbf{y}}$ following a uniform distribution in a circle-shaped cluster $\mathcal{B}(\mathbf{y}, D_c)$ with radius D_c and centered at $\mathbf{y} \in \Phi_p$. The PDF of UEs in the cluster is given by

$$f(\mathbf{x}, \mathbf{y}) = \begin{cases} \frac{1}{\pi R_c^2}, & d = |\mathbf{x} - \mathbf{y}| \leq R_c, \\ 0, & \text{elsewhere}, \end{cases} \tag{5.1}$$

where d is the distance of any arbitrary UE located at $\mathbf{x}$ relative to its cluster center located at $\mathbf{y}$. Specifically, the complete PCP, Φ_u, is given by

$$\Phi_u = \bigcup_{\mathbf{y} \in \Phi_p} \kappa^{\mathbf{y}}, \tag{5.2}$$

where $\kappa^{\mathbf{y}} \in \mathcal{B}(\mathbf{y}, D_c)$ denotes the UEs point process with intensity λ_d.

We assume that each BS serves a single user per channel, where each user takes a turn to be served in a round-robin manner [95, 96, 89, 94]. Therefore, we model the location of active UEs by thinning theorem as in [89, 94], where the location of all active UEs is modeled by PCP Φ'_u with intensity $\lambda'_u = \lambda_b$. Since λ'_u can also be represented as $\lambda'_u = \lambda_p \lambda_d \pi D_c^2$, we have the average number of simultaneously active UEs in the cluster as $n = \lambda_d \pi Dc^2 = \frac{\lambda_b}{\lambda_p}$, where λ_d is the intensity of active UEs in a cluster.

The communications between UEs and their associated BSs are surrounded by randomly distributed buildings in the communication area. Due to the severe penetration loss encountered by the MMW signals when passing through these buildings, a UE can be either LoS or non-LoS to its associated BS. We adopt the blockage model in [50] to characterize the blockage effects on the system

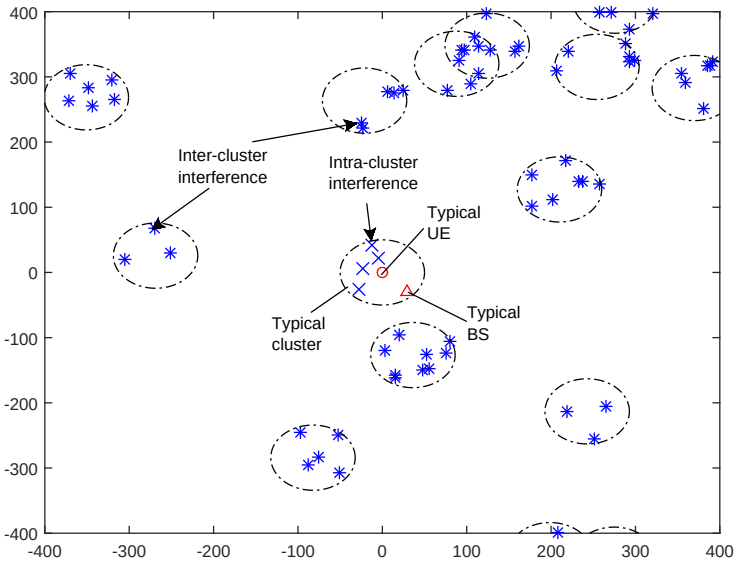

Figure 5.1. Examples of user distribution based on PCP with $\lambda_p = 20/km^2$ and $n = 5$

performance. By incorporating such a model, the probability of LoS and non-LoS links, are respectively given by, $p_L(r) = e^{-\beta r}$ and $p_N(r) = 1 - e^{-\beta r}$, where r represents the distance between a UE and BS, and β is the blockage factor, which is determined by the density and the average size of the buildings.

For simplicity, we assume that all users in the finite point process cluster $\kappa^{\mathbf{y}}$ have the same link status, denoted by $c \in \{L, N\}$[1], where L is for LoS and N for non-LoS. Consequently, from the perspective of the BS, the center of clusters can be divided into two sub-processes: Φ_p^L with intensity $\lambda_p p_L(r)$ and Φ_p^N with intensity $\lambda_p p_N(r)$ for LoS clusters and non-LoS clusters, respectively. Also, full frequency reuse is assumed in the uplink transmission and all BSs have the same available bandwidth BW, which is equally allocated across all users.

[1]In practice, users in the same cluster may appear as LoS or non-LoS status to the BS. However, our simulation results show that assuming the same link status for all user in the same cluster causes a minor error. The similar assumption is also made in [93].

5.2.2 Antenna Model

All the MMW BSs and UEs are assumed to have directional antennas. We use a sectored antenna model as in [50] to model the actual antenna pattern. The BS antenna gain as a function of the steering angle θ_b, is given by

$$G_b(\theta_b) = \begin{cases} M_b, & |\theta_b| \leq \omega_b, \\ m_b, & \text{elsewhere}, \end{cases} \tag{5.3}$$

where M_b, m_b and ω_b are respectively, the main lobe gain, back lobe gain and main lobe beamwidth of the BS antenna. The UE antenna gain as a function of the steering angle θ_u is modeled in the similar manner such that

$$G_u(\theta_u) = \begin{cases} M_u, & |\theta_u| \leq \omega_u, \\ m_u, & \text{elsewhere}, \end{cases} \tag{5.4}$$

where M_u, m_u and ω_u are respectively, the main lobe gain, back lobe gain and main lobe beamwidth of the UE antenna.

We assume a perfect beam aligment between the UE and its serving BS, where the total directivity gain of the desired link is $M_b M_u$. Furthermore, for the interfering link, we model the steering angle of UEs and BSs as independently and uniformly distributed over $(0, 2\pi]$. For a given interfering UE located at $\mathbf{x}$ and a BS at $\mathbf{z}$, their total directivity gain is $G_{\mathbf{x},\mathbf{z}} = G_b(\theta_b)G_u(\theta_u)$. Correspondingly, the total directivity gain $G_{\mathbf{x},\mathbf{z}}$ can be modeled as a discrete random variable [50]

, which is given as

$$G_{\mathbf{x},\mathbf{z}} = \begin{cases} a_1 = M_b M_u, & \text{w.p. } b_1 = \frac{\omega_b \omega_u}{4\pi^2}, \\ a_2 = M_b m_u, & \text{w.p. } b_2 = \frac{\omega_b}{2\pi}\left(1 - \frac{\omega_u}{2\pi}\right), \\ a_3 = m_b M_u, & \text{w.p. } b_3 = \left(1 - \frac{\omega_b}{2\pi}\right)\frac{\omega_u}{2\pi}, \\ a_4 = m_b m_u, & \text{w.p. } b_4 = \left(1 - \frac{\omega_b}{2\pi}\right)\left(1 - \frac{\omega_u}{2\pi}\right), \end{cases} \tag{5.5}$$

where a_k is the probability distribution with probability (w.p.) b_k and $k \in \{1, 2, 3, 4\}$.

5.2.3 User Association Strategies

We consider two user association strategies as in the following:

- Closest-selection (CS) : In this case, we only consider the LoS clusters, where we assume that a user associates with the closest BS via LoS link and the selection of a serving BS is based on distance.
- Strongest-selection (SS) : In this case, we consider both the LoS and non-LoS clusters and assume that a user is served by the BS that provides the maximum long-term averaged received power, i.e., the effect of fading is ignored[2].

5.2.4 User Fractional Power Control

Fractional power control (FPC) is employed at the UE to overcome the effects of path loss and reshape the interference power [95]. In this work, we assume that each UE utilizes a distance-proportional FPC, where the transmit power is given

[2]In this work, we follow the convention of stochastic geometric analysis (e.g., [97, 86, 96]) where fading is ignored. As stated in [97] cell association based on long-term averaged power is used to avoid the ping-pong effect of handover due to the the fast fluctuation of the instantaneous channel gain.

by

$$P_T(\mathbf{x}, \mathbf{z}) = |\mathbf{x} - \mathbf{z}|^{\alpha\epsilon}, \tag{5.6}$$

where $|\mathbf{x} - \mathbf{z}|$ is the distance between a UE located at $\mathbf{x}$ and its serving BS located at $\mathbf{z}$. $\epsilon \in [0, 1]$ is the FPC factor. Therefore, when a UE moves closer to the serving BS, the transmit power required to maintain the feasible received SINR decreases. This power control is important for limited battery-operated devices such as mobile devices. The transmit power is static when $\epsilon = 0$ and FPC with full path loss compensation when $\epsilon = 1$.

5.2.5 Signal-to-interference and noise ratio (SINR)

Based on the stationarity of the BS, cluster center and UE point processes, we assume that a reference UE (termed the typical UE) is located at the origin in the reference cluster (termed the typical cluster) and served by a BS located at $\mathbf{z}$ (termed the typical BS). Without loss of generality, we consider the typical cluster centered at the origin, which is denoted by $\kappa^{\mathbf{0}}$, by conditioning on the event that the origin exits in Φ_p. Note that the distribution of Φ_u is unaffected by conditioning on the typical cluster or the typical UE based on Slivnyak's Theorem [65, Theorem 8.10]. Thus, based on the assumptions mentioned above, the SINR received by the typical BS at $\mathbf{z}$ can be written as

$$\mathrm{SINR}_{\mathbf{z}} = \frac{h_{\mathbf{z}} P_T(\mathbf{z}) M_b M_u L(\mathbf{z})}{\sigma^2 + \sum_{\mathbf{x} \in \Phi_u} h_{\mathbf{x},\mathbf{z}} P_T(\mathbf{x}, \mathbf{z}) G_{\mathbf{x},\mathbf{z}} L(\mathbf{x}, \mathbf{z})}, \tag{5.7}$$

where $h_{(.)}$ is the small-scale fading term. We assume that the small fading term is independently exponentially distributed with unit mean (i.e., Rayleigh fading). σ^2 is the noise power. $L(\mathbf{x}, \mathbf{z}) = \delta|\mathbf{x} - \mathbf{z}|^{-\alpha}$ is the path loss where α equals to α_L with probability $p_L(r)$ for LoS link, and α_N with probability $p_N(r)$ if the link is

non-LoS. δ represents the near-field path loss[3].

From (5.7), we define two types of interference as follows:

- Intra-cluster interference is the interference received by the typical BS from all interfering UEs located within the typical cluster except from the typical UE, which can be modeled as

$$I^a = \sum_{\mathbf{x}\in\kappa^{\mathbf{0}}} h_{\mathbf{x},\mathbf{z}} P_T(\mathbf{x},\mathbf{z}) G_{\mathbf{x},\mathbf{z}} L(\mathbf{x},\mathbf{z}). \tag{5.8}$$

- Inter-cluster interference is the interference received by the typical BS from all interfering UEs located outside the typical cluster, which can be modeled as

$$I^e = \sum_{\mathbf{y}\in\Phi_p} \sum_{\mathbf{x}\in\kappa^{\mathbf{y}}} h_{\mathbf{x},\mathbf{z}} P_T(\mathbf{x},\mathbf{z}) G_{\mathbf{x},\mathbf{z}} L(\mathbf{x},\mathbf{z}). \tag{5.9}$$

5.2.6 Mathematical Preliminaries

Denote by $G(v)$, $G_p(v)$ and $G_c(v)$ the generating functionals of Φ_c, $\kappa^{\mathbf{0}}$ and Φ_p processes, respectively. The generating functional is given by

$$\begin{aligned} G(v) &\overset{(a)}{=} G_p(G_{(\cdot)}(v)) \overset{(b)}{=} G_p(G_{(\mathbf{y})}(v)) \\ &\overset{(c)}{=} G_p(G_c(v(\mathbf{y}+\cdot))) \overset{(d)}{=} \mathbb{E}\left[\prod_{\mathbf{y}\in\Phi_p} G_c(v(\mathbf{y}+\cdot)\right] \\ &\overset{(e)}{=} \exp\left(-\int_{\mathbb{R}^2} \left(1 - G_c(v(\mathbf{y}+\cdot))\right) \Lambda(d\mathbf{y})\right) \\ &\overset{(f)}{=} \exp\left(-\lambda_p \sum_{c\in\{L,N\}} \int_{\mathbb{R}^2} \left(1 - G_c(v(\mathbf{y}+\cdot))\right) p_c(\mathbf{y}) d\mathbf{y}\right), \end{aligned} \tag{5.10}$$

where (a)-(d) are from [62], (e) is due to the generating functional of PPP and (f) is from the fact that Φ_L and Φ_N are independent. The generating function

[3]In the close-in path loss model[84], δ can be regarded as the path loss at distance of 1 meter, which is given by $\delta = 20\log_{10}\left(\frac{2\pi d}{f_c}\right)$ with $d = 1$ meter and f_c represents the wavelength of the carrier frequency.

of the representative cluster in (5.10) is given by

$$G_c(v(\mathbf{y}+\cdot)) = \mathbb{E}\left[\prod_{\mathbf{x}\in\kappa^0} v(\mathbf{y}+\mathbf{x})\right] = \exp\left(\frac{-n}{\pi D_c^2}\int_{\mathcal{B}(\mathbf{0},D_c)} v(\mathbf{y}+\mathbf{x})d\mathbf{x}\right). \tag{5.11}$$

where $\mathcal{B}(\mathbf{0}, D_c)$ represents a circle centered at the origin with radius D_c.

5.3 Stochastic Geometry Analysis

In this section, we first provide the distance distributions and then analyze the interference and SINR coverage probability.

5.3.1 Distance Distribution Analysis

The distribution of distance between nodes is of great importance for evaluating the performance metrics in the random network. In this subsection, we provide all the relevant distance distributions that will be used in the interference and SINR coverage analysis.

Let R_s be the distance from the typical BS to the typical UE. The following lemmas provide the distributions of R_s for the CS and SS strategies.

Lemma 5.1. *When the CS strategy is employed, the PDF of R_s is given by*

$$f_{R_s}^{CS}(r|L) = 2\pi\lambda_b r \exp\left(-\beta r\right) \exp\left(-\frac{2\pi\lambda_b}{\beta^2}\left(1-\frac{(1+\beta r)}{\exp\left(\beta r\right)}\right)\right). \tag{5.12}$$

Proof. The proof of **Lemma 5.1** is provided in Appendix B.1. □

Lemma 5.2. *Given that the typical UE is connected to a LoS BS. When the SS strategy is employed, the PDF of R_s is given by*

$$f_{R_s}^{SS}(r|L) = \frac{2\pi\lambda_b r \exp(-\beta r)}{\mathcal{A}_L} \exp\left(-\Lambda_L(r)\right), \tag{5.13}$$

where

$$\Lambda_L(r) = 2\pi\lambda_b \left(\frac{1+\beta r^{v_l}}{\exp(\beta r^{v_l})\beta^2} - \frac{(1+\beta r)}{\exp(\beta r)\beta^2} + \frac{r^{2v_l}}{2} \right), \tag{5.14}$$

$v_l = \frac{\alpha_L}{\alpha_N}$, *and* $\mathcal{A}_L$ *is the probability that the typical UE is associated with a LoS BS, which is given by*

$$\mathcal{A}_L = 2\pi\lambda_b \int_0^\infty r \exp(-\beta r) \exp\left(-\Lambda_L(r)\right) dr. \tag{5.15}$$

Proof. The proof of **Lemma 5.2** is similar to that in [86] and provided in Appendix B.2 for completeness. □

Lemma 5.3. *Given that the typical UE is connected to a non-LoS BS. When the SS strategy is employed, the PDF of* R_s *is given by*

$$f_{R_s}^{SS}(r|N) = \frac{2\pi\lambda_b r \left(1 - \exp(-\beta r)\right)}{\mathcal{A}_N} \exp\left(-\Lambda_N(r)\right), \tag{5.16}$$

where

$$\Lambda_N(r) = 2\pi\lambda_b \left(\frac{(1+\beta r)}{\exp(\beta r)\beta^2} - \frac{1+\beta r^{v_n}}{\exp(\beta r^{v_n})\beta^2} + \frac{r^2}{2} \right), \tag{5.17}$$

$v_n = \frac{\alpha_N}{\alpha_L}$ *and* $\mathcal{A}_N$ *is the probability that the typical UE is associated with a non-LoS BS, which is given by*

$$\mathcal{A}_N = 1 - \mathcal{A}_L. \tag{5.18}$$

Proof. The proof of **Lemma 5.3** follows a similar method as that of **Lemma 5.2** and is omitted here. □

Next, we denote R_t as the distance of an interfering UE to its serving BS. Recall that we have assumed a single active UE per BS in the uplink transmission.

Thus, the random variable R_t is identically distributed but not independent. However, it was found in [95, 96] that this dependence is weak. To maintain the analytical tractability, we assume that the random variable R_t is independent and identically distributed (i.i.d), where the PDF of R_t is given in the following lemma.

Lemma 5.4. *Given that the interfering UE has LoS or non-LoS status to its serving BS, the PDF of R_t for LoS and non-LoS can be approximated as*

$$f_{R_t}^{\xi}(r|L) \approx f_{R_s}^{\xi}(r|L), \tag{5.19}$$

and

$$f_{R_t}^{\xi}(r|N) \approx f_{R_s}^{\xi}(r|N), \tag{5.20}$$

where $\xi \in (CS, SS)$.

Proof. The proof of **Lemma 5.4** follows directly from **Lemma 5.2** and **Lemma 5.3**. □

Recall from (5.8) and (5.9) that we have two types of interference, i.e., intra-cluster interference and inter-cluster interference. Denote by R_x^a and R_x^i the distance from the typical BS to the intra-cluster interfering UE and the distance from the typical BS to the inter-cluster interfering UE, respectively. Also, there are two cases of receiver, i.e.,

- **Case 1**: when the typical BS is located inside the typical cluster, where $0 \leq R_s < D_c$, as shown in Fig. 5.2.
- **Case 2**: when the typical BS is located outside the typical cluster, $R_s \geq D_c$, as shown in Fig. 5.3.

The PDF of R_x^a for **Case 1** and **Case 2** can be derived as in the following lemma.

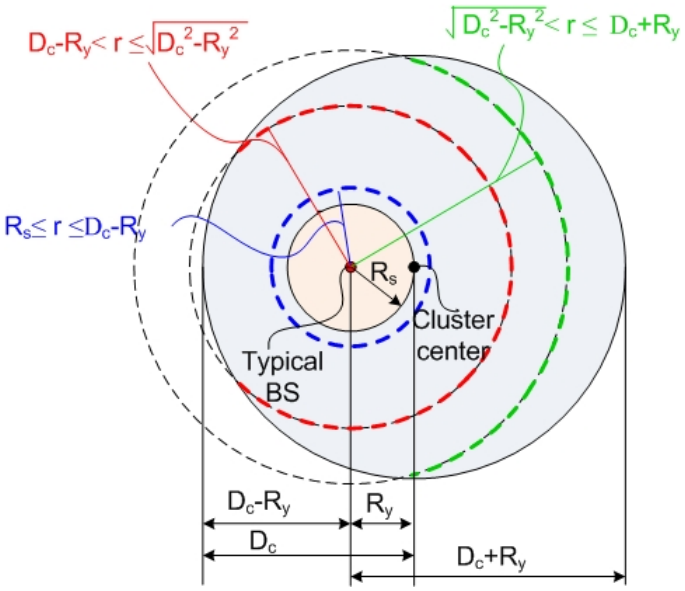

Figure 5.2. An example of interfering UE for **Case 1**.

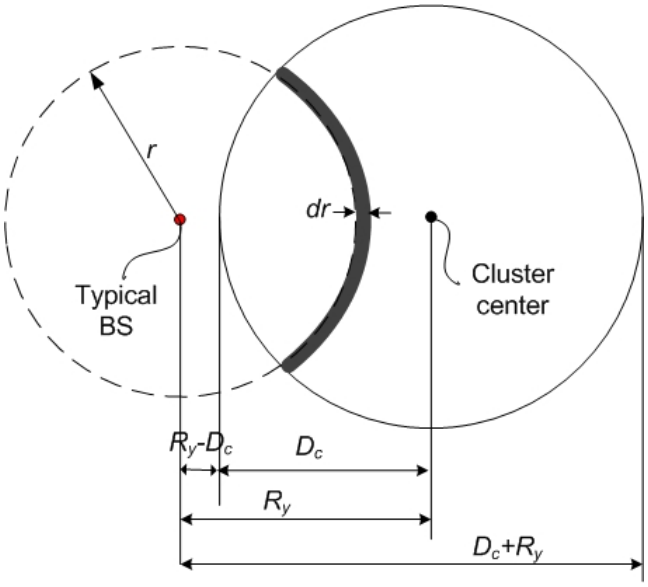

Figure 5.3. An example of interfering UE for **Case 2**.

Lemma 5.5. *Conditioned on R_s, the PDF of R_x^a is given by*

$$f_{R_x^a}(r|R_s) = \begin{cases} \frac{\mathcal{A}(r)}{\pi D_c^2}, & \text{if } 0 \leq Rs < D_c, \\ \frac{\mathcal{B}(r)}{\pi D_c^2}, & \text{if } Rs \geq D_c, \end{cases} \tag{5.21}$$

where

$$\mathcal{A}(r) = \begin{cases} 4r\left(\arccos\left(\frac{r}{2D_c}\right) - \frac{r}{2D_c}\sqrt{1-\left(\frac{r}{2D_c}\right)^2}\right), \\ \qquad\qquad\qquad\qquad \textit{if } R_s \le r \le R_s + D_c, \\ 0, \qquad\qquad\qquad\qquad \textit{otherwise}, \end{cases} \tag{5.22}$$

and

$$\mathcal{B}(r) = \begin{cases} 2r\arccos\left(\frac{R_s^2+r^2-D_c^2}{2R_s r}\right), & \textit{if } R_s \le r \le R_s + D_c, \\ 0, & \textit{otherwise}. \end{cases} \tag{5.23}$$

Proof. The proof is provided in Appendix B.3. □

Next, we derive the distribution of the distance from the typical BS to the inter-cluster interfering UE, which is denoted by R_x^e. We also denote R_y as the distance from the typical BS to the cluster center. The PDF of R_x^e can be derived as in the following lemma.

Lemma 5.6. *Conditioned on R_s, the PDF of R_x^e is given by*

$$f_{R_x^e}(r|R_s) = \begin{cases} \frac{\mathcal{C}(r)}{\pi D_c^2}, & \textit{if } 0 \le R_y < D_c, \\ \frac{\mathcal{D}(r)}{\pi D_c^2}, & \textit{if } R_y \ge D_c, \end{cases} \tag{5.24}$$

where

$$\mathcal{C}(r) = \begin{cases} 2\pi r, & R_s \le r \le D_c - R_y, \\ 2\pi r - y(r), & D_c - R_y < r \le \sqrt{D_c^2 - R_y^2}, \\ y(r), & \sqrt{D_c^2 - R_y^2} < r \le D_c + R_y, \\ 0, & \textit{otherwise}, \end{cases} \tag{5.25}$$

$$\mathcal{D}(r) = \begin{cases} y(r), & R_y - D_c \leq r \leq R_y + D_c, \\ 0, & otherwise, \end{cases} \tag{5.26}$$

such that,

$$y(r) = 2r \arccos\left(\frac{R_y^2 + r^2 - D_c^2}{2R_y r}\right). \tag{5.27}$$

Proof. The proof is provided in Appendix B.4. □

5.3.2 Interference Analysis

Based on (5.8) and (5.9), there are two types of interfering UEs, i.e., intra-cluster interfering UEs and inter-cluster interfering UEs. Let $i \in \{a, e\}$ represent the intra-cluster and inter-cluster UEs. Due to the presence of blockages, the interfering UEs can be further partitioned into four cases, which are (i) LoS UEs with LoS links to their serving BSs (denoted by I_{LL}^i), (ii) LoS UEs with non-LoS links to their serving BSs (denoted by I_{LN}^i), (iii) non-LoS UEs with LoS links to their serving BSs (denoted by I_{NL}^i) and (iv) non-LoS UEs with non-LoS links to their serving BSs (denoted by I_{NN}^i). Consequently, the overall intra-cluster and inter-cluster interference are respectively given by

$$I^a = I_{LL}^a + I_{LN}^a + I_{NL}^a + I_{NN}^a, \tag{5.28}$$

and

$$I^e = I_{LL}^e + I_{LN}^e + I_{NL}^e + I_{NN}^e, \tag{5.29}$$

where the Laplace transforms of each terms are given in the following theorem.

Theorem 5.1. *Conditioned on R_s, The Laplace transform of I^a is given by*

$$\mathcal{L}_{I^a}(s|R_s) = \prod_{\mathcal{C}} \exp\left(-n \sum_{k=1}^{4} b_k \int_{R_s}^{D_c+R_s} \mathcal{F}_{\mathcal{C}}(s,r) f_{R_x^a}(r|R_s) dr\right), \tag{5.30}$$

where $\mathcal{C} \in \{LL, LN, NL, NN\}$,

$$\mathcal{F}_{LL}(s,r) = \mathcal{A}_L \int_0^{\infty} \left(1 - \frac{1}{1 + \frac{s a_k \delta t^{\alpha_L \epsilon}}{r^{\alpha_L}}}\right) f_{R_t}^{\xi}(t|L) dt, \tag{5.31}$$

$$\mathcal{F}_{LN}(s,r) = \mathcal{A}_N \int_0^{\infty} \left(1 - \frac{1}{1 + \frac{s a_k \delta t^{\alpha_L \epsilon}}{r^{\alpha_N}}}\right) f_{R_t}^{\xi}(t|N) dt, \tag{5.32}$$

$$\mathcal{F}_{NL}(s,r) = \mathcal{A}_L \int_0^{\infty} \left(1 - \frac{1}{1 + \frac{s a_k \delta t^{\alpha_N \epsilon}}{r^{\alpha_L}}}\right) f_{R_t}^{\xi}(t|L) dt, \tag{5.33}$$

$$\mathcal{F}_{NN}(s,r) = \mathcal{A}_N \int_0^{\infty} \left(1 - \frac{1}{1 + \frac{s a_k \delta t^{\alpha_N \epsilon}}{r^{\alpha_N}}}\right) f_{R_t}^{\xi}(t|N) dt, \tag{5.34}$$

*a_k and b_k are antenna directivity parameters as defined in Section 5.2.2, $f_{R_t}^{\xi}(t|c)$ and $f_{R_x^a}(r|R_s)$ are given in **Lemma 5.4** and **Lemma 5.5**, respectively.*

Proof. The proof is provided in Appendix B.5. □

Theorem 5.2. *Conditioned on R_s, The Laplace transform of I^e is given by*

$$\mathcal{L}_{I^e}(s|R_s) = \prod_{\mathcal{C}} \exp\left(-2\pi\lambda_p \int_{R_s}^{\infty} (1 - \beta_{\mathcal{C}}(y,s)) y p_c(y) dy\right), \tag{5.35}$$

where

$$\beta_{\mathcal{C}}(y,s) = \exp\left(-n \sum_{k=1}^{4} b_k \int_{\mathcal{R}} \mathcal{F}_{\mathcal{C}}(s,r) f_{R_x^e}(r|R_s) dr\right), \tag{5.36}$$

such that $\mathcal{F}_{\mathcal{C}}(s,r)$ for $\mathcal{C} \in \{LL, LN, NL, NN\}$ are given in (5.31)-(5.34). $f_{R_x^e}(r|R_s)$

is given in ***Lemma 5.6****. Based on* ***Lemma 5.6****,* $\mathcal{R}$ *refers to the domain of the random variable* R_x^e *subject to different cases in (5.24).*

Proof. The proof is provided in Appendix B.6. □

It can be observed from **Theorem 5.1** and **Theorem 5.2** that the conditional Laplace transforms of the interference depend on the location of the typical BS $|\mathbf{z}| = R_s$. This indicates that the distribution of the interference depends on the location at which we observe it. Conversely, when the transmitter is modeled following the PPP as in [64, 95, 98, 99, 88, 96], the interference distribution is independent of the receiver location.

5.3.3 SINR coverage probability

We define the coverage probability as the probability that the instantaneous SINR received by a BS at $\mathbf{z}$ is greater than a threshold γ, which can be written as

$$\mathbb{P}_{cov}(\gamma) = \mathbb{P}\left(\mathrm{SINR}_{\mathbf{z}} > \gamma\right). \tag{5.37}$$

Now, based on the Laplace transforms derived in Section 5.3.2, we present the SINR coverage probability of the typical BS for the CS and SS strategies in the following theorems.

Theorem 5.3. *The SINR coverage probability in the uplink MMW cellular networks for the CS strategy can be expressed as*

$$\mathbb{P}_{cov}^{CS}(\gamma) = \int_0^\infty \exp\left(-s\sigma^2\right) \mathcal{L}_{I_{LL}^a}(s|v)\mathcal{L}_{I_{LL}^e}(s|v) f_{R_s}^{CS}(v|L)dv \tag{5.38}$$

where $s = \frac{\gamma v^{\alpha_L(1-\epsilon)}}{\delta M_b M_u}$, $\mathcal{L}_{I_{LL}^a}(s|v)$ *and* $\mathcal{L}_{I_{LL}^e}(s|v)$ *are given in (B.13) and (B.14), respectively, and* $f_{R_s}^{CS}(v|L)$ *is given in* ***Lemma 5.1****.*

Proof. The proof is provided in Appendix B.7. □

Theorem 5.4. *The SINR coverage probability in the uplink MMW cellular networks for the SS strategy can be expressed as*

$$\mathbb{P}_{cov}^{SS}(\gamma) = \mathcal{A}_L \mathbb{P}(\gamma|L) + \mathcal{A}_N \mathbb{P}(\gamma|N), \tag{5.39}$$

where $\mathbb{P}(\gamma|c)$ is the conditional coverage probability given the status of the communication link is $c \in \{L, N\}$, $\mathcal{A}_L$ and $\mathcal{A}_N$ are given in (5.15) and (5.18), respectively. Further, $\mathbb{P}(\gamma|c)$ can be evaluated as

$$\mathbb{P}(\gamma|L) = \int_0^\infty \exp\left(-s_L \sigma^2\right) \mathcal{L}_{I^a}(s_L|v) \mathcal{L}_{I^e}(s_L|v) f_{R_s}^{SS}(v|L) dv, \tag{5.40}$$

and

$$\mathbb{P}(\gamma|N) = \int_0^\infty \exp\left(-s_N \sigma^2\right) \mathcal{L}_{I^a}(s_N|v) \mathcal{L}_{I^e}(s_N|v) f_{R_s}^{SS}(v|N) dv, \tag{5.41}$$

*where $s_L = \frac{\gamma v^{\alpha_L(1-\epsilon)}}{\delta M_b M_u}$, $s_N = \frac{\gamma v^{\alpha_N(1-\epsilon)}}{\delta M_b M_u}$. For $s_c = \{s_L, s_N\}$, $\mathcal{L}_{I^a}(s_c|v)$ and $\mathcal{L}_{I^e}(s_c|v)$ are given in **Theorem 5.1** and **Theorem 5.2**, respectively. $f_{R_s}^{SS}(v|L)$ and $f_{R_s}^{SS}(v|N)$ are given in **Lemma 5.2** and **Lemma 5.3**, respectively .*

Proof. The proof follows the similar procedures for obtaining the coverage probability in **Theorem 5.3** and using the Laplace transforms in **Theorem 5.1** and **Theorem 5.2**. □

The expressions in **Theorem 5.3** and **Theorem 5.4** provide general results for the coverage probabilities with the CS and SS strategies, respectively. Essentially, we write the interference as the summation of two independent terms, i.e., intra-cluster and inter-cluster interference. In PCP, these two terms are independent. Thus, the Laplace transform of the sum of independent random variables can be written as the product of the individual Laplace transform as given in **Theorem 5.3** and **Theorem 5.4**.

We notice that every component of **Theorem 5.3** depends on (5.12). To

obtain some analytical insights into the network's performance, we focus on the analytical expression in (5.12). Specifically, (5.12) is a multiplication function between two terms, both of which consist of BS intensity parameter, λ_b. The first term is a linear function, i.e., $2\pi\lambda_b r$, and the remaining term comprises of a negative exponential function. As λ_b increases, the former term is dominant in initial state, which leads to the increase of the coverage probability in **Theorem 5.3**. By further increasing λ_b, the later term is more dominant and hence the overall function in (5.12) decays exponentially to zero. Thus, the coverage probability converges to zero. In Section 5.4, we will demonstrate the existence of an optimal BS intensity that maximizes the coverage probability for both CS and SS strategies.

The SINR coverage probability in **Theorem 5.3** can be simplified for the fixed power transmit case, i.e., $\epsilon = 0$ as in the following corollary.

Corollary 5.1. *The SINR coverage probability in the uplink of MMW cellular networks for the CS strategy with fixed user transmit power is given by*

$$\mathbb{P}_{cov}^{CS}(\gamma) = \int_0^\infty \exp\left(-s\sigma^2\right) \mathcal{L}_{I^a}(s|v)\mathcal{L}_{I^e}(s|v) f_{R_s}^{CS}(v|L)dv, \tag{5.42}$$

where

$$\mathcal{L}_{I^a}(s|v) = \exp\left(-n\sum_{k=1}^{4} b_k \int_v^{D_c+v} \left(1 - \frac{1}{1+\frac{sa_k\delta}{r^{\alpha_L}}}\right) f_{R_x^a}(r|v)dr\right), \tag{5.43}$$

$$\mathcal{L}_{I^e}(s|v) = \exp\left(-2\pi\lambda_p \int_v^\infty (1-\beta_L(y,s))yp_L(y)dy\right), \tag{5.44}$$

$$\beta_L(y,s) = \exp\left(-n\sum_{k=1}^{4} b_k \int_{\mathcal{R}} \left(1 - \frac{1}{1+\frac{sa_k\delta}{r^{\alpha_L}}}\right) f_{R_x^e}(r|v)dr\right), \tag{5.45}$$

$s = \frac{\gamma v^{\alpha_L}}{\delta M_b M_u}$, $f_{R_s}^{CS}(v|L)$ *is given in* ***Lemma 5.1****,* a_k *and* b_k *are antenna direc-*

tivity parameters as defined in Section 5.2.2, $f_{R_x^a}(r|v)$ *and* $f_{R_x^e}(r|v)$ *are given in* ***Lemma 5.5*** *and* ***Lemma 5.6****, respectively.*

Proof. The proof follows directly from **Theorem 5.3** and the fact that $t^{\alpha_L \epsilon} = 1$ when $\epsilon = 0$. □

Note that the Laplace transforms of intra-cluster and inter-cluster interference in (5.43) and (5.44) are similar to that in [93, Theorem 3]. Specifically, in [93, Theorem 3], the computations of these Laplace transforms require double integrals. However, by using the distance distributions as derived in **Lemma 5.5** and **Lemma 5.6**, we simplify the Laplace transforms in [93, Theorem 3] to a single integration as given in (5.43) and (5.44). Thus, the computation complexity in **Corollary 5.1** is $\mathcal{O}(\mathbb{R})$, unlike [93, Theorem 3] with $\mathcal{O}(\mathbb{R}^2)$. Moreover, the derivation approach in **Corollary 5.1** are more tractable and much easier to numerically evaluate.

5.4 Performance Evaluation and Trends

In this section, we provide numerical results to validate the accuracy of our analysis. We consider Monte Carlo simulations for the system in a square area of 5 km x 5 km. The simulation results are obtained by averaging over 10 000 realizations. In each simulation run, BSs, UEs and cluster centers are randomly dropped according to the corresponding intensities. We assume that the MMW network is operated at 73 GHz with bandwidth of 100 MHz allocated to each user. The path LoS and non-LoS path loss exponents are set to $\alpha_L = 2$ and $\alpha_N = 4$, respectively. The noise power is given by σ^2(dBm)= -174 dBm/Hz+$10\log_{10}(BW) + 10$ dB. The parameters for the sectored antenna model at the BSs are set to M_b =18 dBi, m_b =-2 dBi, ω_b =10^o [88], while the parameters for the sectored antenna model at the UEs are set to M_u =10 dBi, m_b =-10 dBi, ω_b =30^o [96].

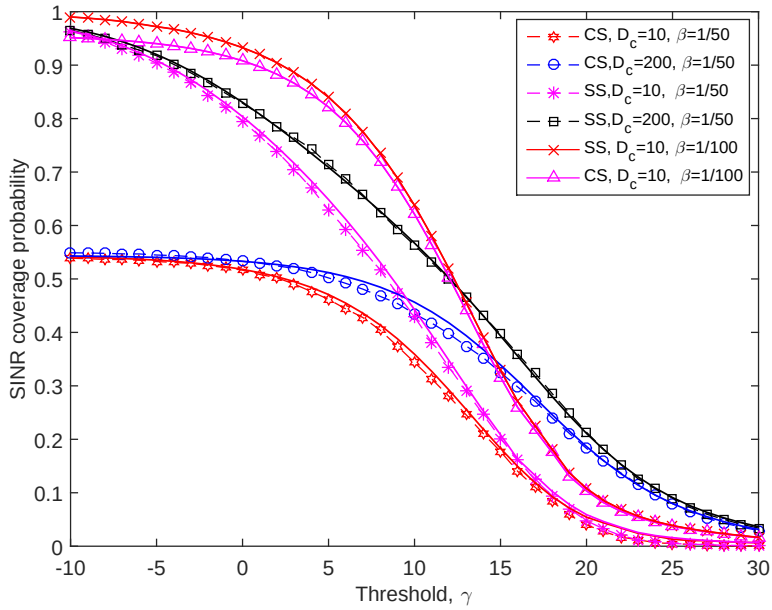

(a) No power control $\epsilon = 0$

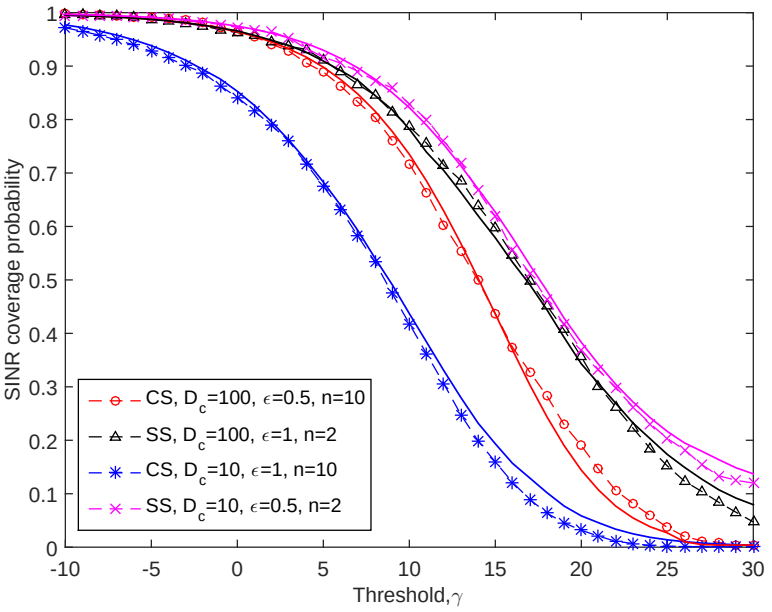

(b) FPC factor $\epsilon = 0.5, 1$

Figure 5.4. SINR coverage probability in the uplink MMW. The solid lines are results obtained from the analytical expressions. The markers are results from the simulations.

1) Accuracy of the analytical model: In Fig. 5.4, we compare the SINR coverage probabilities obtained from **Theorem 5.3** and **Theorem 5.4** with the simulation results for $\epsilon = 0, 0.5, 1$, and cluster radius $D_c = 10, 100, 200$. The results in Fig. 5.4 (a) show a very close match which indicates that the approximations made in the analytical derivation, result in a negligible error. We note in Fig. 5.4 (b) that the gap of the SINR distributions become visible especially for high SINR threshold. This gap is reasonable due to the independent assumption of the distance from the interfering UE to its serving BS in (5.19) and (5.20). We also see from Fig. 5.4 (a) that the large size of the cluster gives better SINR coverage in both CS and SS association strategies. This is because the distance between the typical BS and the interfering UE increases with the cluster size, which therefore reduces the interfering signals. Another important observation is that the results in Fig. 5.4 (a) show that there is a difference between the SINR coverage probabilities achieved by CS and SS strategies. We refer to this difference as *coverage gain* for the rest of the chapter. It is clear from Fig. 5.4 (a) that the coverage gains reduce with the decrease of blockage parameter β. The following section investigates the impact of β.

2) Effect of blockage: Fig. 5.5 illustrates the SINR coverage probability as a function of blockage parameter for CS and SS strategies when the power control $\epsilon = 0$. We can see that the SS strategy has greater SINR coverage probability at the dense building environment, e.g., $\beta > 10^{-2}$ for both target thresholds $\gamma = 5$ dB and $\gamma = 15$ dB, compared with CS strategy. The coverage gain increases as the blockage parameter rises, which indicates the importance of the non-LoS propagation in an urban environment with dense buildings. Intuitively, in the area with sparse buildings, the likelihood of a UE communicating with a LoS BS is higher than areas surrounded by dense buildings. Therefore, considering only the LoS cluster is sufficient to characterize the SINR performance. On the other hand, the MMW communications mainly rely on non-LoS propagation as

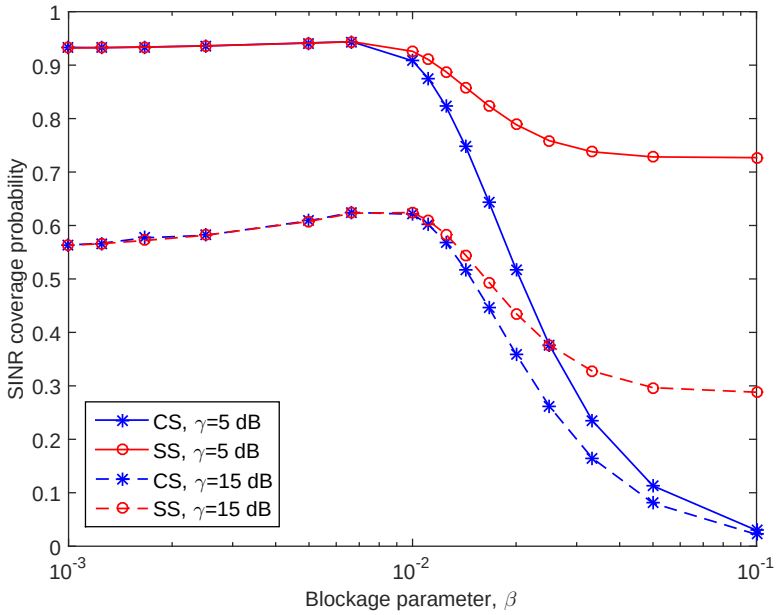

Figure 5.5. Effect of blockage on the SINR coverage probability for CS and SS strategies.

the density of buildings increases. Thus, SS strategy is preferable for the MMW networks in the urban area with dense buildings.

3) Effect of FPC factor ϵ: Next, we study the impact of the FPC factor on the SINR coverage. As mentioned in Section 5.2.4, the fundamental motivations of the FPC in the cellular uplink are to provide performance improvements for the lowest-percentile UEs and manage the power consumption of UEs. We plot in Fig. 5.6 the SINR coverage probability for various FPC factors. Here we assume that the blockage parameter $\beta = 1/50, 1/100$, and the average number of UEs per cluster $n = 10$. To observe the impact of the FPC, we also plot the baseline case, which refers to $\epsilon = 0$. We observe from both Fig. 5.6 (a) and Fig. 5.6 (b) that the baseline case does not provide the lowest SINR coverage probability in both CS and SS strategies. Regarding the CS strategy, for the case of $\beta = 1/50$ in Fig. 5.6 (a), the largest SINR coverage probability for UEs in the lower 50 percentile is given by $\epsilon = 0.25$, followed by $\epsilon = 0.5$, having gained over the baseline case for overall coverage probability. However, for the SINR thresholds $\gamma < 10$ dB, the full path loss compensation $\epsilon = 1$ causes the coverage probability to drop

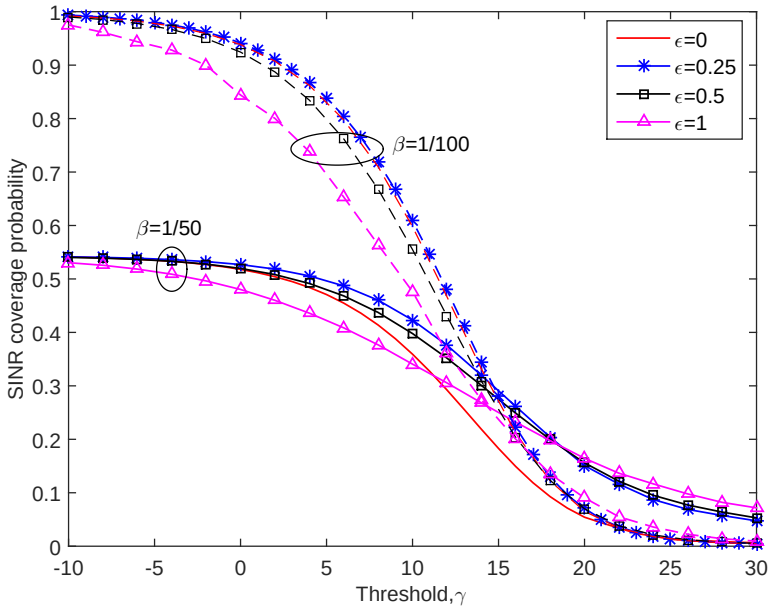

(a) CS strategy

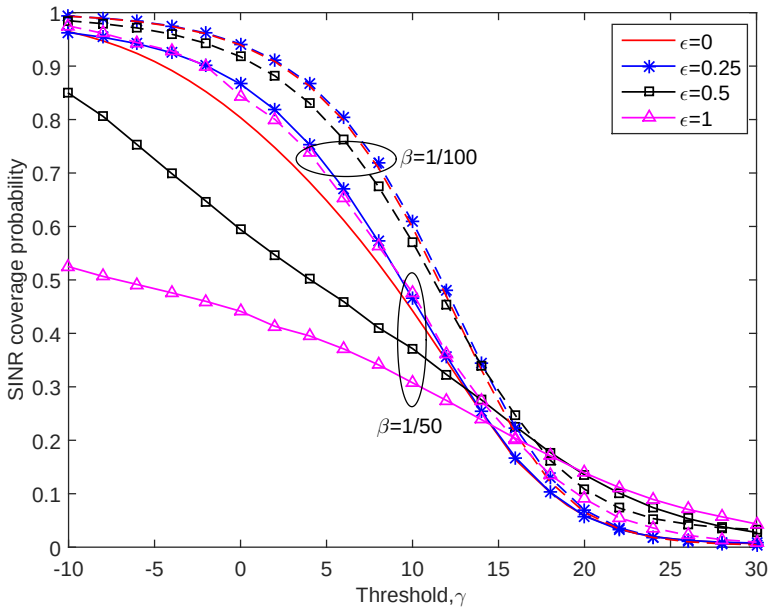

(b) SS strategy

Figure 5.6. SINR coverage probability in the uplink MMW for various FPC factors. The solid lines are the coverage probabilities for the case $\beta = 1/50$. The dash lines are the coverage probabilities for the case $\beta = 1/100$.

below the baseline case. Meanwhile, for the case of $\beta = 1/50$ in Fig. 5.6 (b), the highest SINR coverage probability achieved by $\epsilon = 0.25$. As the FPC factor ϵ rises, the coverage probability shifts below the baseline case before crossing above the baseline curve at $\gamma = 12$ dB. We also note that for the case $\beta = 1/100$ in both CS and SS strategies, the difference in coverage probability for the baseline and $\epsilon = 0.25$ is negligible, which indicates that the FPC does not provide a significant improvement in the SINR coverage probability in the environment with sparse blockages. Although transmitting at full path loss compensation $\epsilon = 1$ gives some improvement especially at thresholds $\gamma > 15$ dB, it causes even more reduction in the coverage probability, especially in the low SINR thresholds.

4) Effect of BS Intensity: Fig. 5.7 plots the SINR coverage probability as a function of the BS intensity for the case without FPC, i.e., $\epsilon = 0$. We can see from Fig. 5.7 that all curves first increase monotonically with the BS intensity. After achieving their maximum points, these curves decrease with the increasing BS intensity. This is because having more BS will generally improve the coverage in the noise-limited regime. However, in the interference-limited regime, increasing BS intensity will lead to more interference and consequently reduce the received SINR. For a given SINR threshold and for a given FPC factor, there exists an optimal BS intensity that maximizes the SINR coverage probability. For example, at $\gamma = 5$ dB and $\epsilon = 0$, the SINR coverage probabilities are maximized at $\lambda_b = 100/\text{km}^2$ and $\lambda_b = 180/\text{km}^2$ for CS and SS strategies, respectively. We also see that the SS strategy outperforms the CS strategy at the low BS density and converges to the CS strategy at the high BS density. This result is expected since by increasing BS intensity, more links between the UEs and their associated BSs are in LoS. Therefore, the probability that the UE connected to the LoS BS increases, so the SS strategy converges to the CS strategy when the association probability in (5.15), $\mathcal{A}_L \to 1$.

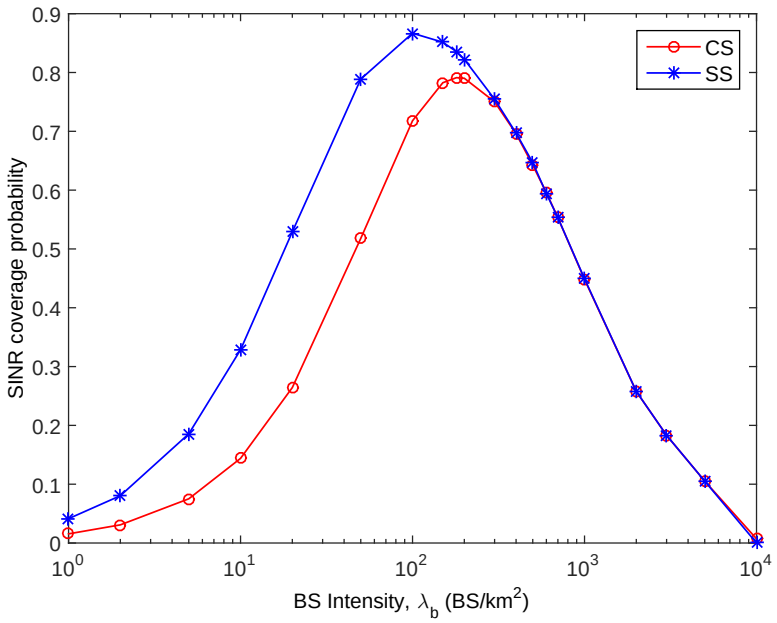

Figure 5.7. Effect of BS intensity on the SINR coverage probability for CS and SS strategies.

5.5 Chapter Summary

In this chapter, we proposed a general analytical framework to compute the SINR coverage probability in the uplink MMW cellular networks. We modeled the locations of BS as a PPP, whereas the locations of user following a PCP to represent the clustered users scenario. We assumed that the users and BSs are equipped with sectorized antennas. For this framework, we derived the SINR coverage in the uplink MMW cellular network that incorporates the effect of MMW properties, FPC and UE association strategies. The presented results showed that the large size of the cluster could significantly improve the SINR coverage probability due to the increasing distance from the interfering UEs to the typical BS. Furthermore, by considering the FPC at the UE, we demonstrated that a proper selection of the FPC factor is required to provide acceptable performance for the majority of UEs and maintain high overall system capacity.

Chapter 6

Conclusion

This thesis presented stochastic geometry frameworks for MMW channel modeling and performance analysis to evaluate the system level performances of outdoor MMW cellular networks. In the following, we summarize the key results and insights of this thesis and then provide some potential avenues for future research.

6.1 Summary of results and insights

In chapter 3, we proposed a stochastic channel model for point-to-point MMW systems in outdoor environments. In this channel model, we incorporated the environment features to capture the effects of the first-order reflection paths generated by randomly distributed buildings. We developed an approximate but accurate closed-form expression for the PDP contributed by all the first-order reflection paths and derived a semi-analytical result for the average number of the first-order reflection paths. Numerical results demonstrated that these approximate expressions are very tight under all the considered system settings. The presented results demonstrated that wireless networks might benefit from buildings in the area of MMW communication links since the external surfaces of these buildings render reflection paths that can provide a comparable signal power to that of the LoS path. Furthermore, the proposed channel model also

revealed that there exists an optimal system setting that can contribute to the maximum power of the first-order reflection paths. The findings in this chapter can provide useful insights to develop more complex channel models applicable to future MMW systems.

In chapter 4, we developed a mathematical framework to analyze the performance of inter-cell interference coordination in the dense MMW cellular networks. By leveraging the concepts from stochastic geometry and incorporating the distinguishing features of MMW communications, we derived numerically tractable expressions for the coverage probability and ASE for the downlink MMW cellular networks. The simulation results matched very well and confirmed that the proposed BS coordination significantly outperformed the non-coordinated case in terms of coverage probability. Also, the results showed that there exists an optimum cluster size that leads to the maximum ASE depending on the value of the blockage parameter.

Finally, in chapter 5, we turned our attention to study the performance of the uplink MMW cellular network by considering the clustered UEs scenario. To analyze the SINR coverage in the uplink MMW cellular network, we proposed a stochastic geometry framework that incorporates the effect of MMW properties, FPC and UE association strategies. The presented results showed that the large size of the cluster could significantly improve the SINR coverage probability due to the increasing distance from the interfering UEs to the typical BS. Furthermore, by considering the FPC at the UE, we demonstrated that a proper selection of the FPC factor is required to provide acceptable performance for the majority of UEs and maintain high overall system capacity.

6.2 Future work

In addition to the key results and findings summarized above, there are still some new directions and extensions of the work developed in this thesis to be investigated in the future.

In chapter 3, the channel modeling for the first-order reflection paths was studied considering the two-dimensional propagation environment and system parameters. A natural extension would be to develop a three-dimensional analytical channel model for outdoor MMW multipath propagation. The model will help to understand the impact of high rise buildings and antenna height on the received signal power, angle spread and delay spread of the multipath components. It would also be interesting to include the directional antenna properties in the channel model since the vision is to equip future wireless networks operating at MMW bands with massively high directional antennas.

In chapter 4, we focus on the downlink performance of the MMW cellular networks. In particular, the BSs were assumed to be equipped with directional antenna while the typical UE employs a single omnidirectional antenna. In the future, all MMW cellular networks will deploy directional antenna arrays at both BSs and UEs. It is natural to consider the directional antennas at both BSs and UEs, and use the similar analytical approach as that in Chapter 4 for analyzing the downlink SINR performance. Also, it would be interesting to include the effect of beam alignment in the analysis. In [100, 93], it was demonstrated that the performance loss varied depending on the antenna model and system parameters.

The contribution in Chapter 5 focuses on the uplink SINR performance of the MMW cellular networks. In the future cellular networks, the MMW will coexist with conventional microwave cellular networks as a potential solution to overcome the coverage hole due to blockages. Although the interference of these two frequencies are independent, the SINR distributions are correlated in reality. For example, some of the microwave and MMW transmitters may be co-located

depending on hotspot regions. Thus, ignoring the correlation of transmitters distributions can lead to incorrect conclusions. Also, the different propagation characteristics of the MMW and microwave bands and the bandwidth disparity would result in significant load imbalance as it may be desirable to get access from the MMW BSs that provide much lower SINR than the conventional microwave BSs. As a future work, it would be interesting to study the correlations of BSs locations and load balancing, which can help to understand the performance gains of hybrid MMW and microwave band systems.

Appendix A

Proofs for Chapter 3

A.1 Derivation of (3.16)

To formulate $S_{FF'I'I}$ in (3.16), let us return to (3.15). After the similar derivations to those for (3.12) and (3.13), except that we replace τ with $\tau + \Delta\tau$, we have the coordinates of the reflection point R'_1, denoted by (x', y'), as

$$x' = \frac{-c^2(\tau+\Delta\tau)^2 \tan\theta}{2\sqrt{c^2(\tau+\Delta\tau)^2 \sec^2\theta - D^2}} = x + \frac{c^2\tau\Delta\tau \tan\theta(2D^2 - c^2\tau^2\sec^2\theta)}{2(c^2\tau^2\sec^2\theta - D^2)^{3/2}}, \quad \text{(A.1)}$$

and

$$y' = \frac{c^2(\tau+\Delta\tau)^2 - D^2}{2\sqrt{c^2(\tau+\Delta\tau)^2 \sec^2\theta - D^2}} = y + \frac{c^2\tau\Delta\tau(c^2\tau^2\sec^2 - 2D^2 + D^2\sec^2\theta)}{2(c^2\tau^2\sec^2\theta - D^2)^{3/2}}. \quad \text{(A.2)}$$

Note that the second equalities of (A.1) and (A.2) are obtained by ignoring all terms that contain $(\Delta\tau)^2$, which is reasonable when $\Delta\tau$ is sufficiently small.

Given the coordinates of the points R_1 and R'_1, we can easily find the expres-

sion of the vector $\overrightarrow{RR'}$, which is identical to the vector $\overrightarrow{FF'}$. Hence we have

$$\overrightarrow{FF'} = \overrightarrow{RR'_1} = \begin{bmatrix} x' - x \\ y' - y \end{bmatrix} = \begin{bmatrix} \frac{c^2\tau\Delta\tau\tan\theta(2D^2 - c^2\tau^2\sec^2\theta)}{2(c^2\tau^2\sec^2\theta - D^2)^{3/2}} \\ \frac{c^2\tau\Delta\tau(c^2\tau^2\sec^2 - 2D^2 + D^2\sec^2\theta)}{2(c^2\tau^2\sec^2\theta - D^2)^{3/2}} \end{bmatrix}, \tag{A.3}$$

and its norm can be written as

$$|\overrightarrow{FF'}| = \sqrt{(x' - x)^2 + (y' - y)^2} = \frac{c^2\tau\Delta\tau\sqrt{c^4\tau^4\sec^6\theta + D^4\sec^4\theta - 2D^2c^2\tau^2\sec^4\theta}}{2(c^2\tau^2\sec^2\theta - D^2)^{3/2}}. \tag{A.4}$$

Meanwhile, the vector $\overrightarrow{FI}$ can be expressed as

$$\overrightarrow{FI} = \begin{bmatrix} -l\cos\hat{\mathrm{a}}\cdot\theta \\ -l\sin\hat{\mathrm{a}}\cdot\theta \end{bmatrix}, \tag{A.5}$$

with its norm being

$$|\overrightarrow{FI}| = \sqrt{l^2\cos^2\theta + l^2\sin^2\theta} = l. \tag{A.6}$$

Denote by ψ the angle between vectors $\overrightarrow{FF'}$ and $\overrightarrow{FI}$. Then, we have

$$\cos\psi = \frac{\overrightarrow{FF'}\cdot\overrightarrow{FI}}{|\overrightarrow{FF'}||\overrightarrow{FI}|}. \tag{A.7}$$

Mathematically, the area of the parallelogram $FF'I'I$ can be written as

$$\begin{aligned} S_{FF'I'I} &= |\overrightarrow{FF'}||\overrightarrow{FI}|\sin\psi = |\overrightarrow{FF'}||\overrightarrow{FI}|\sqrt{1 - \cos^2\psi} \\ &= \sqrt{|\overrightarrow{FF'}|^2|\overrightarrow{FI}|^2 - (|\overrightarrow{FF'}||\overrightarrow{FI}|\cos\psi)^2}. \end{aligned} \tag{A.8}$$

Thus, by substituting (A.4),(A.6) and (A.7) into (A.8), we obtain the expression for $S_{FF'I'I}$ as written in (3.16).

A.2 Proof of Theorem 1

The first-order reflection path with its reflection point at R_1 will occur when there is at least one building whose center falls within the $FF'I'I$ region. Thus we have

$$\mathbb{P}(E_1|\mathcal{N}_{R_1}) = \mathbb{P}(K_{RF_1} > 0) = 1 - \mathbb{P}(K_{RF_1} = 0) \tag{A.9}$$

where[1]

$$\mathbb{P}(K_{RF_1} = 0) = \frac{(\mathbb{E}[K_{RF_1}])^0}{0!} e^{-\mathbb{E}[K_{RF_1}]} = e^{-\lambda \frac{\mathbb{E}[l] c^2 \tau \Delta\tau}{2\sqrt{c^2\tau^2 - D^2\cos^2\theta}}}. \tag{A.10}$$

Substituting (3.15) and (A.9) into (3.14), we have

$$f_{RF_1}(\tau|\theta) = \lim_{c\Delta\tau \to 0} \frac{1 - e^{-\lambda \frac{\mathbb{E}[l] c^2 \tau \Delta\tau}{2\sqrt{c^2\tau^2 - D^2\cos^2\theta}}}}{c\Delta\tau}. \tag{A.11}$$

Finally, using the L'Hospital rule [102], we can rewrite (A.11) as

$$f_{RF_1}(\tau|\theta) = \lim_{c\Delta\tau \to 0} \frac{\lambda \frac{\mathbb{E}[l] c\tau}{2\sqrt{c^2\tau^2 - D^2\cos^2\theta}} e^{-\lambda \frac{\mathbb{E}[l] c^2 \tau \Delta\tau}{2\sqrt{c^2\tau^2 - D^2\cos^2\theta}}}}{1} = \lambda \frac{\mathbb{E}[l] c\tau}{2\sqrt{c^2\tau^2 - D^2\cos^2\theta}}. \tag{A.12}$$

which completes the proof.

A.3 Derivation of (3.20)

From Fig. 3.4, the area of the blockage region $JKQTZWUEM$ can be express as

$$S_{JKQTZWUEM} = S_{JKQTSM} + S_{UPQTZW} - S_{PQTS} - S_{PSE}, \tag{A.13}$$

[1]For a Poisson distributed random variable x with expectation $\mathbb{E}[x]$, we have $\mathbb{P}(x = n) = \frac{\mathbb{E}[x]^n e^{-\mathbb{E}[x]}}{n!}$ [101].

where each term on the right hand-side is interpreted individually as follows. Specifically, the region $JKQTSM$ consists of two right-angled triangles JKM and QTS, and a parallelogram $KQSM$ with height denoted by h_1 and base $|\mathrm{Tx}R_1|$, which is the length of the line segment $\mathrm{Tx}R_1$. This area is given by

$$S_{JKQTSM} = \frac{lw}{2} + \frac{lw}{2} + |\mathrm{Tx}R_1| \cdot h_1 = lw + |\mathrm{Tx}R_1| \cdot h_1. \tag{A.14}$$

Let us first return to Fig. 3.4 and introduce some notations to facilitate the derivation of h_1. Denote by γ_1 the angle between the l-side wall of building and the line segment $\mathrm{Tx}R_1$. As illustrated in Fig. 3.4, the value of h_1 can be obtained by the trigonometric formula as

$$h_1 = \sin(\phi_1 + \phi_1')\sqrt{l^2 + w^2}, \tag{A.15}$$

where ϕ_1 is the angle between the l-side wall of building and the line segment KM and $\phi_1' = \gamma_1$. Then, by using the trigonometric identity, we have

$$\begin{aligned} h_1 &= (\sin\gamma_1 \cos\phi_1 + \cos\gamma_1 \sin\phi_1)\sqrt{l^2 + w^2} \\ &= \left(\sin\gamma_1 \frac{l}{\sqrt{l^2 + w^2}} + \cos\gamma_1 \frac{w}{\sqrt{l^2 + w^2}}\right)\sqrt{l^2 + w^2}. \end{aligned} \tag{A.16}$$

Next, let us derive the expression for $\sin\gamma_1$ and $\cos\gamma_1$. Denote by θ_a the angle between the x-axis and the line segment $\mathrm{Tx}R_1$ as illustrated in Fig. 3.4. The slope of the line segment $\mathrm{Tx}R_1$ is given by

$$\tan\theta_a = \frac{y}{x + D/2}. \tag{A.17}$$

By recalling the definition of θ in assumption 4, we have

$$\gamma_1 = \pi - (\theta - \theta_a). \tag{A.18}$$

Applying the trigonometric function on both sides of (A.18), we have

$$\tan\gamma_1 = \tan(\pi - (\theta - \theta_a)) = -\tan(\theta - \theta_a) = -\frac{\tan\theta - \tan\theta_a}{1 + \tan\theta\tan\theta_a}. \tag{A.19}$$

Then, substituting (3.10) and (A.17) into (A.19), we obtain

$$\tan\gamma_1 = \frac{\sqrt{c^2\tau^2 - D^2\cos^2\theta}}{D|\cos\theta|} \tag{A.20}$$

or equivalently

$$\gamma_1 = \arctan\left(\frac{\sqrt{c^2\tau^2 - D^2\cos^2\theta}}{D|\cos\theta|}\right). \tag{A.21}$$

From (A.21) and by using some trigonometric identities, we can express the simplified $\sin\gamma_1$ and $\cos\gamma_1$ as, respectively,

$$\sin\gamma_1 = \sin\left(\arctan\left(\frac{\sqrt{c^2\tau^2 - D^2\cos^2\theta}}{D|\cos\theta|}\right)\right) = \frac{\sqrt{c^2\tau^2 - D^2\cos^2\theta}}{c\tau}, \tag{A.22}$$

and

$$\cos\gamma_1 = \cos\left(\arctan\left(\frac{\sqrt{c^2\tau^2 - D^2\cos^2\theta}}{D|\cos\theta|}\right)\right) = \frac{D|\cos\theta|}{c\tau}. \tag{A.23}$$

Finally, by substituting (A.22) and (A.23) into (A.16), we obtain

$$h_1 = \frac{l\sqrt{c^2\tau^2 - D^2\cos^2\theta}}{c\tau} + \frac{wD|\cos\theta|}{c\tau}. \tag{A.24}$$

Similarly, the region $UPQTZW$ is the combined area of two right-angled triangles PQT and UZW, and a parallelogram $UPTZ$ with height denoted by h_2 and base $|R_1\mathrm{Rx}|$, which is the length of the line segment $R_1\mathrm{Rx}$. This area is

given by

$$S_{UPQTZW} = \frac{lw}{2} + \frac{lw}{2} + |R_1\mathrm{Rx}| \cdot h_2 = lw + |R_1\mathrm{Rx}| \cdot h_2 \tag{A.25}$$

where after the similar derivation as (A.24), we have $h_2 = h_1$. Meanwhile, the region $PQTS$ is a rectangle, whose area can be calculated as

$$S_{PQTS} = lw. \tag{A.26}$$

Next, we calculate the area of the region PSE. Intuitively, it can be seen that the area and shape of this region depend on the building orientation θ. In one extreme case when $\theta = \pi/2$, this region is of a rectangle shape whose area is given by

$$S_{PSE} = \frac{l(c\tau - D)}{2}. \tag{A.27}$$

In the other extreme case when $\theta = \pi$, the shape of the region PSE is a triangle, which is given by

$$S_{PSE} = \frac{tl}{2} \tag{A.28}$$

where t is the height of the triangle. Note that $\angle EPS$ in Fig. 3.4 is equal to γ_1. Thus we have

$$t = \frac{l \tan\gamma_1}{2}. \tag{A.29}$$

From (A.20), for the case of $\theta = \pi$, we have

$$\tan\gamma_1 = \frac{\sqrt{c^2\tau^2 - D^2\cos^2\theta}}{D|\cos\theta|} = \frac{\sqrt{c^2\tau^2 - D^2}}{D}. \tag{A.30}$$

Substituting (A.29) and (A.30) into (A.28), we have

$$S_{PSE} = \frac{l^2\sqrt{c^2\tau^2 - D^2}}{4D}. \tag{A.31}$$

Meanwhile, for the general case of $\pi/2 < \theta < \pi$, the region PSE is a trapezium. Though we can analytically derive the exact area of such a region as a function of θ, we find that the resultant expression is much complicated, which makes the subsequent derivation very complex. Thus, we present an approximate but sufficiently accurate expression for the area of the region PSE by only taking average between the aforementioned two extreme cases, i.e.,

$$S_{PSE} \approx \frac{l(c\tau - D)}{4} + \frac{l^2\sqrt{c^2\tau^2 - D^2}}{8D}. \tag{A.32}$$

Finally, by substituting (A.14), (A.25), (A.26) and (A.32) into (A.13), we obtain the area of the blockage region $JKQTZWUEM$ as

$$\begin{aligned} S_{JKQTZWUEM} &\approx (|\mathrm{Tx}R_1| + |R_1\mathrm{Rx}|)h_1 + lw - \frac{l(c\tau - D)}{4} - \frac{l^2\sqrt{c^2\tau^2 - D^2}}{8D} \\ &\overset{(a)}{=} c\tau h_1 + lw - \frac{l(c\tau - D)}{4} - \frac{l^2\sqrt{c^2\tau^2 - D^2}}{8D} \end{aligned} \tag{A.33}$$

where the equality (a) holds because the total length of $|\mathrm{Tx}R_1|$ and $|R_1\mathrm{Rx}|$ is equal to the path length of the considered first-order reflection path $L_r = c\tau$. This completes the proof.

A.4 Proof of Theorem 2

Since the first-order reflection path will occur when there is no building whose center falls within the blockage region $JKQTZWUEM$, we have

$$f_{NB_1}(\tau|\theta) = \mathbb{P}(K_{NB_1} = 0) = \frac{(\mathbb{E}[K_{NB_1}])^0}{0!} e^{-\mathbb{E}[K_{NB_1}]}. \tag{A.34}$$

Substituting (3.22) into (A.34), we can directly obtain the $f_{NB_1}(\tau|\theta)$ as in the Theorem 2.

A.5 Derivation of (3.31)

We first substitute (3.28) and (3.30) into (3.4) and obtain

$$f_{SR}(\tau) = \frac{1}{\pi}\left(\int_0^{\pi/2} f_{SR}(\tau|\theta)\, d\theta + \int_{\pi/2}^{\pi} f_{SR}(\tau|\theta)\, d\theta\right). \tag{A.35}$$

We notice that when the value of φ in the first term on the right hand side of (A.35) is $\varphi = \pi - \theta$, the resulting $f_{SR}(\tau|\theta)$ and the $f_{SR}(\tau|\theta)$ in the second term on the right hand side of (A.35) are symmetric about $\pi/2$. Thus, we can further simplify (A.35) as

$$\begin{aligned}
f_{SR}(\tau) &= \frac{2}{\pi}\int_{\pi/2}^{\pi} f_{SR}(\tau|\theta)\, d\theta \\
&\approx \frac{2}{\pi}\int_{\pi/2}^{\pi} \frac{\lambda\mathbb{E}[l]c\tau}{\sqrt{c^2\tau^2 - D^2\cos^2\theta}} \cdot \exp\Bigg(-\lambda\Bigg(\mathbb{E}[l]\sqrt{c^2\tau^2 - D^2\cos^2\theta} + \mathbb{E}[w]D\,|cos\theta| \\
&\quad + \mathbb{E}[l]\mathbb{E}[w] - \frac{\mathbb{E}[l](c\tau - D)}{4} - \frac{\mathbb{E}[l]^2\sqrt{c^2\tau^2 - D^2}}{8D}\Bigg)\Bigg) d\theta \\
&\quad + \frac{2}{\pi}\int_{\pi/2}^{\pi} \frac{\lambda\mathbb{E}[w]c\tau}{\sqrt{c^2\tau^2 - D^2\cos^2\theta}} \cdot \exp\Bigg(-\lambda\Bigg(\mathbb{E}[w]\sqrt{c^2\tau^2 - D^2\cos^2\theta} + \mathbb{E}[l]D\,|cos\theta| \\
&\quad + \mathbb{E}[w]\mathbb{E}[l] - \frac{\mathbb{E}[w](c\tau - D)}{4} - \frac{\mathbb{E}[w]^2\sqrt{c^2\tau^2 - D^2}}{8D}\Bigg)\Bigg) d\theta.
\end{aligned} \tag{A.36}$$

Next, we let $a = c\tau/D$. For simplicity, we perform an approximation of $|\cos\theta|$ in the exponential function of (A.36). The approximated expression can be written as

$$\begin{aligned}
|\cos\theta| &= \frac{(\sqrt{a^2-1} - a)\cos\theta + a}{\sqrt{a^2-1} - a} - \frac{a}{\sqrt{a^2-1} - a} \\
&\approx \frac{\sqrt{a^2 - \cos^2\theta}}{\sqrt{a^2-1} - a} - \frac{a}{\sqrt{a^2-1} - a}.
\end{aligned} \tag{A.37}$$

Therefore, by replacing (A.37) into (A.36), we have

$$f_{SR}(\tau) \approx \int_{\pi/2}^{\pi} \frac{\zeta_1' \exp(-b_1\sqrt{a^2-\cos^2\theta})}{\sqrt{a^2-\cos^2\theta}} + \int_{\pi/2}^{\pi} \frac{\zeta_2' \exp(-b_2\sqrt{a^2-\cos^2\theta})}{\sqrt{a^2-\cos^2\theta}} \quad \text{(A.38)}$$

where

$$\zeta_1' = \lambda\mathbb{E}[l]a\exp\left(-\lambda\mathbb{E}[l]\mathbb{E}[w] + \frac{\lambda\mathbb{E}[l]D(a-1)}{4} + \frac{\lambda\mathbb{E}[l]^2\sqrt{a^2-1}}{8} + \frac{\lambda\mathbb{E}[w]Da}{\sqrt{a^2-1}-a}\right)$$
$$b_1 = \lambda D\left(\mathbb{E}[l] + \frac{\mathbb{E}[w]}{\sqrt{a^2-1}-a}\right)$$
$$\zeta_2' = \lambda\mathbb{E}[w]a\exp\left(-\lambda\mathbb{E}[w]\mathbb{E}[l] + \frac{\lambda\mathbb{E}[w]D(a-1)}{4} + \frac{\lambda\mathbb{E}[w]^2\sqrt{a^2-1}}{8} + \frac{\lambda\mathbb{E}[l]Da}{\sqrt{a^2-1}-a}\right)$$
$$b_2 = \lambda D\left(\mathbb{E}[w] + \frac{\mathbb{E}[l]}{\sqrt{a^2-1}-a}\right).$$

Next, we perform the first-order Taylor expansions for $\sqrt{a^2-\cos^2\theta}$, $\exp(-b_1\sqrt{a^2-\cos^2\theta})$ and $\exp(-b_2\sqrt{a^2-\cos^2\theta})$, separately at $\theta = \frac{3\pi}{4}$. Their first-order Taylor expansions are given as

$$\sqrt{a^2-\cos^2\theta} \approx \eta - \frac{3\pi}{8\eta} + \frac{\theta}{2\eta} \quad \text{(A.39)}$$

where $\eta = \sqrt{a^2-(1/2)}$,

$$\exp(-b_1\sqrt{a^2-\cos^2\theta}) \approx \exp(-b_1\eta)\left(1 + \frac{3\pi b_1}{8\eta}\right) - \frac{b_1\exp(-b_1\eta)}{2\eta}\theta, \quad \text{(A.40)}$$

and

$$\exp(-b_2\sqrt{a^2-\cos^2\theta}) \approx \exp(-b_2\eta)\left(1 + \frac{3\pi b_2}{8\eta}\right) - \frac{b_2\exp(-b_2\eta)}{2\eta}\theta. \quad \text{(A.41)}$$

Finally, substituting (A.39), (A.40) and (A.41) into (A.38), we obtain the closed-form approximation for the $f_{SR}(\tau)$ as in (3.31).

Appendix B

Proofs for Chapter 5

B.1 Proof of Lemma 5.1

Denote by r the distance between a BS to a LoS user. Using the transformation $r = t^{1/\alpha_L}$ and the mapping theorem [65], the intensity measure for LoS user is given by

$$\begin{aligned}
\Lambda_L([0,t)) &= 2\pi\lambda_b \int_0^\infty \mathbb{P}(r^{\alpha_L} < t) e^{-\beta r} r dr \\
&= 2\pi\lambda_b \int_0^\infty \mathbb{E}\left[1(r < t^{\frac{1}{\alpha_L}})\right] e^{-\beta r} r dr \\
&= 2\pi\lambda_b \int_0^{t^{\frac{1}{\alpha_L}}} e^{-\beta r} r dr \\
&= \frac{2\pi\lambda_b}{\beta^2}\left(1 - e^{-\beta t^{1/\alpha_L}}\left(1 + \beta t^{1/\alpha_L}\right)\right). \qquad \text{(B.1)}
\end{aligned}$$

Next, we can obtain the intensity of the LoS UE as

$$\lambda_L(t|L) = \frac{d\Lambda_L[0,t)}{dt}. \qquad \text{(B.2)}$$

Consequently, the distribution of the distance R_s to the closest LoS BS

$$\mathbb{P}[R_s > r] = \exp\left(-\frac{2\pi\lambda_b}{\beta^2}\left(1 - e^{-\beta r}\left(1 + \beta r\right)\right)\right) \qquad \text{(B.3)}$$

and the PDF of R_s is given as in **Lemma 5.1**.

B.2 Proof of Lemma 5.2

Given that the typical user has at least one LoS BS, the conditional probability density function of its distance to the nearest LoS BS is given as

$$f_L(x) = 2\lambda_b \pi x p(x) \exp\left(-2\lambda_b \pi \int_0^x r p_L(r) dr\right) / \mathcal{B}_L \tag{B.4}$$

where $r > 0$, $\mathcal{B}_L = 1 - \exp\left(-2\lambda_b \pi \int_0^\infty r p_L(r) dr\right)$ refers to the probability that a user has at least one LoS BS and $p_L(r)$ is the LoS probability as given in Section 5.2.1.

Next, we derive the probability that the user is served by a LoS BS as in the following. Let d_c be the distance from the typical user to its nearest BS in Φ_b^c with $c = \{L, N\}$. The user is served by a BS in Φ_b^L if and only if it observe an LoS BS, and its nearest BS in Φ_b^L has smaller path loss than that of the nearest BS in Φ_b^N. Thus, we have

$$\begin{aligned} \mathcal{A}_L &= \mathcal{B}_L \mathbb{P}\left(\delta d_L^{-\alpha_L} > \delta d_N^{-\alpha_N}\right) \\ &= \mathcal{B}_L \int_0^\infty \mathbb{P}\left(d_N > x^{\alpha_L/\alpha_N}\right) f_L(x) dx, \end{aligned} \tag{B.5}$$

where $\mathcal{B}_L$ is the probability that the user has at least one LoS BS and $\vartheta_L(x) = x^{\alpha_L/\alpha_N}$.

$$\begin{aligned} \mathbb{P}\left(d_N > \vartheta_L(x)\right) &= \mathcal{P}\left(\Phi_b^N \cap \mathcal{B}(0, \vartheta_L(x)) = \emptyset\right) \\ &= \exp\left(-2\lambda_b \pi \int_0^{\vartheta_L(x)} p_N(t) t dt\right) \end{aligned} \tag{B.6}$$

where $\mathcal{B}(0, x)$ denotes the ball centered at the origin of radius x and $p_N(t)$ is the non-LoS probability as given in Section 5.2.1. Then, by substituting (B.6) for (B.5), we can obtain the probability that the user is served by a LoS BS as in

(5.15).

By conditioning that the serving base station is LoS, the PDF of distance from the user to its serving BS

$$f_{R_s}^{SS}(x|L) = \frac{\mathcal{B}_L f_L(x)}{\mathcal{A}_L} \exp\left(-2\lambda_b \pi \int_0^{\vartheta_L(x)} p_N(t) t dt\right) \tag{B.7}$$

Finally, after some simple mathematical manipulations, (B.7) can be written as in **Lemma 5.2**.

B.3 Proof of Lemma 5.5

The distribution of R_x^a for **Case 1** can be obtained by following the similar steps as in the derivation of the distribution of the distance between two nodes in a circle [103]. However, we include the exclusion region around the typical BS, where it guarantees that there are no active UEs are located inside this region. Thus, the PDF of distance in **Lemma 5.5** is conditioned by R_s resulting in the random variable R_x^a has the domain $[R_s, R_s + D_c]$.

Next, we derive the PDF of R_x^a for **Case 2**. Let R_y be the distance from the typical BS to the cluster center. Since we have assumed that the typical UE is located at the origin, we have $R_y = R_s$ for the intra-cluster interference. As illustrated in Fig. 5.3, when the typical BS is located outside the typical cluster, the interferer may exist on numerous possible locations on the minor arc of a circle with radius r. It is expected that, as the distance of the interferer increases from r to $r + dr$, the minor arc will also gradually move outwards by distance dr. Denote by $\mathbb{P}(E|dr)$ the probability that the intra-cluster interfering UE falls within the shaded region swept by the minor arc during the movement, as illustrated in Fig. 5.3. Then, conditioned on Rs, we can express the PDF of

R_x^a as

$$f_{R_x^a}(r|R_s) = \lim_{dr\to 0} \frac{\mathbb{P}(E|dr)}{dr} \overset{(a)}{=} \frac{2r\arccos\left(\frac{R_s^2+r^2-D_c^2}{2R_s r}\right)dr}{dr} \overset{(b)}{=} \frac{2r\arccos\left(\frac{R_s^2+r^2-D_c^2}{2R_s r}\right)dr}{\pi D_c^2 dr}, \tag{B.8}$$

where (a) follows from the area of the shaded region and (b) is caused by uniform distribution of the intra-cluster interfering UEs within the circles with radius D_c. Thus, the proof is complete.

B.4 Proof of Lemma 5.6

We note that the distance of interferer depends on R_y, which refer to the similar cases in **Lemma 5.5**, i.e., **Case 1** and **Case 2**. The inter-cluster interfering UE can be classified into the following cases.

Case 1: When $0 < R_y < D_c$. In this case, the typical BS is located inside the cluster. Here we include the exclusion region as depicted in Fig. 5.2. Consequently, the minimum distance from this UE to the typical BS is R_s. Given the distance $R_s < R_y < D_c$, the possible location of the inter-cluster interference UE that has the same distance to the typical BS can be further classified into three types:

(i) when $R_s \leq r \leq D_c - R_y$ as shown in Fig. 5.2 (blue dashed), the interfering UE lies on the circumference of a circle centered at the typical BS point with radius r, which gives the first case of (5.25).

(ii) when $D_c - R_y \leq r \leq \sqrt{D_c^2 - R_y^2}$ as depicted in Fig. 5.2 (red dashed), the interfering UE lies on the major arc of a circle centered at the typical BS point with radius r, which gives the second case of (5.25).

(iii) when $\sqrt{D_c^2 - R_y^2} \leq r \leq D_c - R_y$ as shown in Fig. 5.2 (green dashed), the

interfering UE lies on the minor arc of a circle centered at the typical BS point with radius r, which gives the third case of (5.25).

Case 2: When $R_y > D_c$, the typical BS is located outside the cluster. The possible location of the inter-cluster interfering UE that has the same distance from the typical user is on the minor arc of a circle with radius r, i.e., denoted as dash-line in Fig. 5.3, which gives the first case of (5.26).

Finally, to obtain the PDF of R_x^e, we can follow the similar derivation as those in **Lemma 5.5**, except that we replace the area of the shaded region following the cases mentioned above.

B.5 Proof of Theorem 5.1

Recall that the intra-cluster interference is given in (5.28). I_{LL}^a can be computed as the sum of interference from each LoS UEs with LoS links to their serving BSs, which is given by

$$I_{LL}^a = \sum_{\mathbf{x} \in \kappa^{\mathbf{0}} \cap \psi^L} h_{\mathbf{x},\mathbf{z}} G_{\mathbf{x},\mathbf{z}} \delta r^{-\alpha_L} t^{\alpha_L \epsilon}, \tag{B.9}$$

where ψ_L is the points of $\kappa^{\mathbf{0}}$ with LoS to its serving BS.

Similarly, I_{LN}^a can be computed as the sum of interference from each LoS UEs with non-LoS links to their serving BSs, which is given by

$$I_{LN}^a = \sum_{\mathbf{x} \in \kappa^{\mathbf{0}} \cap \psi^N} h_{\mathbf{x},\mathbf{z}} G_{\mathbf{x},\mathbf{z}} \delta r^{-\alpha_L} t^{\alpha_N \epsilon}, \tag{B.10}$$

where ψ_N is the points of $\kappa^{\mathbf{0}}$ with non-LoS to its serving BS.

I_{NL}^a can be computed as the sum of interference from each non-LoS UEs with

LoS links to their serving BSs, which is given by

$$I_{NL}^{a} = \sum_{\mathbf{x}\in\kappa^{\mathbf{0}}\cap\psi^{L}} h_{\mathbf{x},\mathbf{z}} G_{\mathbf{x},\mathbf{z}} \delta r^{-\alpha_N} t^{\alpha_L \epsilon}. \tag{B.11}$$

I_{NN}^{a} can be computed as the sum of interference from each non-LoS UEs with non-LoS links to their serving BSs, which is given by

$$I_{NN}^{a} = \sum_{\mathbf{x}\in\kappa^{\mathbf{0}}\cap\psi^{N}} h_{\mathbf{x},\mathbf{z}} G_{\mathbf{x},\mathbf{z}} \delta r^{-\alpha_N} t^{\alpha_N \epsilon}. \tag{B.12}$$

First, we derive the Laplace transform of I_{LL}^{a}. Conditioned on R_s and based on (B.9), we have

$$\begin{aligned}
\mathcal{L}_{I_{LL}^{a}}(s|\, R_s) &= \mathbb{E}\left[\exp\left(-s \sum_{\mathbf{x}\in\kappa^{\mathbf{0}}\cap\psi^{L}} h_{\mathbf{x},\mathbf{z}} G_{\mathbf{x},\mathbf{z}} \delta r^{-\alpha_L} t^{\alpha_L \epsilon}\right)\right] \\
&\overset{(a)}{=} \mathbb{E}\left[\prod_{\mathbf{x}\in\kappa^{\mathbf{0}}\cap\psi^{L}} \frac{1}{1+\frac{s G_{\mathbf{x},\mathbf{z}} \delta t^{\alpha_L \epsilon}}{r^{\alpha_L}}}\right] \\
&\overset{(b)}{=} \exp\left(-n \sum_{k=1}^{4} b_k \int_{R_s}^{D_c+R_s} \left(1 - \frac{1}{1+\frac{s a_k \delta t^{\alpha_L \epsilon}}{r^{\alpha_L}}}\right)\right. \\
&\qquad \left. \times f_{R_x^a}(r|R_s) dr\right) \\
&\overset{(c)}{=} \exp\left(-n \sum_{k=1}^{4} b_k \int_{0}^{\infty} \int_{R_s}^{D_c+R_s} \left(1 - \frac{1}{1+\frac{s a_k \delta t^{\alpha_L \epsilon}}{r^{\alpha_L}}}\right)\right. \\
&\qquad \left. \times f_{R_x^a}(r|R_s) f_{R_t}^{\xi}(t|L) dr dt\right),
\end{aligned} \tag{B.13}$$

where (a) is the moment generating function of the exponential random variable, (b) follows from (5.11) and the assumption that $G_{\mathbf{x},\mathbf{z}}$ is a discrete random variable and from the generating functional of PPP, (c) by unconditioning on t where the PDF of R_t is given in **Lemma 5.4**. Then, we have the Laplace transform of I_{LL}^{a} as in (5.31).

The Laplace transforms for I_{LN}^{a}, I_{NL}^{a}, and I_{NN}^{a} are obtained following the similar steps as in (B.13) and are given as in (5.32), (5.33) and (5.34), respectively. Finally, the Laplace transform of the overall I_a is given by the product of

individual Laplace transforms as in **Theorem 5.1**.

B.6 Proof of Theorem 5.2

Based on (5.9), the Laplace transform of I^e_{LL} is given by

$$\begin{aligned}
\mathcal{L}_{I^e_{LL}}(s|\, R_s) &= \mathbb{E}\left[\exp\left(-s\sum_{\mathbf{y}\in\Phi_p}\sum_{\mathbf{x}\in\kappa^{\mathbf{y}}} h_{\mathbf{x},\mathbf{z}}G_{\mathbf{x},\mathbf{z}}\delta r^{-\alpha_L}t^{\alpha_L\epsilon}\right)\right] \\
&\overset{(a)}{=} \mathbb{E}_{\Phi_p}\left[\prod_{\mathbf{y}\in\Phi^p}\mathbb{E}_{\kappa^{\mathbf{y}}}\left[\prod_{\mathbf{x}\in\kappa^{\mathbf{y}}}\frac{1}{1+\frac{sG_{\mathbf{x},\mathbf{z}}\delta t^{\alpha_L\epsilon}}{r^{\alpha_L}}}\right]\right] \\
&\overset{(b)}{=} \exp\left(-\lambda_p\sum_{c\in\{L,N\}}\int_{\mathbb{R}^2}(1-\beta_{LL}(y,s))p_c(y)dy\right) \\
&= \exp\left(-2\pi\lambda_p\sum_{c\in\{L,N\}}\int_v^\infty(1-\beta_{LL}(y,s))yp_c(y)dy\right) \qquad \text{(B.14)}
\end{aligned}$$

where (a) is the moment generating function of the exponential random variable, (b) is from (5.10) and $\beta_{LL}(y,s)$ is the generating functional of the cluster centered at $\mathbf{y}$, which is given by

$$\begin{aligned}
\beta_{LL}(y,s) = \exp\Bigg(-n\sum_{k=1}^{4}b_k\int_0^\infty\int_{\mathcal{R}}\left(1-\frac{1}{1+\frac{sa_k\delta t^{\alpha_L\epsilon}}{r^{\alpha_L}}}\right) \qquad \text{(B.15)} \\
\times f_{R^e_x}(r|R_s)f^{\xi}_{R_t}(t|L)drdt.
\end{aligned}$$

The Laplace transforms for I^e_{LN}, I^e_{NL}, and I^e_{NN} can be obtained following the similar steps as in (B.14). Then, the Laplace transform of the overall I_e is obtained from the product of individual Laplace transforms as in **Theorem 5.2**.

B.7 Proof of Theorem 5.3

Given that the link from the typical UE to the typical BS located at $\mathbf{z} \triangleq (R_s, 0)$ is LoS and based on (5.7), the conditional coverage probability can be computed

as

$$\begin{aligned}
&\mathbb{P}(\gamma|L, R_s) = \mathbb{P}\left(\mathrm{SINR}_{\mathbf{z}} > \gamma\right) \\
&= \mathbb{P}\left(\frac{h_{\mathbf{z}} M_b M_u \delta R_s^{\alpha_L(\epsilon-1)}}{\sigma^2 + I} > \gamma\right) \\
&= \exp\left(-\frac{\gamma\sigma^2 R_s^{\alpha_L(1-\epsilon)}}{\delta M_b M_u}\right) \mathbb{E}\left[\exp\left(-\frac{t R_s^{\alpha_L(1-\epsilon)} I}{\delta M_b M_u}\right)\right] \\
&= \exp\left(-\frac{\gamma\sigma^2 R_s^{\alpha_L(1-\epsilon)}}{\delta M_b M_u}\right) \mathcal{L}_I\left(\frac{t R_s^{\alpha_L(1-\epsilon)} I}{\delta M_b M_u}\right) \\
&= \exp\left(-s_L\sigma^2\right) \mathcal{L}_I\left(s|\, R_s\right)
\end{aligned} \tag{B.16}$$

where $s = \frac{\gamma R_s^{\alpha_L(1-\epsilon)}}{\delta M_b M_u}$ and I is the interfering UEs. Recall that we have assumed that UEs within the cluster have the same link status to the typical BS and only LoS clusters are considered in the CS strategy. Thus, we have $I = I^a + I^e = I^a_{LL} + I^e_{LL}$, where the Laplace transforms are given by (B.13) and (B.14). Finally, by substituting (B.13) and (B.14) into (B.16), and by unconditioning the derived expression with the PDF of R_s, which is given in **Lemma 5.1**, we conclude with the desired expression in **Theorem 5.3**.

Bibliography

[1] J. Wells, "Faster than fiber: The future of multi-g/s wireless," *IEEE Micro. Mag.*, vol. 10, no. 3, pp. 104–112, May 2009.

[2] T. S. Rappaport, R. W. H. Jr., R. C. Daniels, and J. N. Murdock, *Millimeter Wave Wireless Communications*, 1st ed. Prentice Hall, 2014.

[3] T. Rappaport, S. Sun, R. Mayzus, H. Zhao, Y. Azar, K. Wang, G. Wong, J. Schulz, M. Samimi, and F. Gutierrez, "Millimeter wave mobile communications for 5G cellular: It will work!" *IEEE Access*, vol. 1, pp. 335–349, May 2013.

[4] Z. Pi and F. Khan, "An introduction to millimeter-wave mobile broadband systems," *IEEE Comm. Mag.*, vol. 49, no. 6, pp. 101–107, Jun. 2011.

[5] Cisco visual networking index: Global mobile data traffic forecast update, 2016-2021 white paper. [Online]. Available: http://goo.gl/SwuEIc

[6] C. E. Shannon, "A mathematical theory of communication," *The Bell System Technical Journal*, vol. 27, pp. 379–423, Jul. 1948.

[7] J. Andrews, S. Buzzi, W. Choi, S. Hanly, A. Lozano, A. Soong, and J. Zhang, "What will 5G be?" *IEEE J. Sel. Areas Commun.*, vol. 32, no. 6, pp. 1065–1082, Jun. 2014.

[8] Y. Niu, Y. Li, D. Jin, L. Su, and A. V. Vasilakos, "A survey of millimeter wave communications (mmWave) for 5G: opportunities and challenges,"

Wireless Networks, vol. 21, no. 8, pp. 2657–2676, 2015. [Online]. Available: http://dx.doi.org/10.1007/s11276-015-0942-z

[9] D. Roddy, *Satellite Communications*, 4th ed. USA: McGraw-Hill, 2006.

[10] S. Seidel and H. Arnold, "Propagation measurements at 28 GHz to investigate the performance of local multipoint distribution service (LMDS)," in *Wireless Commun. Conf.*, Nov. 1995, pp. 754–757.

[11] T. Baykas, C. S. Sum, Z. Lan, J. Wang, M. A. Rahman, H. Harada, and S. Kato, "IEEE 802.15.3c: the first IEEE wireless standard for data rates over 1 Gb/s," *IEEE Commun. Mag.*, vol. 49, no. 7, pp. 114–121, Jul. 2011.

[12] IEEE, "IEEE Standard-Part 11: Wireless LAN MAC and PHY Specifications Amendment 3: Enhancements for Very High Throughput in the 60 GHz Band," Dec 2012.

[13] WirelessHD. (2009, Aug.) WirelessHD specification overview. [Online]. Available: http://www.wirelesshd.org/wp-content/uploads/2009/12/WirelessHD-Specification-Overview-v1-0-4-Aug09.pdf

[14] A. Maltsev, A. Pudeyev, A. Lomayev, and I. Bolotin, "Channel modeling in the next generation mmWave Wi-Fi: IEEE 802.11ay standard," in *Proc. 22nd Eur. Wireless Conf. Eur. Wireless*, May 2016, pp. 1–8.

[15] FCC, "Allocations and service rules for the 71-76 GHz, 81-86 GHz, and 92-95GHz bands," *FCC Memorandum Opinion and Order 05-45, Federal Communications Commission*, 2005.

[16] ECC, "Radio frequency channel arrangements for fixed service systems operating in the bands 71-76GHz and 81-86 GHz," *ECC Recommendation (05)07*, 2005.

[17] T. S. Rappaport, F. Gutierrez, E. Ben-Dor, J. N. Murdock, Y. Qiao, and J. I. Tamir, "Broadband millimeter-wave propagation measurements and models using adaptive-beam antennas for outdoor urban cellular communications," *IEEE Trans. Antennas and Propag.*, vol. 61, no. 4, pp. 1850–1859, Apr. 2013.

[18] T. S. Rappaport, G. R. MacCartney, M. K. Samimi, and S. Sun, "Wideband millimeter-wave propagation measurements and channel models for future wireless communication system design," *IEEE Trans. Comm.*, vol. 63, no. 9, pp. 3029–3056, Sep. 2015.

[19] C. Gustafson, K. Haneda, S. Wyne, and F. Tufvesson, "On mm-wave multipath clustering and channel modeling," *IEEE Trans. Antennas Propag.*, vol. 62, no. 3, pp. 1445–1455, Mar. 2014.

[20] T. Bai, R. Vaze, and R. Heath, "Analysis of blockage effects on urban cellular networks," *IEEE Trans. Wireless Commun.*, vol. 13, no. 9, pp. 5070–5083, Sept. 2014.

[21] S. Singh, M. Kulkarni, A. Ghosh, and J. Andrews, "Tractable model for rate in self-backhauled millimeter wave cellular networks," *IEEE J. Sel. Areas Commun.*, vol. 33, no. 10, pp. 2196–2211, Oct. 2015.

[22] H. Shokri-Ghadikolaei and C. Fischione, "The transitional behavior of interference in millimeter wave networks and its impact on medium access control," *IEEE Trans. Comm.*, vol. 64, no. 2, pp. 723–740, Feb. 2016.

[23] K. Venugopal, M. C. Valenti, and R. W. Heath, "Device-to-device millimeter wave communications: Interference, coverage, rate, and finite topologies," *IEEE Trans. Wireless Commun.*, vol. 15, no. 9, pp. 6175–6188, Sep. 2016.

[24] S. Rajagopal, S. Abu-Surra, and M. Malmirchegini, "Channel feasibility for outdoor non-line-of-sight mmwave mobile communication," in *Proc. IEEE VTC Fall*, Sep. 2012, pp. 1–6.

[25] H. Zhang, S. Venkateswaran, and U. Madhow, "Channel modeling and mimo capacity for outdoor millimeter wave links," in *Proc. IEEE WCNC*, Apr. 2010, pp. 1–6.

[26] Q. Li, G. Wu, and T. Rappaport, "Channel model for millimeter-wave communications based on geometry statistics," in *Proc., IEEE Globecom Workshops*, Dec. 2014, pp. 427–432.

[27] M. Samimi and T. Rappaport, "Ultra-wideband statistical channel model for non line of sight millimeter-wave urban channels," in *Proc. IEEE Globecom*, Dec. 2014, pp. 3483–3489.

[28] S. Geng, J. Kivinen, X. Zhao, and P. Vainikainen, "Millimeter-wave propagation channel characterization for short-range wireless communications," *IEEE Trans. Veh. Technol.*, vol. 58, no. 1, pp. 3–13, Jan. 2009.

[29] W. Roh, J. Seol, J. Park, B. Lee, J. Lee, Y. Kim, J. Cho, K. Cheun, and F. Aryanfar, "Millimeter-wave beamforming as an enabling technology for 5g cellular communications: theoretical feasibility and prototype results," *IEEE Communications Magazine*, vol. 52, no. 2, pp. 106–113, Feb. 2014.

[30] S. Rangan, T. Rappaport, and E. Erkip, "Millimeter-Wave Cellular Wireless Networks: Potentials and Challenges," *Proceedings of the IEEE*, vol. 102, no. 3, pp. 366–385, Mar. 2014.

[31] Y. Li, J. G. Andrews, F. Baccelli, T. D. Novlan, and C. J. Zhang, "Design and analysis of initial access in millimeter wave cellular networks," *IEEE Trans. Wireless Commun.*, vol. 16, no. 10, pp. 6409–6425, Oct. 2017.

[32] R. W. Heath, N. GonzÃ¡lez-Prelcic, S. Rangan, W. Roh, and A. M. Sayeed, "An overview of signal processing techniques for millimeter wave mimo systems," *IEEE Journal of Selected Topics in Signal Processing*, vol. 10, no. 3, pp. 436–453, Apr. 2016.

[33] S. Han, C. I, Z. Xu, and C. Rowell, "Large-scale antenna systems with hybrid analog and digital beamforming for millimeter wave 5g," *IEEE Communications Magazine*, vol. 53, no. 1, pp. 186–194, Jan. 2015.

[34] J. Singh, S. Ponnuru, and U. Madhow, "Multi-gigabit communication: the adc bottleneck lt;sup gt;1 lt;/sup gt;," in *2009 IEEE International Conference on Ultra-Wideband*, Sep. 2009, pp. 22–27.

[35] J. Mo and R. W. Heath, "Capacity analysis of one-bit quantized mimo systems with transmitter channel state information," *IEEE Trans. Signal Processing*, vol. 63, no. 20, pp. 5498–5512, Oct. 2015.

[36] J. Jarvelainen and K. Haneda, "Sixty gigahertz indoor radio wave propagation prediction method based on full scattering model," *Radio Science*, vol. 49, no. 4, pp. 293–305, Apr. 2014.

[37] R. Cowan, "Objects arranged randomly in space: an accessible theory," *Advances in Applied Probability*, vol. 21, no. 3, pp. 543–569, 1989.

[38] M. Akdeniz, Y. Liu, M. Samimi, S. Sun, S. Rangan, T. Rappaport, and E. Erkip, "Millimeter wave channel modeling and cellular capacity evaluation," *IEEE J. Sel. Areas Commun.*, vol. 32, no. 6, pp. 1164–1179, Jun. 2014.

[39] C. Liu, M. Li, S. V. Hanly, P. Whiting, and I. B. Collings, "Millimeter-wave small cells: Base station discovery, beam alignment, and system design challenges," *IEEE Wireless Communications*, vol. 25, no. 4, pp. 40–46, Aug. 2018.

[40] G. J. Foschini, K. Karakayali, and R. A. Valenzuela, "Coordinating multiple antenna cellular networks to achieve enormous spectral efficiency," *Proc. IEEE Communications*, vol. 153, no. 4, pp. 548–555, Aug. 2006.

[41] F. Baccelli and A. Giovanidis, "A stochastic geometry framework for analyzing pairwise-cooperative cellular networks," *IEEE Trans. Wireless Commun.*, vol. 14, no. 2, pp. 794–808, Feb. 2015.

[42] K. Huang and J. G. Andrews, "An analytical framework for multicell cooperation via stochastic geometry and large deviations," *IEEE Trans. Info. Th.*, vol. 59, no. 4, pp. 2501–2516, Apr. 2013.

[43] T. A. Khan, X. Zhang, and R. W. Heath, "A stochastic geometry approach to analyzing cellular networks with semi-static clustering," in *Proc. IEEE Global Communications Conference (GLOBECOM)*, Dec. 2015, pp. 1–6.

[44] W. Choi and J. G. Andrews, "The capacity gain from intercell scheduling in multi-antenna systems," *IEEE Trans. Wireless Commun.*, vol. 7, no. 2, pp. 714–725, Feb. 2008.

[45] J. Zhang and J. G. Andrews, "Adaptive spatial intercell interference cancellation in multicell wireless networks," *IEEE Journal on Selected Areas in Communications*, vol. 28, no. 9, pp. 1455–1468, Dec. 2010.

[46] C. Li, J. Zhang, M. Haenggi, and K. B. Letaief, "User-centric intercell interference nulling for downlink small cell networks," *IEEE Trans. Comm.*, vol. 63, no. 4, pp. 1419–1431, Apr 2015.

[47] O. E. Ayach, S. Rajagopal, S. Abu-Surra, Z. Pi, and R. W. Heath, "Spatially sparse precoding in millimeter wave mimo systems," *IEEE Trans. Wireless Commun.*, vol. 13, no. 3, pp. 1499–1513, Mar. 2014.

[48] M. N. Kulkarni, A. Alkhateeb, and J. G. Andrews, "A tractable model for per user rate in multiuser millimeter wave cellular networks," in *2015 49th Asilomar Conference on Signals, Systems and Computers*, Nov. 2015, pp. 328–332.

[49] M. Kokshoorn, H. Chen, P. Wang, Y. Li, and B. Vucetic, "Millimeter wave mimo channel estimation using overlapped beam patterns and rate adaptation," *IEEE Trans. Signal Processing*, vol. 65, no. 3, pp. 601–616, Feb. 2017.

[50] T. Bai and R. W. Heath, "Coverage and rate analysis for millimeter-wave cellular networks," *IEEE Trans. Wireless Comm.*, vol. 14, no. 2, pp. 1100–1114, Feb. 2015.

[51] A. Goldsmith, *Wireless Communications*. Cambridge University Press, 2005.

[52] A. V. Alejos, M. G. Sanchez, and I. Cuinas, "Measurement and analysis of propagation mechanisms at 40 ghz: Viability of site shielding forced by obstacles," *IEEE Trans. Veh. Technol.*, vol. 57, no. 6, pp. 3369–3380, Nov., 2008.

[53] C. R. Anderson and T. S. Rappaport, "In-building wideband partition loss measurements at 2.5 and 60 ghz," *IEEE Trans. Wireless Commun.*, vol. 3, no. 3, pp. 922–928, May 2004.

[54] B. Langen, G. Lober, and W. Herzig, "Reflection and transmission behaviour of building materials at 60 ghz," in *5th IEEE International Symposium on Personal, Indoor and Mobile Radio Communications, Wireless Networks - Catching the Mobile Future.*, Sep. 1994, pp. 505–509 vol.2.

[55] K. C. Allen, N. DeMinco, J. Hoffman, Y. Lo, and P. Papazian, "Building penetration loss measurements at 900 MHz, 11.4 GHz, and 28.8 GHz," *NTIA rep.*, pp. 94–306, May 1994.

[56] S. Joshi and S. Sancheti, "Foliage loss measurements of tropical trees at 35 ghz," in *2008 International Conference on Recent Advances in Microwave Theory and Applications*, Nov. 2008, pp. 531–532.

[57] A. Y. Nashashibi, K. Sarabandi, S. Oveisgharan, M. C. Dobson, W. S. Walker, and E. Burke, "Millimeter-wave measurements of foliage attenuation and ground reflectivity of tree stands at nadir incidence," *IEEE Trans. Antennas Propag.*, vol. 52, no. 5, pp. 1211–1222, May 2004.

[58] J. S. Lu, D. Steinbach, P. Cabrol, and P. Pietraski, "Modeling human blockers in millimeter wave radio links," *ZTE Communications*, vol. 10, no. 4, pp. 23–28, Dec. 2012.

[59] S. Hur, S. Baek, B. Kim, Y. Chang, A. F. Molisch, T. S. Rappaport, K. Haneda, and J. Park, "Proposal on millimeter-wave channel modeling for 5g cellular system," *IEEE Journal of Selected Topics in Signal Processing*, vol. 10, no. 3, pp. 454–469, Apr. 2016.

[60] H. C. Nguyen, G. R. MacCartney, T. Thomas, T. S. Rappaport, B. Vejlgaard, and P. Mogensen, "Evaluation of empirical ray-tracing model for an urban outdoor scenario at 73 ghz e-band," in *2014 IEEE 80th Vehicular Technology Conference (VTC2014-Fall)*, Sep. 2014, pp. 1–6.

[61] A. M. Hunter, J. G. Andrews, and S. Weber, "Transmission capacity of ad hoc networks with spatial diversity," *IEEE Trans. Wireless Comm.*, vol. 7, no. 12, pp. 5058–5071, Dec. 2008.

[62] W. Stoyan, D. Kendall and J. Mecke, *Stochastic Geometry and Its Applications*, 2nd ed. John Wiley and Sons, 1995.

[63] F. Baccelli and B. Blaszczyszyn, *Stochastic Geometry and Wireless Networks*. Boston, MA, USA: NOW, 2009, vol. I-Theory.

[64] J. G. Andrews, F. Baccelli, and R. K. Ganti, "A tractable approach to coverage and rate in cellular networks," *IEEE Trans. Comm.*, vol. 59, no. 11, pp. 3122–3134, Nov. 2011.

[65] M. Haenggi, *Stochastic Geometry for Wireless Networks*, Cambridge Press, Ed. Cambridge Press, 2013.

[66] R. K. Ganti and M. Haenggi, "Interference and outage in clustered wireless ad hoc networks," *IEEE Trans. Info. Theory*, vol. 55, no. 9, pp. 4067–4086, Sep. 2009.

[67] M. Afshang and H. S. Dhillon, "Poisson cluster process based analysis of hetnets with correlated user and base station locations," *IEEE Trans. Wireless Commun.*, vol. PP, no. 99, pp. 1–1, 2018.

[68] S. Priebe, M. Kannicht, M. Jacob, and T. Kurner, "Ultra broadband indoor channel measurements and calibrated ray tracing propagation modeling at THz frequencies," *Journal of Communications and Networks*, vol. 15, no. 6, pp. 547–558, Dec. 2013.

[69] METIS ICT-317669-METIS/D1.2, "Initial channel models based on measurements." [Online]. Available: https://www.metis2020.com/

[70] H. Xu, V. Kukshya, and T. Rappaport, "Spatial and temporal characteristics of 60 GHz indoor channels," *IEEE J. Sel. Areas Commun.*, vol. 20, no. 3, pp. 620–630, Apr. 2002.

[71] S. Larew, T. Thomas, M. Cudak, and A. Ghosh, "Air interface design and ray tracing study for 5G millimeter wave communications," in *Proc., IEEE Globecom Workshops*, Dec. 2013, pp. 117–122.

[72] G. Franceschetti, S. Marano, and F. Palmieri, "Propagation without wave equation toward an urban area model," *IEEE Trans. Antennas Propag.*, vol. 47, no. 9, pp. 1393–1404, Sep. 1999.

[73] S. Marano and M. Franceschetti, "Ray propagation in a random lattice: a maximum entropy, anomalous diffusion Process," *IEEE Trans. Antennas Propag.*, vol. 53, no. 6, pp. 1888–1896, Jun. 2005.

[74] J. D. Parson, *The Mobile Radio Propagation Channel*, 2nd ed. New York: John Wiley and Sons, May 2000.

[75] M. Kyro, V. Semkin, and V. Kolmonen, "Empirical characterization of scattering pattern of built surfaces at mm-wave frequencies," in *Proc. EuCAP*, Apr. 2013, pp. 112–115.

[76] B. Langen, G. Lober, and W. Herzig, "Reflection and transmission behaviour of building materials at 60 GHz," in *Proc. IEEE PMIRC*, Sep. 1994, pp. 505–509.

[77] J. Hansen, "An analytical calculation of power delay profile and delay spread with experimental verification," *IEEE Comm. Lett.*, vol. 7, no. 6, pp. 257–259, Jun. 2003.

[78] A. Raisanen, J. Ala-Laurinaho, K. Haneda, J. Jarvelainen, A. Karttunen, M. Kyro, V. Semkin, A. Lamminen, and J. Saily, "Studies on E-band antennas and propagation," in *Proc. Antennas and Propagation Conference*, Nov. 2013, pp. 176–180.

[79] A. Meijerink and A. Molisch, "On the physical interpretation of the saleh valenzuela model and the definition of its power delay profiles," *IEEE Trans. Antennas Propag.*, vol. 62, no. 9, pp. 4780–4793, Sep. 2014.

[80] J. Liberti and T. Rappaport, *Smart Antennas for Wireless Communications: IS-95 and Third Generation CDMA Applications.* Prentice Hall, 1999.

[81] D. Maamari, N. Devroye, and D. Tuninetti, "Coverage in mmwave cellular networks with base station cooperation," *IEEE Trans. Wireless Comm.*, vol. 15, no. 4, pp. 2981–2944, Apr. 2016.

[82] S. Bassoy, M. Jaber, M. A. Imran, and P. Xiao, "Load aware self-organising user-centric dynamic comp clustering for 5g networks," *IEEE Access*, vol. 4, pp. 2895–2906, May 2016.

[83] T. V. Sreejith, K. Kuchi, and R. K. Ganti, "Performance of cloud radio networks with clustering," in *IEEE International Conference on Communication Workshop (ICCW)*, Jun. 2015, pp. 2738–2743.

[84] A. Thornburg, T. Bai, and R. W. Heath, "Performance analysis of outdoor mmwave ad hoc networks," *IEEE Trans. Sig. Proc.*, vol. 64, no. 15, pp. 4065–4079, Aug 2016.

[85] M. Ding, P. Wang, D. Lopez-Perez, G. Mao, and Z. Lin, "Performance impact of LoS and NLoS transmissions in dense cellular networks," *IEEE Trans. Wireless Commun.*, vol. 15, no. 3, pp. 2365–2380, Mar. 2016.

[86] T. Bai and R. Heath, "Coverage analysis for millimeter wave cellular networks with blockage effects," in *Proc. IEEE GlobalSIP*, Dec 2013, pp. 727–730.

[87] M. Rebato, M. Mezzavilla, S. Rangan, F. Boccardi, and M. Zorzi. (2016, April) Understanding noise and interference regimes in 5g millimeter-wave cellular networks. http://arxiv.org/abs/1604.05622.

[88] H. Elshaer, M. N. Kulkarni, F. Boccardi, J. G. Andrews, and M. Dohler, "Downlink and uplink cell association with traditional macrocells and millimeter wave small cells," *IEEE Trans. Wireless Commun.*, vol. 15, no. 9, pp. 6244–6258, Sep. 2016.

[89] L. Zhang, W. Nie, G. Feng, F. C. Zheng, and S. Qin, "Uplink performance improvement by decoupling uplink/downlink access in hetnets," *IEEE Trans. Veh. Technol.*, vol. 66, no. 8, pp. 6862–6876, Aug. 2017.

[90] Y. Wang and Q. Zhu, "Performance analysis of clustered device-to-device networks using matern cluster process," *Wireless Netw*, pp. 1–10, 2018.

[91] S. M. Azimi-Abarghouyi, B. Makki, M. Haenggi, M. Nasiri-Kenari, and T. Svensson, "Stochastic geometry modeling and analysis of single-and multi-cluster wireless networks," *IEEE Trans. Comm.*, pp. 1–1, 2018.

[92] M. Afshang, H. S. Dhillon, and P. H. J. Chong, "Modeling and performance analysis of clustered device-to-device networks," *IEEE Trans. Wireless Commun.*, vol. 15, no. 7, pp. 4957–4972, Jul. 2016.

[93] A. Thornburg and R. W. Heath, "Ergodic rate of millimeter wave ad hoc networks," *IEEE Trans. Wireless Comm.*, vol. 17, no. 2, pp. 914–926, Feb. 2018.

[94] E. Turgut and M. C. Gursoy. (2017) Uplink performance analysis in d2d-enabled mmwave cellular networks with clustered users. [Online]. Available: https://arxiv.org/abs/1710.10169

[95] T. D. Novlan, H. S. Dhillon, and J. G. Andrews, "Analytical modeling of uplink cellular networks," *IEEE Trans. Wireless Commun.*, vol. 12, no. 6, pp. 2669–2679, June 2013.

[96] O. Onireti, A. Imran, and M. A. Imran, "Coverage, capacity and energy efficiency analysis in the uplink of mmwave cellular networks," *IEEE Trans. Veh. Technol.*, vol. PP, no. 99, pp. 1–16, 2017.

[97] H. Jo, Y. J. Sang, P. Xia, and J. G. Andrews, "Heterogeneous cellular networks with flexible cell association: A comprehensive downlink SINR anal-

ysis," *IEEE Trans. Wireless Commun.*, vol. 11, no. 10, pp. 3484–3495, Oct. 2012.

[98] S. Singh, X. Zhang, and J. G. Andrews, "Joint rate and sinr coverage analysis for decoupled uplink-downlink biased cell associations in hetnets," *IEEE Trans. Wireless Commun.*, vol. 14, no. 10, pp. 5360–5373, Oct 2015.

[99] J. Park, S. L. Kim, and J. Zander, "Tractable resource management with uplink decoupled millimeter-wave overlay in ultra-dense cellular networks," *IEEE Trans. Wireless Commun.*, vol. 15, no. 6, pp. 4362–4379, Jun. 2016.

[100] E. Turgut and M. C. Gursoy, "Coverage in heterogeneous downlink millimeter wave cellular networks," *IEEE Trans. Comm.*, vol. 65, no. 10, pp. 4463–4477, Oct 2017.

[101] B. W. Lennart Rade, *Mathematics Handbook for Science and Engineering*, 5th ed. Springer, 2010.

[102] S. C. Stefan Waner, *Applied Calculus*, 6th ed. Cengage Learning, 2013.

[103] D. Moltchanov, "Survey paper: Distance distributions in random networks," *Ad Hoc Netw.*, vol. 10, no. 6, p. 1146â"1166, Aug. 2012.